

# Nanostructured Aerosol Particles: Fabrication, Pulmonary Drug Delivery, and Controlled Release

Guest Editors: Xingmao Jiang, Yung-Sung Cheng, and Hugh D. C. Smyth



---



# **Nanostructured Aerosol Particles: Fabrication, Pulmonary Drug Delivery, and Controlled Release**

## **Nanostructured Aerosol Particles: Fabrication, Pulmonary Drug Delivery, and Controlled Release**

Guest Editors: Xingmao Jiang, Yung-Sung Cheng,  
and Hugh D. C. Smyth



---

Copyright © 2011 Hindawi Publishing Corporation. All rights reserved.

This is a special issue published in volume 2011 of "Journal of Nanomaterials." All articles are open access articles distributed under the Creative Commons Attribution License, which permits unrestricted use, distribution, and reproduction in any medium, provided the original work is properly cited.

# Journal of Nanomaterials

## Editorial Board

Katerina Aifantis, Greece	Do Kyung Kim, Republic of Korea	Titipun Thongtem, Thailand
Nageh K. Allam, USA	Kin Tak Lau, Australia	Somchai Thongtem, Thailand
Margarida Amaral, Portugal	Burtrand Lee, USA	Valeri P. Tolstoy, Russia
Xuedong Bai, China	Benxia Li, China	Tsung-Yen Tsai, Taiwan
Enrico Bergamaschi, Italy	Jun Li, Singapore	Takuya Tsuzuki, Australia
Theodorian Borca-Tasciuc, USA	Shijun Liao, China	Raquel Verdejo, Spain
C. Jeffrey Brinker, USA	Gong Ru Lin, Taiwan	Mat U. Wahit, Malaysia
Christian Brosseau, France	J.-Y. Liu, USA	Shiren Wang, USA
Xuebo Cao, China	Jun Liu, USA	Yong Wang, USA
Sang-Hee Cho, Republic of Korea	Tianxi Liu, China	Cheng Wang, China
Shafiu Chowdhury, USA	Songwei Lu, USA	Zhenbo Wang, China
Cui ChunXiang, China	Daniel Lu, China	Jinquan Wei, China
Miguel A. Correa-Duarte, Spain	Jue Lu, USA	Ching Ping Wong, USA
Shadi A. Dayeh, USA	Ed Ma, USA	Xingcai Wu, China
Ali Eftekhari, USA	Gaurav Mago, USA	Guodong Xia, Hong Kong
Claude Estournes, France	Sanjay R. Mathur, Germany	Zhi Li Xiao, USA
Alan Fuchs, USA	Nobuhiro Matsushita, Japan	Ping Xiao, UK
Lian Gao, China	A. McCormick, USA	Shuangxi Xing, China
Russell E. Gorga, USA	Vikas Mittal, UAE	Yangchuan Xing, USA
Hongchen Chen Gu, China	Weihai Ni, Germany	N. Xu, China
Mustafa O. Guler, Turkey	Sherine Obare, USA	Doron Yadlovker, Israel
John Zhanhu Guo, USA	Edward Andrew Payzant, USA	Ying-Kui Yang, China
Smrati Gupta, Germany	Kui-Qing Peng, China	Khaled Youssef, USA
Michael Harris, USA	Anukorn Phuruangrat, Thailand	Kui Yu, Canada
Zhongkui Hong, USA	Ugur Serincan, Turkey	Haibo Zeng, China
Michael Z. Hu, USA	Huaiyu Shao, Japan	Tianyou Zhai, Japan
David Hui, USA	Donglu Shi, USA	Renyun Zhang, Sweden
Y.-K. Jeong, Republic of Korea	Suprakas Sinha Ray, South Africa	Yanbao Zhao, China
Sheng-Rui Jian, Taiwan	Vladimir Sivakov, Germany	Lianxi Zheng, Singapore
Wanqin Jin, China	Marinella Striccoli, Italy	Chunyi Zhi, Japan
Rakesh K. Joshi, India	Bohua Sun, South Africa	
Zhenhui Kang, China	Saikat Talapatra, USA	
Fathallah Karimzadeh, Iran	Nairong Tao, China	

## Contents

**Nanostructured Aerosol Particles: Fabrication, Pulmonary Drug Delivery, and Controlled Release,**  
Xingmao Jiang, Yung-Sung Cheng, and Hugh D. C. Smyth  
Volume 2011, Article ID 198792, 2 pages

**Controlled Release from Core-Shell Nanoporous Silica Particles for Corrosion Inhibition of Aluminum Alloys,** Xingmao Jiang, Ying-Bing Jiang, Nanguo Liu, Huifang Xu, Shailendra Rathod, Pratik Shah, and C. Jeffrey Brinker  
Volume 2011, Article ID 760237, 10 pages

**Photoresponsive Release from Azobenzene-Modified Single Cubic Crystal NaCl/Silica Particles,**  
Xingmao Jiang, Nanguo Liu, Roger A. Assink, Yingbing Jiang, and C. Jeffrey Brinker  
Volume 2011, Article ID 439756, 6 pages

**A Novel Aerosol Method for the Production of Hydrogel Particles,** Diana Guzman-Villanueva, Hugh D. C. Smyth, Dea Herrera-Ruiz, and Ibrahim M. El-Sherbiny  
Volume 2011, Article ID 507508, 10 pages

**Smart Magnetically Responsive Hydrogel Nanoparticles Prepared by a Novel Aerosol-Assisted Method for Biomedical and Drug Delivery Applications,** Ibrahim M. El-Sherbiny and Hugh D. C. Smyth  
Volume 2011, Article ID 910539, 13 pages

**Pilot Study of Inhaled Aerosols Targeted via Magnetic Alignment of High Aspect Ratio Particles in Rabbits,** Gillian E. S. Redman, Andrew R. Martin, Paul Waszak, Richard B. Thompson, Po-Yin Cheung, Bernard Thébaud, and Warren H. Finlay  
Volume 2011, Article ID 130721, 7 pages

**Facilitating Effects of Nanoparticles/Materials on Sensitive Immune-Related Lung Disorders,**  
Ken-ichiro Inoue and Hirohisa Takano  
Volume 2011, Article ID 407402, 6 pages

**Evaluating the Controlled Release Properties of Inhaled Nanoparticles Using Isolated, Perfused, and Ventilated Lung Models,** Moritz Beck-Broichsitter, Thomas Schmehl, Werner Seeger, and Tobias Gessler  
Volume 2011, Article ID 163791, 16 pages

## Editorial

# Nanostructured Aerosol Particles: Fabrication, Pulmonary Drug Delivery, and Controlled Release

Xingmao Jiang,<sup>1,2</sup> Yung-Sung Cheng,<sup>2</sup> and Hugh D. C. Smyth<sup>3</sup>

<sup>1</sup>Department of Chemical and Nuclear Engineering and Center for Micro-Engineered Materials, The University of New Mexico, Albuquerque, NM 87106, USA

<sup>2</sup>Aerosol and Respiratory Dosimetry Program, Lovelace Respiratory Research Institute, Albuquerque, NM 87108, USA

<sup>3</sup>Division of Pharmaceutics, College of Pharmacy, The University of Texas at Austin, Austin, TX 78712, USA

Correspondence should be addressed to Xingmao Jiang, xjiang@lrri.org

Received 3 March 2011; Accepted 3 March 2011

Copyright © 2011 Xingmao Jiang et al. This is an open access article distributed under the Creative Commons Attribution License, which permits unrestricted use, distribution, and reproduction in any medium, provided the original work is properly cited.

Pulmonary drug delivery is the preferred route of administration in the treatment of respiratory diseases and some nonrespiratory diseases. Recent research has focused on developing structurally stable high-dosage drug delivery systems without premature release. To maximize the deposition in the desired lung regions, several factors must be considered in the formulation. The special issue includes seven papers deal with aerosol-assisted fabrication of nanostructured particles, aerosol deposition, nanoparticles pulmonary exposure, and controlled release.

The delivery by inhalation utilizes the extensive surface area of the alveoli, avoiding hepatic first-pass metabolism and enabling noninvasive administration of larger doses to the lungs, leading to greater therapeutic efficacy without increasing toxicity. Pulmonary drug delivery is the preferred route of administration of aerosolized drugs in the treatment of respiratory diseases including asthma and cystic fibrosis, infectious diseases, in particular tuberculosis, and some nonrespiratory diseases such as type I diabetes. Recent research has focused on developing structurally stable high-dosage drug delivery systems without any premature release. To maximize the deposition in desired lung regions, a formulation must be carefully engineered to ensure the carriers have appropriate aerodynamic diameter, size distribution, porosity, density, surface chemistry for optimal dispersibility, and lung targeting. To overcome the problems with the instability of the formulation and poor loading efficiencies, sol gel approaches and wet chemistry have been applied for fabrication of nanocomposite particles with corrugated surfaces, reduced surface energy, and adjustable hydrophobicity/hydrophilicity to improve particle dispersion.

The seven papers presented in this special issue investigate aerosol-assisted fabrication of nanostructured particles, aerosol deposition, nanoparticle pulmonary exposure, and controlled release.

In the first paper, cerium corrosion inhibitors are encapsulated into hexagonally ordered nanoporous silica particles via single-step aerosol-assisted self-assembly. The core/shell structured particles are effective for corrosion inhibition of aluminum alloy AA2024-T3. The release can be controlled by the pore size, pore surface chemistry, and the inhibitor solubility.

In the second paper, azobenzene ligands are uniformly anchored to the pore surfaces of nanoporous silica particles with single-crystal NaCl. The addition of amphiphilic solvents into the release medium delays NaCl release. The functionalized particles demonstrate a photocontrolled release by trans/cis isomerization of azobenzene moieties.

In the third paper, hydrogel particles are produced from sprayed polymeric nano/microdroplets by a nebulization process that is immediately followed by gelation in a cross-linking fluid. Particle synthesis parameters such as type of nebulizer, type of crosslinker, air pressure, and polymer concentration are investigated for their impact on the mean particle size, swelling behavior, and morphology of the developed particles.

In the fourth paper, smart magnetically responsive hydrogel nanoparticles are prepared by a novel spray gelation-based method for biomedical and drug delivery applications. Oligoguluronate and PEG-grafted chitosan

are synthesized and characterized. Magnetically responsive hydrogel nanoparticles based on alginate and alginate/G-blocks are synthesized via aerosolization followed by either ionotropic gelation or both ionotropic and polyelectrolyte complexation using  $\text{CaCl}_2$  or PEG-g-chitosan/ $\text{CaCl}_2$  as crosslinking agents.

In the fifth paper, the authors study the feasibility of magnetically targeted delivery of high aspect ratio particles loaded with iron-oxide nanoparticles to the site of the tumour. Iron sensitive magnetic resonance images of the lungs are acquired to determine the iron concentrations in the right and left lung of each animal. The right/left ratio increases in the middle and basal regions of the lung. It is anticipated that with further optimization, this technique could be an effective method for increasing the dose of drug delivered to a specific site within the lung.

In the sixth paper, nanoparticles instilled through both an intratracheal tube and an inhalation system can exacerbate the lung inflammation by bacterial endotoxin. Repetitive pulmonary exposure to nanoparticles has aggravating effects on allergic airway inflammation, including adjuvant effects on Th2-milieu. Nanoparticle exposure may synergistically facilitate pathological inflammatory conditions in the lung via both innate and adaptive immunological abnormalities.

In the final paper, controlled release of inhaled nanoparticles is evaluated using isolated, perfused, and ventilated lung models. Ex vivo models are thought to overcome the common obstacles of in vitro tests and offer more reliable drug release and distribution data that are closer to the in vivo situation.

*Xingmao Jiang  
Yung-Sung Cheng  
Hugh D. C. Smyth*

## Research Article

# Controlled Release from Core-Shell Nanoporous Silica Particles for Corrosion Inhibition of Aluminum Alloys

Xingmao Jiang,<sup>1,2</sup> Ying-Bing Jiang,<sup>3</sup> Nanguo Liu,<sup>4</sup> Huifang Xu,<sup>5</sup> Shailendra Rathod,<sup>1</sup> Pratik Shah,<sup>1</sup> and C. Jeffrey Brinker<sup>1,6</sup>

<sup>1</sup> Department of Chemical and Nuclear Engineering and Center for Micro-Engineered Materials, University of New Mexico, Albuquerque, NM 87106, USA

<sup>2</sup> Aerosol and Respiratory Dosimetry Program, Lovelace Respiratory Research Institute, 2425 Ridgecrest Dr. SE, Albuquerque, NM 87108, USA

<sup>3</sup> Transmission Electron Microscopy Labs, The University of New Mexico, Albuquerque, NM 87131, USA

<sup>4</sup> SCB Innovation Accelerator, Dow Corning Corporation, 2200 W. Salzburg Road, P.O. Box 0994, Midland, MI 48686, USA

<sup>5</sup> Department of Geoscience, University of Wisconsin-Madison, Madison, WI 53706, USA

<sup>6</sup> Advanced Material Laboratory, Sandia National Laboratories, Albuquerque, NM 87185, USA

Correspondence should be addressed to C. Jeffrey Brinker, cjbrink@sandia.gov

Received 3 November 2010; Accepted 2 December 2010

Academic Editor: Hugh D. Smyth

Copyright © 2011 Xingmao Jiang et al. This is an open access article distributed under the Creative Commons Attribution License, which permits unrestricted use, distribution, and reproduction in any medium, provided the original work is properly cited.

Cerium (Ce) corrosion inhibitors were encapsulated into hexagonally ordered nanoporous silica particles via single-step aerosol-assisted self-assembly. The core/shell structured particles are effective for corrosion inhibition of aluminum alloy AA2024-T3. Numerical simulation proved that the core-shell nanostructure delays the release process. The effective diffusion coefficient elucidated from release data for monodisperse particles in water was  $1.0 \times 10^{-14}$  m<sup>2</sup>s for Ce<sup>3+</sup> compared to  $2.5 \times 10^{-13}$  m<sup>2</sup>s for NaCl. The pore size, pore surface chemistry, and the inhibitor solubility are crucial factors for the application. Microporous hydrophobic particles encapsulating a less soluble corrosion inhibitor are desirable for long-term corrosion inhibition.

## 1. Introduction

Controlled release is of particular interest for a broad spectrum of studies dealing with corrosion inhibition, fertilizers, and medical applications such as gene delivery, tissue engineering, and diagnostic agents. Long-term cost-effective corrosion inhibition of steels and alloys requires a controlled release of corrosion inhibitors especially for protecting the aluminum alloy AA2024-T3 used in aeronautic applications [1]. AA 2024 is composed of (in weight percentage) 93.5% Aluminum (Al), 4.4% Copper (Cu), 0.6% Manganese (Mn), and 1.5% Magnesium (Mg). Currently, carcinogenic chromate compounds have been widely used as corrosion inhibitors [2, 3], but these are expensive to process and maintain. The most potent and less toxic candidate inhibitors for aluminum alloys, according to the study by Scully's group and Tailor's group, are lanthanide, metavanadate, molybdenum, and cobalt ions [1, 4]. The inhibitors not only

suppress cathodic reactions in the alloys that are essential for corrosion inhibition and copper replating, but they provide self-healing for the alloys as well. Much effort has been made to investigate corrosion inhibition, ranging from barrier to conversion coatings or pigmentation of the inhibitors [5–8]. Layered clays have been tried for encapsulating the inhibitors by ion exchange [9]. A multifunctional organic coating containing silica can be formed by the in situ sol-gel process. However, this method lacks appropriate storage and slow release of corrosion inhibitors [10–13]. Nanoporous silica is a mechanically and thermally stable, cheap, and an environmentally benign ceramic, and it has found various applications in adsorption, separation, and catalysis [14, 15]. The well-controlled pore size, narrow pore size distribution, and controllable functionality and pore surface chemistries of self-assembled nanoporous silica materials suggest their use as the encapsulating material for controlled release of corrosion inhibitors. The promising nanocapsules can be

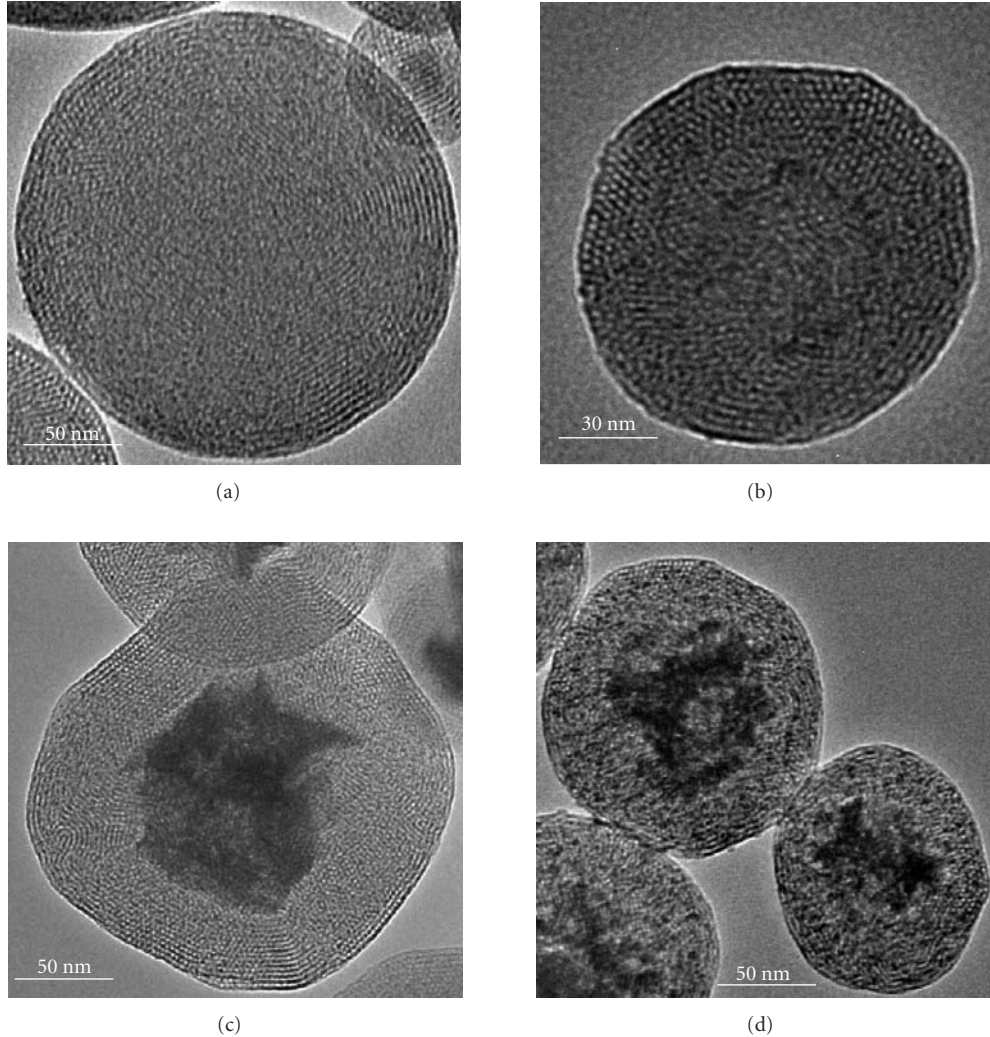


FIGURE 1: TEM images of nanostructured particles (a–d) with different loadings of Ce. The molar ratios of the precursor sol compositions are TEOS : EtOH : H<sub>2</sub>O : HCl : CTAB : CeCl<sub>3</sub> = 1 : 7.7 : 24.8 : 0.00125 : 0.18 : x, where x = 0, 0.06, 0.12, and 0.18, respectively, for particle samples (a)–(d).

dispersed as pigments into a protective epoxy coating for a long-term cost-effective protection of the alloys.

In this paper, we report a novel single-step method for encapsulating cerium (Ce) corrosion inhibitors into nanoporous silica particles by aerosol-assisted evaporation-induced self-assembly (EISA). Nanostructured particles with a core of Ce compounds and a shell of ordered nanoporous silica were prepared. These core-shell nanostructured particles are effective for inhibiting corrosion of aluminum alloy AA2024-T3. We investigated the controlled release of inhibitors and found that long-term corrosion inhibition can be realized using hydrophobic microporous nanocapsules.

## 2. Results and Discussion

The core-shell nanostructured particles were synthesized via aerosol-assisted EISA using cetyltrimethylammonium bromide (CTAB) as a structure-directing agent. Figure 1 shows

representative transmission electron microscopy (TEM) images of calcined silica particles. At low Ce loading the particles keep a hexagonally ordered mesoporous silica structure featuring parallel aligned stripes and hexagonally arranged pores (Figure 1(a)), reflecting differing orientations of a 2D hexagonal silica mesophase confined within a spherical shell. By increasing the loading of cerium chloride (CeCl<sub>3</sub>), the mesostructure turns into a core-shell structure (Figures 1(b) and 1(c)). At high loading (Figure 1(d)), the particles became worm-like or even less ordered, especially near the particle center.

Core-shell structured sample c has been characterized by X-ray diffraction (XRD) and nitrogen isothermal sorption. The nitrogen sorption isotherm of the nanostructured core-shell Ce/silica particles shown in Figure 2 was measured using liquid nitrogen at 77 K and yielded a type IV isotherm with a very narrow hysteresis loop, typical of hexagonal MCM-41-like mesoporous silicas. The pore size was determined to be 1.95 nm with a narrow distribution using

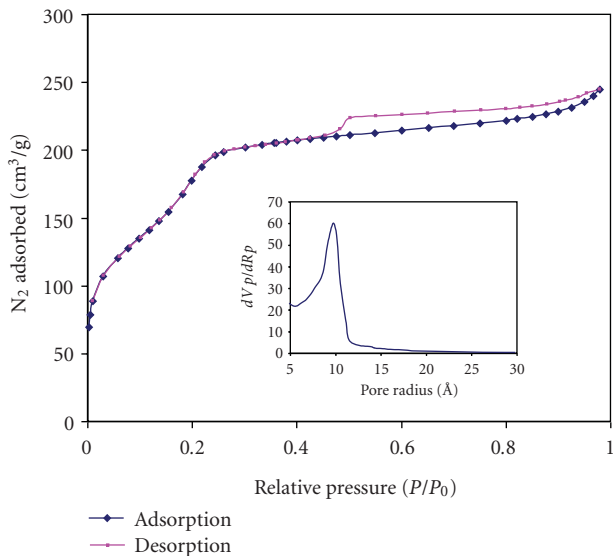


FIGURE 2: Nitrogen sorption for core-shell mesoporous particle b (Figure 1). Inset shows the BJH pore size distribution.

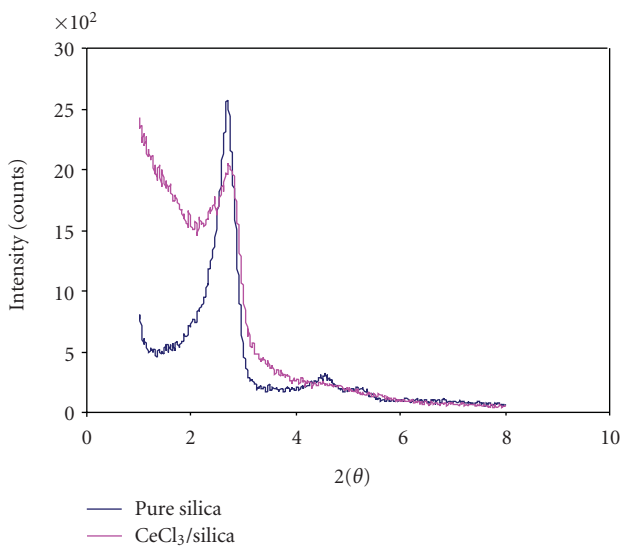


FIGURE 3: XRD patterns for sample a (pure silica) and sample c (Figure 1).

the Barrett-Joyner-Halenda (BJH) model. The Brunauer-Emmett-Teller (BET) surface area is  $615 \text{ m}^2/\text{g}$ . The low-angle peaks are associated with the 2D hexagonal silica mesophase. As can be seen from the XRD patterns shown in Figure 3, compared to pure mesoporous silica the mesostructural order for sample c (Figure 1) is reduced as measured by less intense diffraction peaks.

The TEM image and the energy-filtered elemental TEM maps of Ce and silica for particle sample c are shown in Figure 4 and clearly reveal that Ce is located mainly at the core. The core is composed of mostly Ce compounds combined with a little amount of silica. The surrounding crust contains less Ce, and it is dominantly composed of silica.

A high resolution TEM image (Figure 5) for the core of a nanostructured particle shows that the core is composed

of multiple crystallites  $\sim 3 \text{ nm}$  in size. The inset selected area electron diffraction pattern (SAED) evidences the nanocrystalline cubic  $\text{CeO}_2$  structure.  $\text{CeCl}_3$  is easily hydrolyzed and further oxidized into Ce dioxide at high temperature. Figure 6 shows the energy dispersive X-ray (EDX) spectrum for the particle sample, indicating that most of the  $\text{CeCl}_3$  has been hydrolyzed and the  $\text{Cl}/\text{Ce}$  ratio is much less than the stoichiometric value of 3. The existence of various forms of Ce compounds and the cocondensation of hydrolyzed Ce species with silica acid limit the growth rate of crystallites and favor the formation of multicrystals instead of single crystals within the particles. Hence, the particle samples showed different colors, varying from white, purple, to yellow, with the increasing oxidation. As shown in Figure 7, the electron paramagnetic resonance experiment (EPR) for sample c (Figure 1) proved that only 32% of the Ce is in the state of  $\text{Ce}^{3+}$ . Care should be taken to keep the system from air during aerosol generation and succeeding calcination.

The evaporation of solvents, condensation kinetics, and the mass and heat transport together determine the final structure and the morphology. To better understand the formation process of the core-shell structure, the HCl concentration in precursor sol was intentionally increased 10 times for sample c, and the as-synthesized particles have an inner hollow structure composed of Ce compounds as shown in Figure 8. The reduced Ce salt solubility and quicker condensation/gelation due to accelerated hydrolysis and condensation under more acidic condition impede the ions' diffusion and seize the formed Ce salt crystallite before the ions diffuse inward along with the receding aqueous phase (effective aqueous diffusion coefficient for  $\text{CeCl}_3$  in CTAB-templated mesoporous silica is estimated at  $\sim 1.0 \times 10^{-14} \text{ m}^2/\text{s}$  at  $25^\circ\text{C}$ ). For comparison, a silica-free dilute ethanol solution of  $\text{Ce}(\text{NO}_3)_3 \cdot 6\text{H}_2\text{O}$  with a molar ratio of 664 EtOH:1  $\text{Ce}(\text{NO}_3)_3 \cdot 6\text{H}_2\text{O}$  was also sprayed into the particle-generating system as the precursor sol. Even though no silica species existed, the much lower solubility of  $\text{Ce}(\text{NO}_3)_3 \cdot 6\text{H}_2\text{O}$  in ethanol than in water and the much quicker evaporation of the more volatile ethanol in the absence of a silica network accounted for the early nucleation and succeeding crystallization. Decomposition of the salt and Oswald ripening during aerosol particle generation and succeeding calcination rendered the hollow particles spherical and uniform in thickness (Figure 8(a)). The hollow spherical particle size and the thickness depend on the precursor composition, salt type, and the solvent evaporation rate. Further calcination of the particles makes hollow spherical Ce oxide or Ce dioxide, depending on the calcination environment. A less volatile good solvent and lower heating temperature help form smaller hollow spherical particles of a thicker Ce species layer or even form solid Ce species particles. Figure 9 shows a snapshot of an aerosol particle collected at the end of a  $200^\circ\text{C}$  heating glass tube by a cryofinger kept at  $77 \text{ K}$ . With the evaporation of the solvents and a growing silica/surfactant gel layer, liquid sol recedes toward the droplet's center, and the silica/surfactant crystal phase starts the EISA into the ordered mesostructures.

A mechanism for the formation of the core-shell nanosstructure is proposed here. Starting from an homogeneous

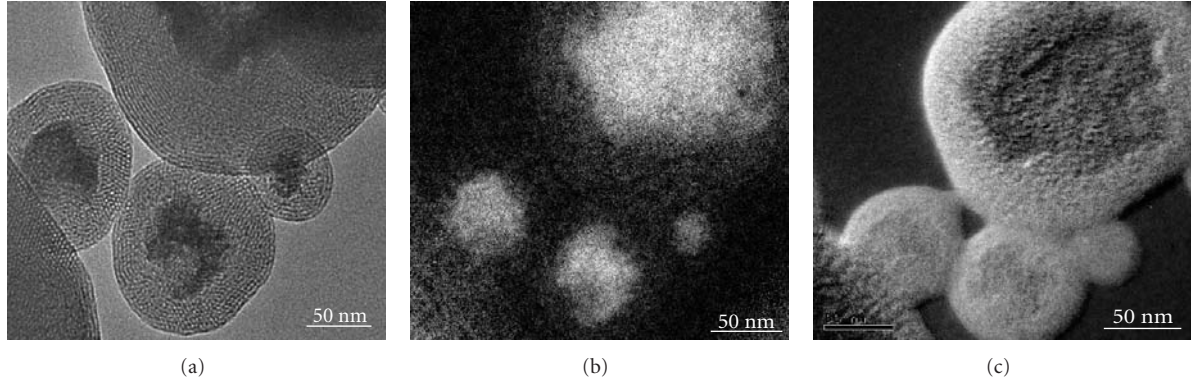


FIGURE 4: (a) TEM image, (b) energy-filtered Ce map, and (c) energy-filtered silica map for core-shell structured particle sample c (Figure 1).

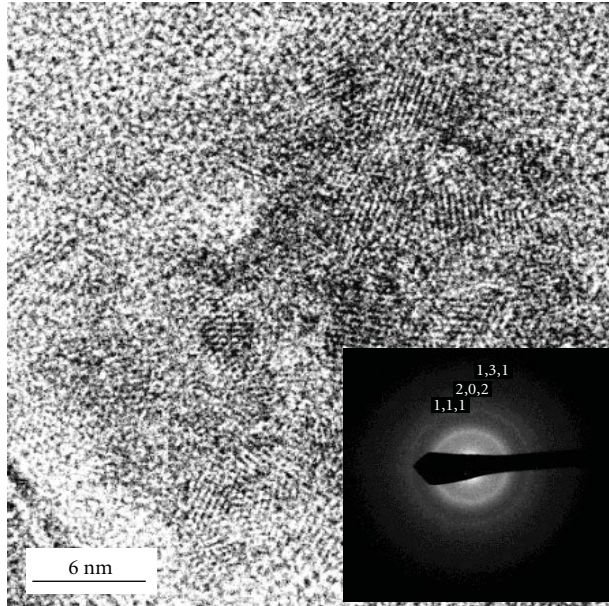


FIGURE 5: High resolution TEM image for the core part of nanostructured particle (inset is selected area electron diffraction (SEAD) pattern).

solution with the initial CTAB concentration much less than critical micelle concentration (CMC), the evaporation of solvents within each droplet creates growing radial gradients in surfactant, solvent, and salt concentrations that keep maximum concentrations for the surfactant and Ce salt at the droplet surface, resulting in an inward diffusion of the salt and surfactant and outward diffusion of solvents. The relatively lower mobility of surfactant due to the high molecular weight and the strong interaction (electrostatic and/or hydrogen bonding) with the silica network causes an inward drift of Ce species relative to the silica/surfactant phase of the droplet's core along with the receding aqueous phase. CMC is first exceeded at the droplet surface after a certain evaporation time. Once that happens, the CMC location continuously moves to the core of the droplet throughout the course of the EISA process. The surfactant enrichment induces silica-surfactant self-assembly into

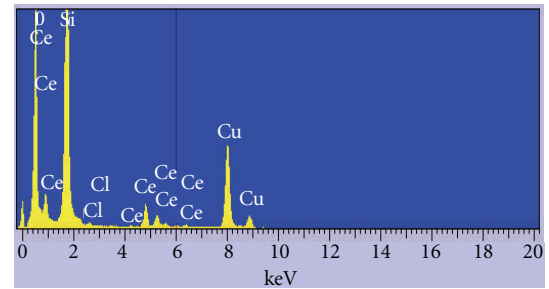


FIGURE 6: EDX spectrum of the core-shell particles observed on the surface of a carbon-coated copper grid.

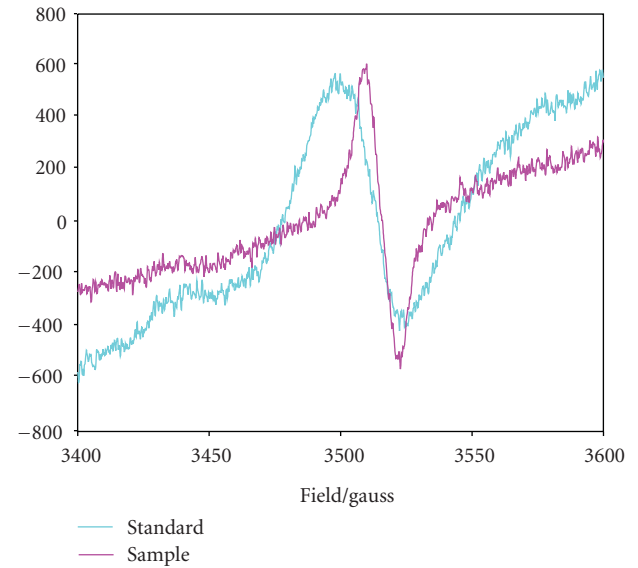


FIGURE 7: EPR spectra for  $\text{CeCl}_3$  standard and particle sample c (Figure 1).

micelles and their further organization into liquid-crystalline mesophases. The receding liquid-vapor interface causes silica-surfactant liquid-crystalline domains to grow radially inward, leaving a growing CTAB-templated liquid-crystalline

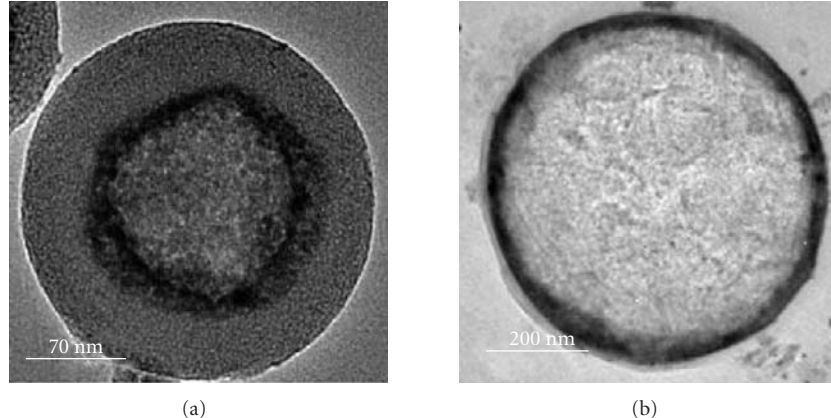


FIGURE 8: TEM images. (a) Hollow Ce/silica particle synthesized using precursor sol with molar ratio TEOS:EtOH:H<sub>2</sub>O:HCl:CTAB:CeCl<sub>3</sub> = 1:7.7:24.8:0.0125:0.18:0.18. (b) Hollow Ce oxide particles.

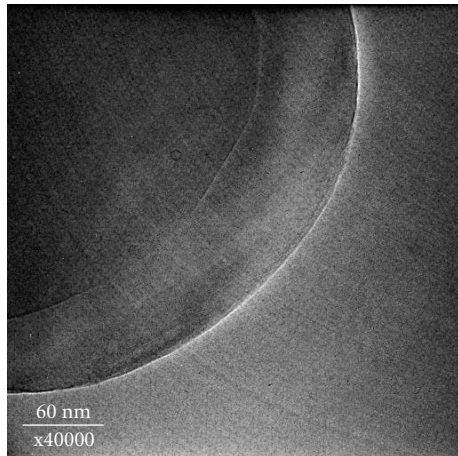
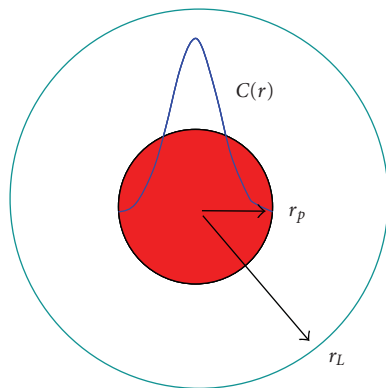


FIGURE 9: TEM image of a frozen evaporating droplet collected on a TEM copper grid by a cryofinger kept at 77 K.



SCHEME 1: Schematic of particle and droplet for diffusion.

state. The evaporation and resulting inward moving liquid-vapor interface boundary concentrate the salt solution. The partitioning of CeCl<sub>3</sub> in the CTAB-templated liquid-crystalline state is quite lower than that in the aqueous phase.

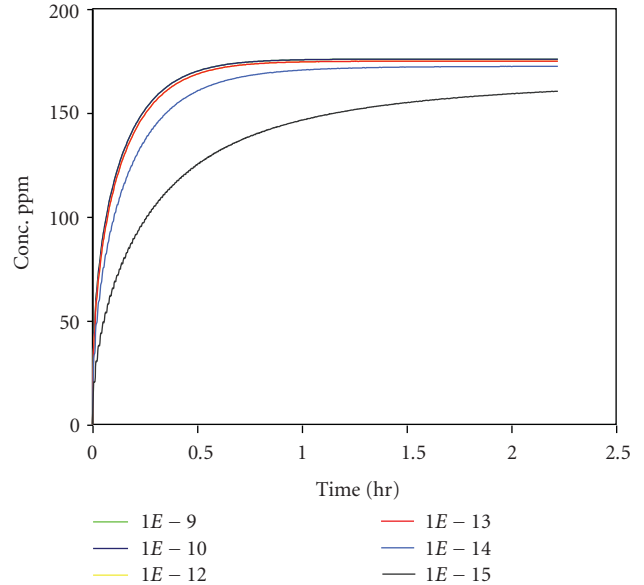


FIGURE 10: Effect of external diffusion ( $D_S$ ) on the release process.

As evaporation proceeds, part of the Ce salt is hydrolyzed into a less soluble Ce hydroxide due to the increased temperature and steep temperature gradient. Hydrolyzed Ce species may take part in the cocondensation along with the silica species. To a point of evaporation, less soluble Ce species nucleate and precipitate. The salt crystallites cannot grow into a big single crystal in the presence of other Ce species as impurity. The oversaturated Ce chloride and Ce hydroxide nucleate and precipitate are collected/filtered by increasingly dense liquid-crystalline mesophases. The held-up Ce species undergo continued hydrolysis and have a higher tendency to be hydrolyzed than the inner salt does due to the steep temperature gradient. However, they cannot continue to grow because of the limited Ce source and existence of the well-assembled bi-continuous CTAB/silica liquid-crystal phase. EDX data prove that smaller particles

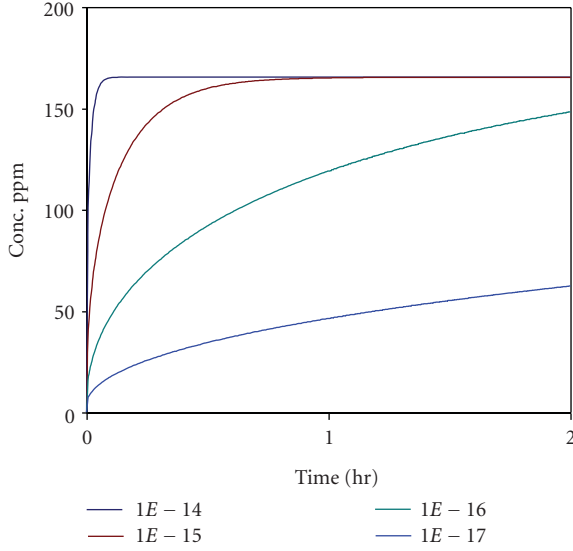


FIGURE 11: Effect on internal diffusion ( $D_p$ ) on the release process.

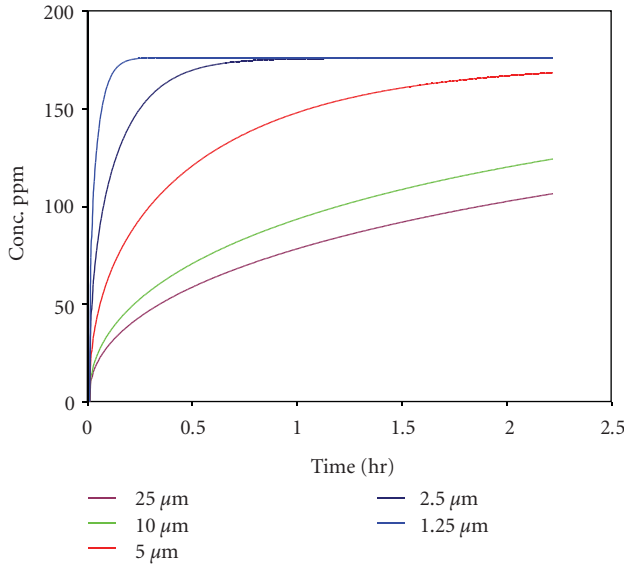


FIGURE 12: Effect of particle size on the release process at a dilution level of 100 and  $D_s = 1 \times 10^{-10} \text{ m}^2/\text{s}$ ,  $D_p = 1 \times 10^{-15} \text{ m}^2/\text{s}$ .

have a higher Ce/Cl ratio, and the ratio is lower at the center than at the crust. At the final period of evaporation, the vapor-liquid boundary shifts to the core. With the increasing temperature and salt concentration, Ce salt nucleation and crystal growth continues and causes phase separation of the mixture. Bigger Ce chloride/Ce hydroxide crystallites are formed at the center. The crystallites distort the assembled liquid-crystal phase and make the mesostructured silica less ordered at the center.

**2.1. Mathematical Modeling on Transport.** A simple model has been developed to evaluate the effective diffusivity. It is assumed that the particles have uniform size and each particle is surrounded symmetrically by an equal amount of

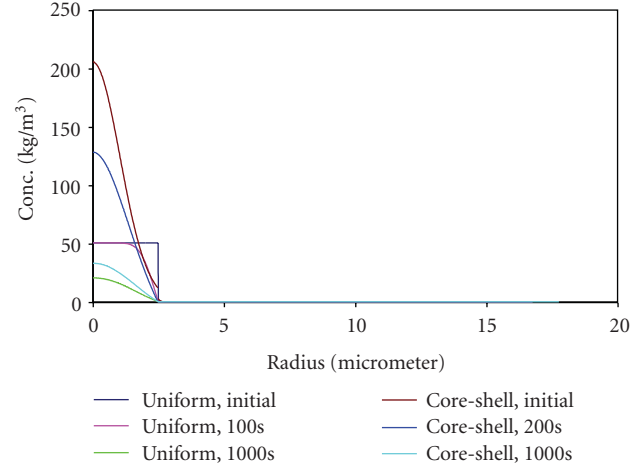


FIGURE 13: Inhibitor distribution of particles during the release process.

solution. As shown in Scheme 1, the particle has a radius of  $r_p$  and the outer boundary of the solution surrounding the particle is  $r_L$ . The concentration of solute in the particle and solution are  $C_p$  and  $C_s$ , respectively. The general diffusion equation (1) in spherical coordinates was used to begin the evaluation process:

$$\frac{\partial C}{\partial t} = D \frac{1}{r^2} \frac{\partial}{\partial r} \left( r^2 \frac{\partial C}{\partial r} \right). \quad (1)$$

A numerical method is used to evaluate the effective diffusion coefficient,  $D_{\text{eff}}$ , by comparing the calculated  $C_s-t$  curve with the measured release profiles based on initial conditions (2) and boundary conditions (3). Using the Crank-Nicolson method and assuming a constant  $D_{\text{eff}}$ , a matrix of the concentration profile at any time is obtained based on the initial conditions and boundary conditions. There is no limitation of  $D_{\text{eff}}\delta/(\delta r)^2 \leq 1/2$  for this method. The  $C_s$  value is averaged by an integration method and plotted as a function of time:

$$C_p(r, 0) = C_0(r), \quad C_s(r, 0) = C_{s,0}, \quad (2)$$

$$\begin{aligned} \left( \frac{\partial C_p}{\partial r} \right)_{r=0} &= \left( \frac{\partial C_s}{\partial r} \right)_{r=r_s} = 0, \\ D_{\text{eff}} \left( \frac{\partial C_p}{\partial r} \right)_{r=r_p} &= D_s \left( \frac{\partial C_s}{\partial r} \right)_{r=r_p}, \\ C_p(r_p, t) &= C_s(r_p, t). \end{aligned} \quad (3)$$

A few factors such as the effective diffusion coefficients in the particles ( $D_{\text{eff}}$ ) and in the bulk solution ( $D_s$ ), particle size effect, dilution level, and distribution of the active corrosion inhibitor have been taken into consideration.

Figure 10 shows how external diffusion,  $D_s$  (the diffusion in deionized (DI) water), affects the predicted release of 2.5  $\mu\text{m}$  particles with an uniformly distributed inhibitor. The dilution level, DI water/particle (weight), is kept as 100, and

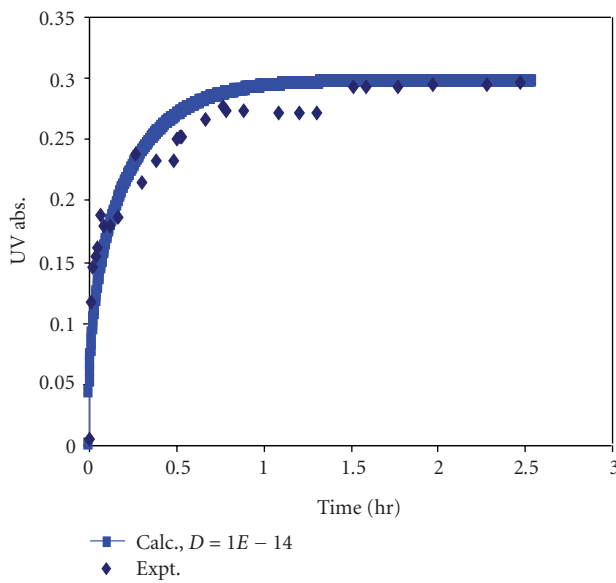


FIGURE 14: Release of Ce/silica particles in DI water.

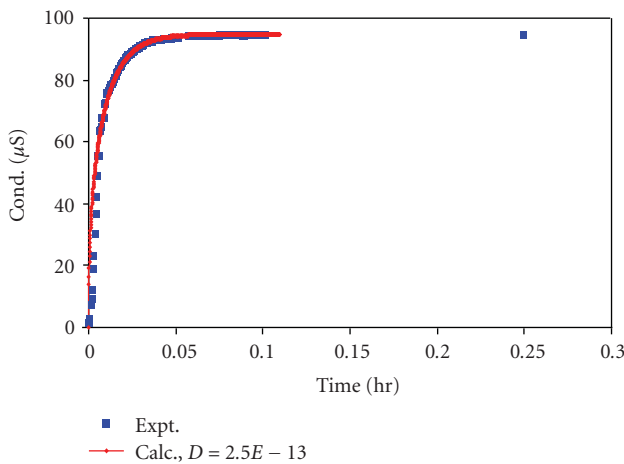


FIGURE 15: Release of NaCl/silica particles in DI water.

the internal diffusion coefficient,  $D_P$ , is set as  $1 \times 10^{-15} \text{ m}^2/\text{s}$ . We can see that external transport resistance can be negligible for a  $D_S/D_P$  greater than 100. The release curves are the same for the  $D_S$  of a value of  $1 \times 10^{-9}$ ,  $1 \times 10^{-10}$ , and  $1 \times 10^{-12} \text{ m}^2/\text{s}$ . The diffusion coefficients of ions in water are within this range. For the release process, stirring does not speed the release as also evidenced by the experiment. There is no need to obtain the exact value for  $D_S$ . We can select a  $D_S$  with a value  $10^{-10}$  or  $10^{-9} \text{ m}^2/\text{s}$  without compromising the accuracy of  $D_P$  in the simulation. The internal diffusion has also been examined. Figure 11 shows the effect of  $D_P$  on the release with a  $D_S$  fixed as  $1 \times 10^{-10} \text{ m}^2/\text{s}$ . The characteristic release time is reverse to  $D_P$ . The particles with a higher  $D_P$  show a quicker release. The release time also depends on the particle size. As shown in Figure 12, bigger particles show delayed release.

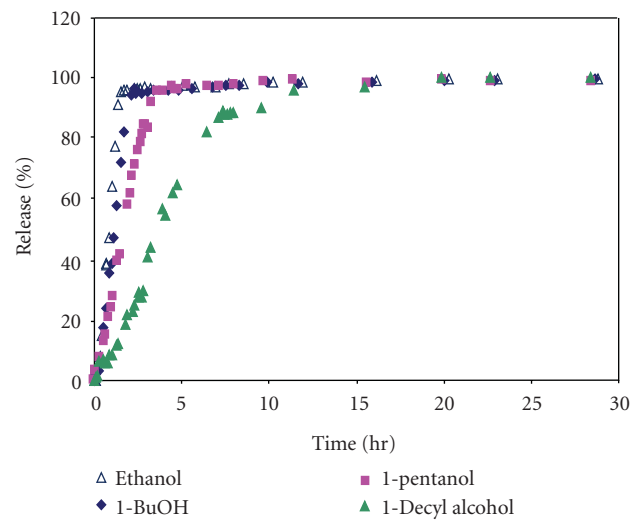


FIGURE 16: Ce release in alcohols for hydrophobic MTES-derived Ce/silica particles.

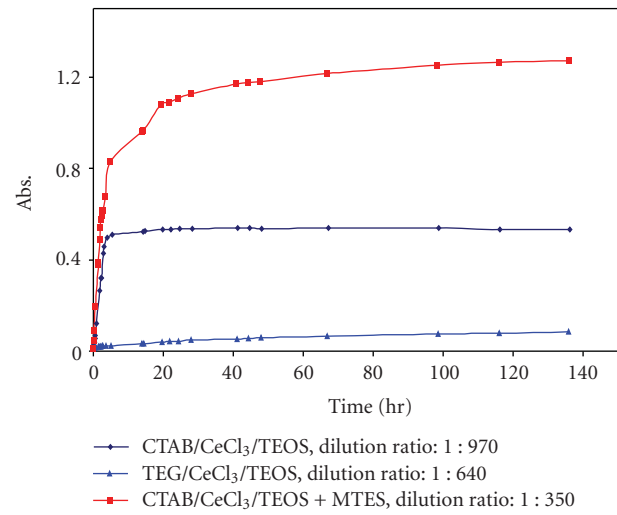


FIGURE 17: Effect of pore size and hydrophobicity on the release process.

Figure 13 shows simulated release results for  $2.5 \mu\text{m}$  particles using the same inhibitor loading. The  $D_S$  was set as  $1 \times 10^{-10} \text{ m}^2/\text{s}$ ,  $D_P$  as  $1 \times 10^{-15} \text{ m}^2/\text{s}$ , and a dilution level of 100. Compared to uniformly distributed particles, core-shell structured particles demonstrated delayed release, giving them a much longer service time.

To elucidate, actual effective diffusion coefficients for monodisperse Ce/silica and NaCl/silica particles of  $10 \mu\text{m}$  were made by a vibrating orifice aerosol generator (VOAG), TSI Atomizer 3076. The particles were dispersed in DI water. The solution concentrations were characterized by measuring the conductivity or absorbance of the solution at different release times. The release profiles are shown in Figures 14 and 15 for Ce/silica and NaCl/silica particles, respectively. The effective diffusion coefficient is  $2.5 \times 10^{-13} \text{ m}^2/\text{s}$  for NaCl and  $1.0 \times 10^{-14} \text{ m}^2/\text{s}$  for Ce<sup>3+</sup>.

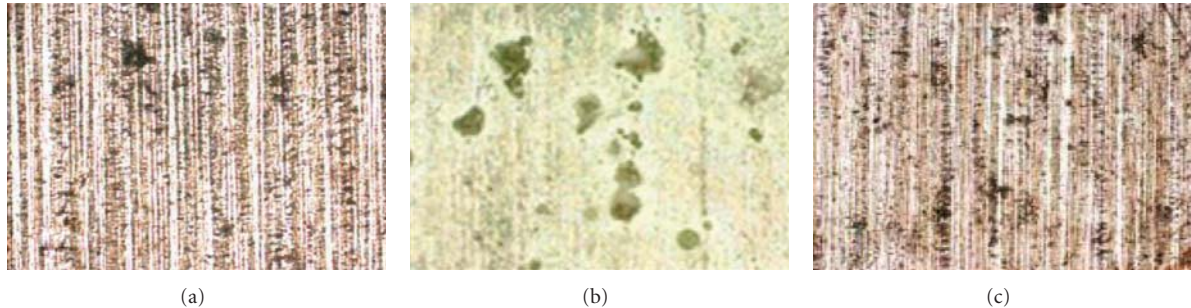


FIGURE 18: Optical microscopic images for aluminum alloy AA2024-T3 (scale bars = 25  $\mu\text{m}$ ). (a) Original uncorroded alloy. (b) Alloy corrosion after immersion in 0.05 M NaCl solution for 100 h. (c) Alloy corrosion after immersion in 0.05 M NaCl and Ce/silica particle solution for 100 h.

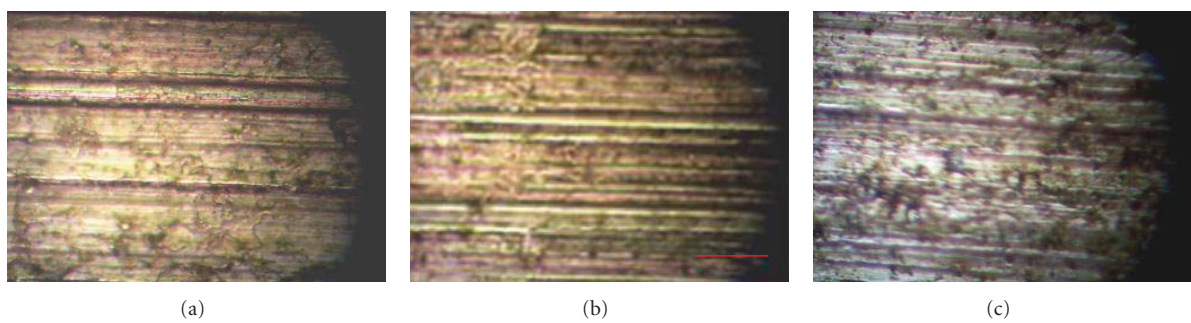


FIGURE 19: Optical microscopic images for aluminum alloy AA2024-T3 (scale bars = 25  $\mu\text{m}$ ). (a) Initial superhydrophobic Ce/silica-coated AA2024-T3 alloy. (b) Corrosion of superhydrophobic and Ce/silica-coated alloy after immersion in 0.05 M NaCl solution for 447 h. (c) Corrosion of bare, uncoated AA2024-T3 alloy after immersion in 0.05 M NaCl solution for 447 h.

The release behavior has been checked for the release rate in different n-alcohols. As shown in Figure 16, the constant release rate in various solvents over a long time suggests a solubility control for the release. The longer the solvent chain, the slower the release. The lower solubility and lower diffusion coefficient due to high viscosity account for the slower and straight release in high-carbon alcohols. For long-term corrosion inhibition, the inhibitors can be selected or converted to the form of suitable solubility in the corrosion medium. Highly soluble inhibitors are not a judicious choice from this point of view, but they may be if the inhibitor concentration is higher than the critical level required for inhibition.

Figure 17 shows release profiles for various Ce/silica particles. Methyltrimethoxysilane (MTES)/TEOS-derived hydrophobic particles and the microporous particles templated by triethylene glycol (TEG) demonstrated slow release. The estimated effective corrosion inhibition time for TEG-templated particles is greater than 3000 h.

The nanostructured core-shell Ce/silica particles were evaluated for corrosion inhibition of aluminum alloy AA2024-T3. As shown in Figure 18, without the nanostructured Ce/silica particles the alloy was easily corroded, and many pits were formed after 100 h of immersion in a 0.05 M NaCl solution; see Figure 18(b). However, dispersing 1 g of nanostructured silica particle b (Figure 1(b)) mixed into 100 mL 0.05 M of NaCl solution efficiently inhibited

corrosion (Figure 18(c)). A superhydrophobic coating layer containing the particles was also checked for corrosion protection. As can be seen in Figure 19, the coating protected the alloy well (Figure 19(b)). Without the core-shell particle coating, the alloy turned black and many pits appeared on the surface (Figure 19(c)). For comparison, the superhydrophobic coating without addition of the particles was checked for protection. Even though there was a lag time to sufficiently wet the sample, after being immersed in the solution for 447 h, the sample containing only the superhydrophobic turned black as well. The controlled release of the particles' corrosion inhibitors inhibited the corrosion and self-healed the corroded surface. This preliminary data clearly demonstrate the effectiveness of Ce<sup>3+</sup> as corrosion inhibitor for protecting alloy AA2024-T3, because the inhibitor is releasable from the nanostructured particles.

Mathematical modeling for Ce<sup>3+</sup> diffusion in the nanoporous particles demonstrated that the core-shell structure helps delay the release process compared to uniformly distributed Ce/silica particles. The evaluated effective diffusion coefficient in water is  $1.0 \times 10^{-14} \text{ m}^2/\text{s}$  at 25°C. The experiment also proved that the release can be controlled effectively by pore size and pore surface chemistry. Long-term corrosion inhibition can be realized by particles with small and hydrophobic pores. But a denser and thicker coating is needed for a water/ion transport barrier. Further corrosion test is being conducted for the particles that are

dispersed into a protective hydrophobic or epoxy coating layer for alloy AA2024-T3.

### 3. Conclusion

In conclusion, the nanostructured particles with a cerium core and mesoporous silica shell were synthesized via aerosol-assisted EISA and characterized using TEM, XRD, EPR, and so forth. We also demonstrated that the core-shell nanostructured particles were effective for corrosion inhibition of aluminum alloy AA2024-T3.

## 4. Experimental

**4.1. Materials.** All the chemicals were used as received. TEOS, MTES, cetyltrimethylammonium bromide (CTAB),  $\text{Ce}(\text{NO}_3)_3 \cdot 6\text{H}_2\text{O}$ , and  $\text{CeCl}_3 \cdot 7\text{H}_2\text{O}$  were obtained from Sigma-Aldrich (St. Louis, MO). Hydrochloric acid was VWR brand (VWR International, West Chester, PA), while absolute ethanol was obtained from Aaper (Brookfield, CT). DI water (Millipore, Billerica, MA) was used for all experiments. Aluminum alloy AA20240-T3 was obtained as a 3.0-mm-thick sheet from Davidson Aluminum & Metal Corporation (Deer Park, NY).

**4.2. Particles Synthesis.** Silica/surfactant aerosols were generated using a commercial atomizer (Model 9302A; TSI, Inc., St. Paul, MN) operated with nitrogen as a carrier/atomization gas. The procedure was the same as described by Lu et al. [14, 15]. It starts with a homogeneous solution of soluble silica, acid, and surfactant prepared in an ethanol/water solvent with an initial surfactant concentration much less than the CMC. The pressure drop at the pinhole was 20 psi. The temperature for three heating zones was kept at 400°C. Particles were collected on a Durapore Membrane Filter maintained at 80°C. The precursor sol molar ratio was 1 TEOS:7.7 EtOH:24.8 water:0.0125 HCl:0.18 CTAB:0–0.24  $\text{CeCl}_3$ . All calcination treatments were performed in a Lindberg tube furnace at 500°C for 5 h in forming gas (7%  $\text{H}_2$  and 93%  $\text{N}_2$ ) at a heating rate of 1°C/min.

**4.3. Characterization.** XRD spectra were recorded on a Siemens D-500 diffractometer, using Ni-filtered Cu  $\text{K}\alpha$  radiation with  $\lambda = 1.5406\text{ \AA}$ , a graphite monochromator, and a scintillation detector; data were refined using the JADE software package (Materials Data Inc., Livermore, CA).

TEM was performed using a JEOL 2010 HREM equipped with Oxford-Link X-ray energy-dispersive spectroscopy (EDS). A Gatan slow scan CCD camera was used for recording TEM images and electron diffraction patterns, operating at an accelerating voltage of 200 kV.

**4.4.  $\text{N}_2$  Isothermal Sorption.** Nitrogen isothermal adsorption was measured at 77 K on a Micromeritics ASAP 2010 porosimeter. Surface area was estimated by using the BET equation. The pore size was calculated using the BJH model.

**4.5. EPR Spectroscopy.** Electron paramagnetic resonance (EPR) analysis was operated using a Bruker Elexsys spectrometer with a microwave frequency of 9.8 GHz, a modulation amplitude of 10 GHz (100 kHz), a receiver gain of  $10^4$ , and a time constant of 82 ms. Samples were prepared by mixing ground pure  $\text{CeCl}_3$  or sample c with boron nitride. The standard sample made from pure  $\text{CeCl}_3$  had the same Ce loading as the sample c mixtures. The  $\text{Ce}^{3+}/(\text{Ce}^{3+} + \text{Ce}^{4+})$  was calculated by the ratio of integrated EPR signals of sample c to the standard sample.

Release of NaCl and  $\text{Ce}^{3+}$  from the particles was characterized by measuring the conductivity or the absorption using a conductivity meter or an UV-Vis spectrometer.

**4.6. Corrosion Inhibition Test.** The corrosion inhibition of particles was checked by dispersing the particles in 0.05 M NaCl aqueous solution. AA2024-T3 alloy coupons were immersed in the solution over 100 h followed by optical microscopy analysis.

**4.6.1. Superhydrophobic Coating on AA20240-T3.** Tetramethylorthosilicate (TMOS), methanol, ammonium hydroxide (35% wt), 3,3,3-trifluoropropyltrimethoxysilane (TFPT-MOS), and DI water were mixed in a molar ratio of 1:41.56:0.003:0.33:5.85. The mixture was stirred for 10 min and aged for 48 h at 50°C. The formed gel was washed with hexane and ethanol for 2 h. The gel was diluted with 1:1 ethanol and kept for sonification for reliquefaction. The redispersed sol was filtered through a 1 μm glass fiber filter. The filtered sol was mixed with core-shell Ce/silica particles (100:1 wt) and was spin-coated at 200 rpm for 20 s on a AA20240-T3 alloy substrate. AA2024-T3 alloy coupons with superhydrophobic coating containing core-shell particles were dipped in a 0.05 M NaCl aqueous solution for 447 h before optical microscopy analysis.

## Acknowledgments

We thank Dr. D. L. Tierney, Department of Chemistry and Biochemistry, Miami University, for assistance with EPR. Also we thank Dr. Scully Jr. of the University of Virginia for the help with the corrosion test. This work was supported by National Science Foundation NIRT Grant: EE C-0210835, NSF: EF-0830117, the Air Force Office of Scientific Research Award Number F49620-01-0168, the DOD MURI Program Contract 318651, NIH: U19 ES019528 (The Center for Nanobiology and Predictive Toxicology at the University of California, Los Angeles), and the NIH/Roadmap for Medical Research grant PHS 2 PN2 EY016570B. Sandia National Laboratories is a multiprogram laboratory operated by Sandia Corporation, a Lockheed Martin Company, for the United States Department of Energy's National Nuclear Security Administration under Contract DE-AC04-94AL85000.

## References

- [1] M. A. Jakab and J. R. Scully, "On-demand release of corrosion-inhibiting ions from amorphous Al-Co-Ce alloys," *Nature Materials*, vol. 4, no. 9, pp. 667–670, 2005.

- [2] J. V. Kloet, W. Schmidt, A. W. Hassel, and M. Stratmann, "The role of chromate in filiform corrosion inhibition," *Electrochimica Acta*, vol. 48, no. 9, pp. 1211–1222, 2003.
- [3] M. W. Kendig and R. G. Buchheit, "Corrosion inhibition of aluminum and aluminum alloys by soluble chromates, chromate coatings, and chromate-free coatings," *Corrosion*, vol. 59, no. 5, pp. 379–400, 2003.
- [4] R. L. Cook Jr., "Pigment-derived inhibitors for aluminum alloy 2024-T3," *Corrosion*, vol. 56, no. 3, pp. 321–333, 2000.
- [5] P. Campestrini, H. Terryn, A. Hovestad, and J. H. W. de Wit, "Formation of a cerium-based conversion coating on AA2024: relationship with the microstructure," *Surface and Coatings Technology*, vol. 176, no. 3, pp. 365–381, 2004.
- [6] M. Forsyth, K. Wilson, T. Behrsing, C. Forsyth, G. B. Deacon, and A. Phanangoankar, "Effectiveness of rare-earth metal compounds as corrosion inhibitors for steel," *Corrosion*, vol. 58, no. 11, pp. 953–960, 2002.
- [7] P. Traverso, R. Spinello, and L. Monaco, "Corrosion inhibition of Al 6061 T6/Al<sub>2</sub>O<sub>3</sub>p 10% (v/v) composite in 3.5% NaCl solution with addition of cerium (III) chloride," *Surface and Interface Analysis*, vol. 34, no. 1, pp. 185–188, 2002.
- [8] B. Davó and J. J. De Damborenea, "Use of rare earth salts as electrochemical corrosion inhibitors for an Al-Li-Cu (8090) alloy in 3.56% NaCl," *Electrochimica Acta*, vol. 49, no. 27, pp. 4957–4965, 2004.
- [9] R. G. Buchheit, H. Guan, S. Mahajanam, and F. Wong, "Active corrosion protection and corrosion sensing in chromate-free organic coatings," *Progress in Organic Coatings*, vol. 47, no. 3-4, pp. 174–182, 2003.
- [10] N. N. Voevodin, V. N. Balbyshev, M. Khobaib, and M. S. Donley, "Nanostructured coatings approach for corrosion protection," *Progress in Organic Coatings*, vol. 47, no. 3-4, pp. 416–423, 2003.
- [11] T. L. Metroke, O. Kachurina, and E. T. Knobbe, "Spectroscopic and corrosion resistance characterization of GLYMO-TEOS Ormosil coatings for aluminum alloy corrosion inhibition," *Progress in Organic Coatings*, vol. 44, no. 4, pp. 295–305, 2002.
- [12] T. L. Metroke, O. M. Kachurina, E. Stesikova, and E. T. Knobbe, "Composite coatings based on hybrid silicate and trivalent chromium conversion layers for aluminum alloy corrosion inhibition," *Abstracts of Papers of the American Chemical Society*, vol. 220, p. U341, 2000.
- [13] A. Pepe, M. Aparicio, S. Ceré, and A. Durán, "Preparation and characterization of cerium doped silica sol-gel coatings on glass and aluminum substrates," *Journal of Non-Crystalline Solids*, vol. 348, pp. 162–171, 2004.
- [14] Y. Lu, H. Fan, A. Stump, T. L. Ward, T. Rieker, and C. J. Brinker, "Aerosol-assisted self-assembly of mesostructured spherical nanoparticles," *Nature*, vol. 398, no. 6724, pp. 223–226, 1999.
- [15] Y. Lu, R. Ganguli, C. A. Drewien et al., "Continuous formation of supported cubic and hexagonal mesoporous films by sol-gel dip-coating," *Nature*, vol. 389, no. 6649, pp. 364–368, 1997.

## Research Article

# Photoresponsive Release from Azobenzene-Modified Single Cubic Crystal NaCl/Silica Particles

Xingmao Jiang,<sup>1</sup> Nanguo Liu,<sup>2</sup> Roger A. Assink,<sup>3</sup> Yingbing Jiang,<sup>4</sup> and C. Jeffrey Brinker<sup>1,3</sup>

<sup>1</sup> Department of Chemical and Nuclear Engineering and Center for Micro-Engineered Materials, The University of New Mexico, Albuquerque, NM 87106, USA

<sup>2</sup> SCB Innovation Accelerator, Dow Corning Corporation, 2200 W. Salzburg Road, P.O. Box 0994, Midland, MI 48686, USA

<sup>3</sup> Advanced Material Laboratory, Sandia National Laboratories, Albuquerque, NM 87185, USA

<sup>4</sup> Transmission Electron Microscopy Labs, The University of New Mexico, Albuquerque, NM 87131, USA

Correspondence should be addressed to C. Jeffrey Brinker, cjbrink@sandia.gov

Received 3 November 2010; Accepted 13 January 2011

Academic Editor: Yung-Sung Cheng

Copyright © 2011 Xingmao Jiang et al. This is an open access article distributed under the Creative Commons Attribution License, which permits unrestricted use, distribution, and reproduction in any medium, provided the original work is properly cited.

Azobenzene ligands were uniformly anchored to the pore surfaces of nanoporous silica particles with single crystal NaCl using 4-(3-triethoxysilylpropylureido)azobenzene (TSUA). The functionalization delayed the release of NaCl significantly. The modified particles demonstrated a photocontrolled release by trans/cis isomerization of azobenzene moieties. The addition of amphiphilic solvents, propylene glycol (PG), propylene glycol propyl ether (PGPE), and dipropylene glycol propyl ether (DPGPE) delayed the release in water, although the wetting behavior was improved and the delay is the most for the block molecules with the longest carbon chain. The speedup by UV irradiation suggests a strong dependence of diffusion on the switchable pore size. TGA, XRD, FTIR, and NMR techniques were used to characterize the structures.

## 1. Introduction

Mesoporous silica with well-defined structures has attracted much attention for controlled release of dyes [1], drugs [2, 3], perfumes, and flavorings [4, 5]. Recently nanoporous spherical silica particles with ordered structures have been prepared by aerosol-assisted self-assembly [6]. Ordered mesoporous core-shell silica particles with single crystal NaCl nanocube or Ce core have also been synthesized [7, 8], and the core-shell structure [8] has been shown effective for corrosion inhibition of aluminum alloy AA2024-T3. The functionalization of pore surfaces by organic groups regulates the hydrophobicity and therefore the release behavior, and the hydrothermal stability of the silica particles has also been improved. Long-term (years) protection of metals and alloys requires the release of the encapsulated corrosion inhibitors to the target surface in a well-controlled manner. Tailorable inherent structure properties such as particle size, pore size, pore connectivity, structure stability, and surface chemistry, are key factors for release behavior. Active transport triggered by external stimuli such as light [4], pH

[9], temperature [10], and electric field [11] are required for a lot potential applications such as drug release, optical devices, and sensors. It also provides additional flexibility for release control. Azobenzene ligands are well known for their active response to light and heat. For example, the dipole moment of the azobenzene group can be reversibly switched between approximately 3D and 0D by cis-trans photoisomerization, resulting in an optical control of ion channel gating for  $\text{Cs}^+$  and  $\text{Na}^+$  movement through the pores [12]. The photoswitchable gates based on the extended trans and the shorter cis configurations of photoisomerizable azobenzene groups in the pore blockers regulated  $\text{K}^+$  flow [13] in engineered  $\text{K}^+$  channel, resulting in a remote control of neuronal firing. Azobenzene moieties bonded to cross-linked membrane reversibly changed the transport number of sulfate ions relative to chloride ions in electrodialysis [14]. The adsorbed azobenzene in zeolite-azobenzene membranes of ZSM-5 (MFI) and Faujasite-type (FAU) zeolites changed gas permeation by photoinduced switching [15]. Azobenzene-functionalized glassy polymer films demonstrated a photoresponsive gas permeability [16]. Liu et al.

succeeded in making a photoresponsive nanocomposite thin film by (evaporation-induced) surfactant-directed self-assembly (EISA) of an azobenzene-modified silane, 4-(3-triethoxysilylpropylureido)azobenzene (TSUA), and tetraethyl orthosilicate (TEOS) [17]. They went further to investigate the photoregulation of mass transport through a photoresponsive azobenzene-modified nanoporous membrane [18]. The optically switchable conformation of azobenzene ligands controlled the effective pore size and, correspondingly, transport behavior on the nanoscale.

In this paper we modified the pore surfaces of mesoporous silica particles of single crystal NaCl cube with TSUA. The extent of condensation increased from 92.4% to 96.45% after the modification. The functionalization delayed the release of NaCl significantly. The modified particles demonstrated a photocontrolled release. The photoresponsive release suggests a strong dependence of diffusion on the switchable pore size. The added amphiphilic solvents, propylene glycol, propylene glycol propyl ether, and dipropylene glycol propyl ether delayed the release in water, although the wetting behavior was improved, and the delay is the most for the block molecules with the longest carbon chain. A few techniques such as TGA, XRD, FTIR, NMR, and TEM were used to characterize the structures.

## 2. Experiment

**2.1. Materials.** TSUA was prepared in the method described elsewhere [19]. All chemicals were used as received. Tetraethyl orthosilicate (TEOS) and cetyltrimethylammonium bromide (CTAB), toluene, propylene glycol, propylene glycol propyl ether (98.5%), and dipropylene glycol propyl ether (98.5%) were obtained from Aldrich; NaCl was manufactured by J. T. Baker. Hydrochloric acid was VWR brand, while absolute ethanol was obtained from Aaper. Millipore deionized water was used for all experiments.

**2.2. Particles Synthesis.** Ordered mesoporous silica particles of single crystal NaCl cube were generated from TEOS as described in a previous work [9]. 1.07 g TSUA was added into 200 ml toluene dried beforehand by molecular sieve 4 Å under stirring at 35°C. After the dissolution of TSUA in the solution, 2.5 g of the NaCl/silica particles were added into the solution refluxed at 90°C for 12 hr. The particles were centrifuged and washed six times using large quantity of hexane, and vacuum dried at 70°C for 2 days.

**2.3. Characterizations.** The mesostructures of the particles were verified using a combination of powder X-ray diffraction (XRD), high resolution transmission electron microscopy (HRTEM) and Fourier transform infrared spectroscopy (FT-IR), thermogravimetric analysis/differential thermal analysis (TGA/DTA). The experiment procedures are the same as described elsewhere [7, 8]. For TEM nitrogen mapping, the particles were first dispersed in a toluene solution of poly(methyl methacrylate), dried, and then microtomed into 50 nm thin films.

NMR characterization of the particles was performed on a Bruker DRX 400 MHz instrument. The release behaviors

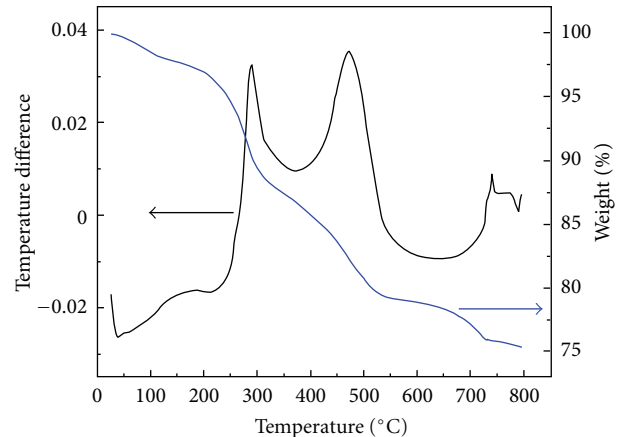


FIGURE 1: TGA/DTA plot of azobenzene-modified sample under air.

of the particles was checked by monitoring the conductivity of the solutions using VWR Corning 316 conductivity meter. Corning Acquire software was used to automatically record the data. A 100 ml quartz beaker from Ace Glass was used for UV ( $\lambda = 360$  nm) irradiation, and a 200 W Hg-Xe arc lamp (ORIEL, model 66002) with optical filters was used as the light source.

## 3. Results and Discussion

As shown in Figure 1, the TGA/DTA of photoresponsive mesoporous materials in air showed about 10.5% weight loss from 177 to 357°C for dehydration of silanols in the silica structures and about 9.5% weight loss from 383 to 666°C and the decomposition of the azobenzene ligands. Considering the original NaCl/silica particles of a surface area of  $796 \text{ m}^2/\text{g}$  and pore size of 2.05 nm, the surface coverage is estimated to be about 0.67 azobenzene ligand  $\text{nm}^{-2}$ , smaller than the value, 1.2 azobenzene ligands  $\text{nm}^{-2}$ , reported for the photoresponsive nanocomposite formed by direct self-assembly of an azobenzene-modified silane [17].

The average axial distance in the pores between two adjacent azobenzene ligands is 2.3 Å. The modification of pore surface is effective to anchor chemically the azobenzene ligands to pore surfaces.

The FTIR spectra were shown in Figure 2. The sample demonstrated strong absorption near  $1047 \text{ cm}^{-1}$  due to the  $-\text{Si}-\text{O}-\text{Si}-$  structure and broad absorption near 790 and  $3478 \text{ cm}^{-1}$  arising from Si-OH structure in the samples. There are three characteristic vibrational bands of the  $-\text{NH}-\text{CO}-\text{NH}-$  group:  $= 3344 \text{ cm}^{-1}$  (N-H stretch),  $1654 \text{ cm}^{-1}$ , and  $1543 \text{ cm}^{-1}$  (C=O, stretching of amides). Besides, the sample showed characteristic absorption near  $1200 \text{ cm}^{-1}$  for aromatic amine and vibrational bands: 3030, 2945,  $2928 \text{ cm}^{-1}$  for aromatic C-H stretch. TEM image for azobenzene-modified particles in Figure 3 showed the ordered porous silica structures with single crystal NaCl. The count mean diameter for the particles is  $\sim 200$  nm, and the geometric standard deviation is  $\sim 2$ . The single crystal NaCl has a size nearly half of the particle size. The silica shell thickness is around one-fourth of the particle size. The

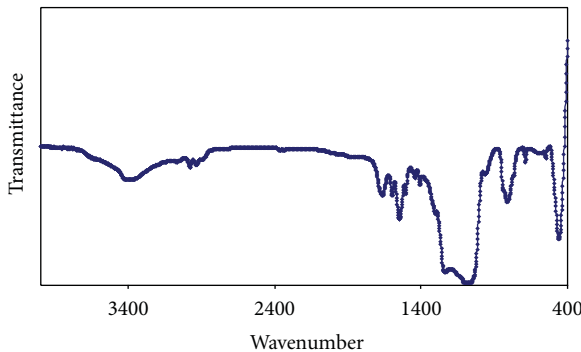
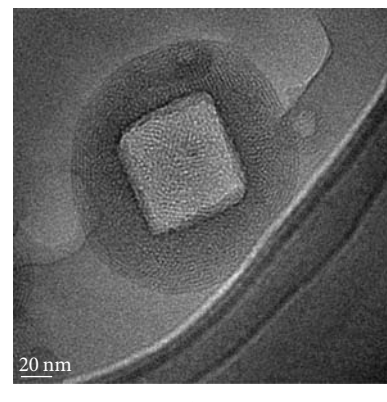


FIGURE 2: FTIR spectrum for azobenzene-modified sample.



(a)

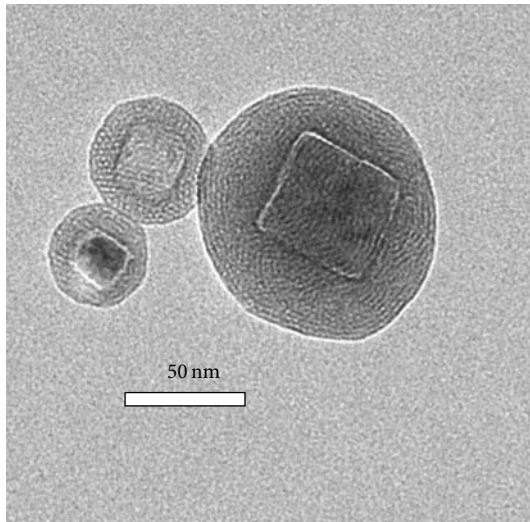
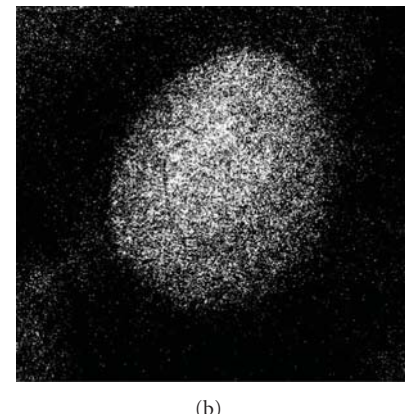


FIGURE 3: TEM image for azobenzene-modified sample.

TEM image obtained from ultramicrotomed sections for modified particle samples was shown in Figure 4. Based on the N mapping for the 50 nm ultrathin layer of microtomed sample, TSUA molecules penetrated well inside the particles, and the azobenzene ligands were covalently anchored within the particles uniformly.

The XRD patterns for the samples as shown in Figure 5 indicated that after the modification the particles keep both the orders for porous silica and crystal NaCl as also demonstrated in Figure 3.

As shown in Figure 6 and Tables 1 and 2, studies of the modified particles by  $^{29}\text{Si}$  MAS NMR spectroscopy showed T1, T2, T3, Q2, Q3, and Q4 resonances at  $\delta = -51, -57.6, -65.1, -90.6, -99.7$ , and  $-108.4$  ppm, respectively. 10.33% of the Si were T's, and 89.67% were Q's (the ratio of Si in T's to Q's is  $\sim 1:12$  based on TGA/DTA data). The extent of condensation of the T species was 54.2%, and the extent of condensation of Q species increased from initial 92.4% to 96.45%, while only 0.49% of Q2 existed for modified particles. The treatment is effective to convert the  $-\text{OH}$  groups on pore surfaces and provided covalent attachment of the azobenzene ligands to the pore surface. The modified particles showed a delayed and



(b)

FIGURE 4: Energy-filtered N mapping for cross-sectioned azobenzene-modified particle. (a) TEM image, (b) N mapping.

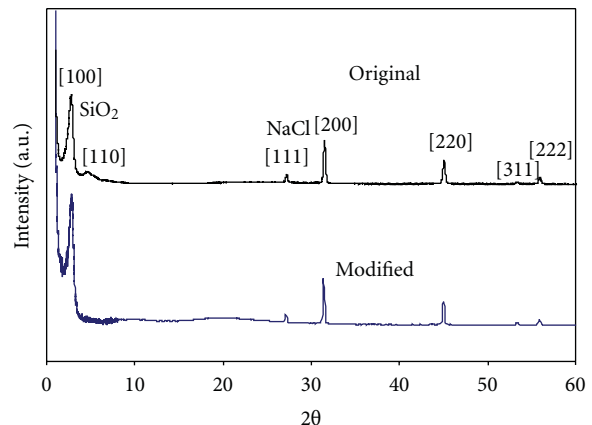


FIGURE 5: XRD patterns for NaCl-silica core-shell structured particle samples.

photoresponsive release at  $25^\circ\text{C}$  under a stirring at 300 rpm. Before the modification, the release is very quick; within 1 minute, all the NaCl molecules diffused into the solution (Figure 7). The external transport resistance is not negligible for the situation. As shown in Figure 7, the addition of long molecule solvent such as DPGPE delayed the release to some degree. However, after the modification, the particles showed a far different behavior. As shown in Figure 8, the releases

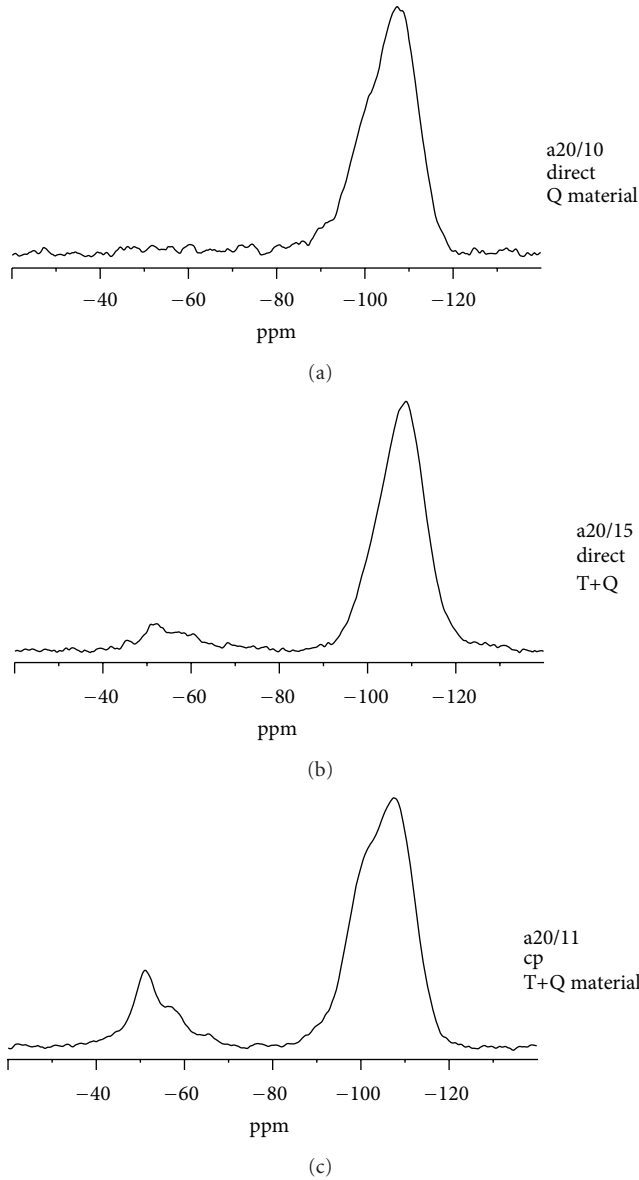


FIGURE 6:  $^{29}\text{Si}$  NMR spectra of  $\text{NaCl}/\text{SiO}_2$  samples before/after modification.

were delayed greatly. The concentrations got stabilized after ~4–150 hr release for modified particles in DI water added with various solvents. The delay depended on the amount and the molecular size of the added solvent. As common used amphiphilic solvents for painting, propylene glycol (PG), propylene glycol propyl ether (PGPE), and dipropylene glycol propyl ether (DPGPE) improved the wetting of the particles in DI water. For the same amount of amphiphilic solvent added, PG delayed the least release; the characteristic release time was ~50 hr for PGPE and ~150 hr for DPGPE, suggesting a strong dependence of the diffusion on pore size. The bigger the block molecule in the pore, the more delayed release. The amount of the added solvent was also important for the delayed release. By comparison of the release profiles in aqueous solution of PG added 3 g and 10 g, respectively,

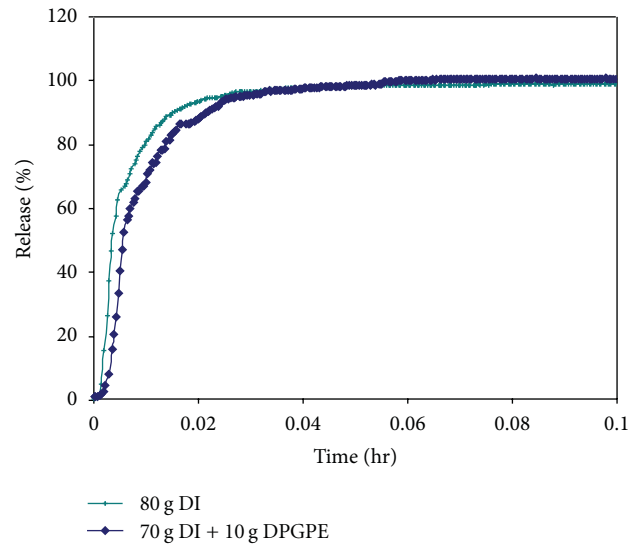


FIGURE 7: Release profiles for  $\text{NaCl}/\text{silica}$  particles in DI water and water solution of DPGPE.

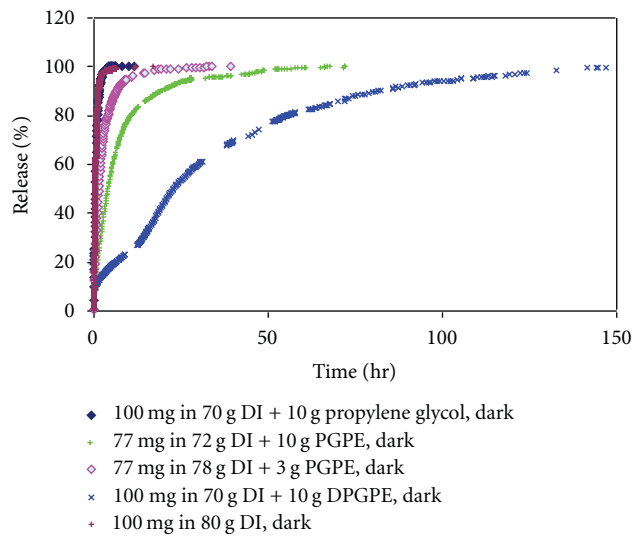


FIGURE 8: Release profiles for azobenzene-modified  $\text{NaCl}/\text{silica}$  particles in various solutions.

TABLE 1: NMR results for unmodified particle sample.

Si species	Shift (ppm)	Linewidth (Hz)	Integral (%)
Q2	-90.6	506	4.14
Q3	-98.9	620	22.15
Q4	-107.7	812	73.71

the release delay depended on the amount added. The more added PG, the more the delayed release.

The photoresponse of the modified particles has been checked for the release. The UV irradiation speeded up the release process as shown in Figure 9. The equilibration time in DI water was reduced from ~4 hr to ~1.5 hr for the

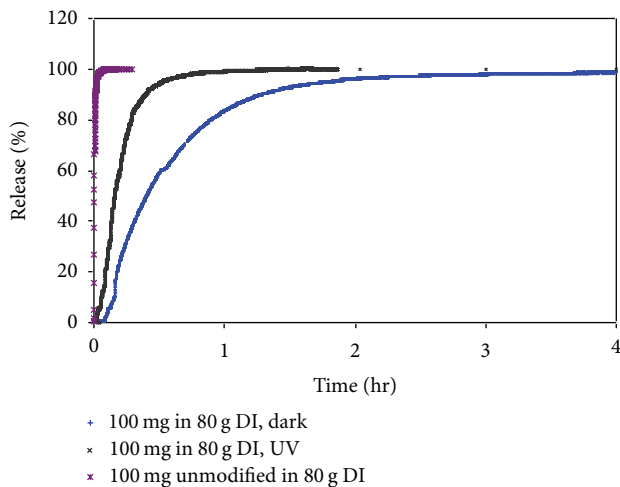


FIGURE 9: Photoresponsive release of azobenzene-modified NaCl/silica particles in DI water. The release from unmodified NaCl/silica particles is shown for comparison.

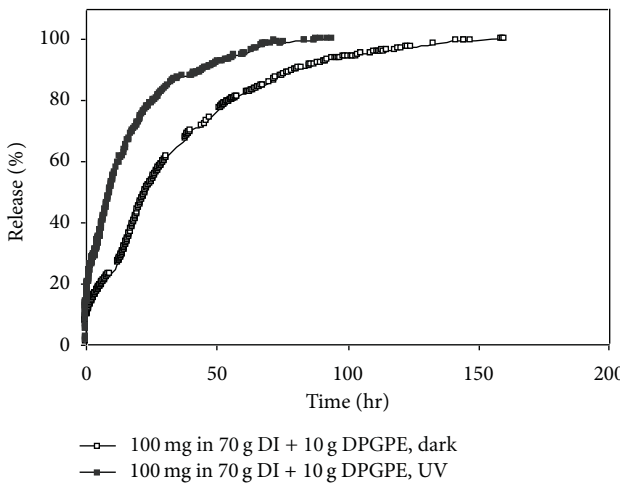


FIGURE 10: Photoresponsive release of azobenzene-modified NaCl/silica particles in DPGPE/water solution.

TABLE 2: NMR results for azobenzene-modified particle sample.

Si species	Shift (ppm)	Linewidth (Hz)	Integral (%)
T1	-51.0	500	5.15
T2	-57.6	500	3.89
T3	-65.1	500	1.29
Q2	-90.6	589	0.49
Q3	-99.7	690	11.75
Q4	-108.4	875	77.42

irradiation. As shown in Figure 10, when DPGPE was added, the equilibration time decreased from  $\sim$ 90–150 hr. The releases demonstrated a strong photoresponsive behavior for modified particles.

## 4. Conclusions

Azobenzene ligands have been successfully anchored uniformly to the pore surface. After the modification, the Q2 has reduced to only 0.49%, and the extent of condensation for Q species is as high as 96.45%, only 0.49% of Q2 existed, and the particles kept the ordered structures. The trans/cis transformation of the azobenzene moieties under UV irradiation realized the photocontrolled release. The addition of amphiphilic solvent into the release medium improved the wetting. However, the releases were delayed greatly after the addition of long block molecules. The delay depended on the amount and the size of the solvent added. This provides an extra external control of release in addition to UV irradiation. Long molecule solvents or polymers can be used as blocker to adjust the release behavior for a long-term controlled release.

## Acknowledgments

This work was supported by National Science Foundation NIRT Grant: EE C-0210835, NSF: EF-0830117, NSF:EF-0830117, NIH: U19 ES019528 (UCLA Center for Nanobiology and Predictive Toxicology), the Air Force Office of Scientific Research award no. F49620-01-0168, the DOD MURI Program Contract 318651, and the NIH/Roadmap for Medical Research Grant PHS 2 PN2 EY016570B. Sandia National Laboratories is a multiprogram laboratory operated by Sandia Corporation, a Lockheed Martin Company, for the United States Department of Energy's National Nuclear Security Administration under Contract DE-AC04-94AL85000.

## References

- [1] K. Suzuki, T. Yumura, Y. Tanaka, and M. Akashi, "Thermo-responsive release from interpenetrating porous silica-poly(N-isopropylacrylamide) hybrid gels," *Journal of Controlled Release*, vol. 75, no. 1-2, pp. 183–189, 2001.
- [2] S. Falaize, S. Radin, and P. Ducheyne, "In vitro behavior of silica-based xerogels intended as controlled release carriers," *Journal of the American Ceramic Society*, vol. 82, no. 4, pp. 969–976, 1999.
- [3] B. G. Trewyn, C. M. Whitman, and V. S. Y. Lin, "Morphological control of room-temperature ionic liquid templated mesoporous silica nanoparticles for controlled release of antibacterial agents," *Nano Letters*, vol. 4, no. 11, pp. 2139–2143, 2004.
- [4] N. K. Mal, M. Fujiwara, Y. Tanaka, T. Taguchi, and M. Matsukata, "Photo-switched storage and release of guest molecules in the pore void of coumarin-modified MCM-41," *Chemistry of Materials*, vol. 15, no. 17, pp. 3385–3394, 2003.
- [5] S. R. Veith, E. Hughes, and S. E. Pratsinis, "Restricted diffusion and release of aroma molecules from sol-gel-made porous silica particles," *Journal of Controlled Release*, vol. 99, no. 2, pp. 315–327, 2004.
- [6] Y. Lu, H. Fan, A. Stump, T. L. Ward, T. Rieker, and C. J. Brinker, "Aerosol-assisted self-assembly of mesostructured spherical nanoparticles," *Nature*, vol. 398, no. 6724, pp. 223–226, 1999.
- [7] X. M. Jiang et al., submitted.
- [8] X. M. Jiang et al., submitted.

- [9] Y. Shin, J. H. Chang, J. Liu, R. Williford, Y. K. Shin, and G. J. Exarhos, "Hybrid nanogels for sustainable positive thermosensitive drug release," *Journal of Controlled Release*, vol. 73, no. 1, pp. 1–6, 2001.
- [10] S. R. Sershen, S. L. Westcott, N. J. Halas, and J. L. West, "Temperature-sensitive polymer-nanoshell composites for photothermally modulated drug delivery," *Journal of Biomedical Materials Research*, vol. 51, no. 3, pp. 293–298, 2000.
- [11] S. Murdan, "Electro-responsive drug delivery from hydrogels," *Journal of Controlled Release*, vol. 92, no. 1-2, pp. 1–17, 2003.
- [12] V. Borisenko, D. C. Burns, Z. Zhang, and G. A. Woolley, "Optical switching of ion-dipole interactions in a gramicidin channel analogue," *Journal of the American Chemical Society*, vol. 122, no. 27, pp. 6364–6370, 2000.
- [13] M. Banghart, K. Borges, E. Isacoff, D. Trauner, and R. H. Kramer, "Light-activated ion channels for remote control of neuronal firing," *Nature Neuroscience*, vol. 7, no. 12, pp. 1381–1386, 2004.
- [14] T. Sata, Y. Shimokawa, and K. Matsusaki, "Preparation of ion-permeable membranes having an azobenzene moiety and their transport properties in electrodialysis," *Journal of Membrane Science*, vol. 171, no. 1, pp. 31–43, 2000.
- [15] K. Weh, M. Noack, K. Hoffmann, K. P. Schröder, and J. Caro, "Change of gas permeation by photoinduced switching of zeolite-azobenzene membranes of type MFI and FAU," *Microporous and Mesoporous Materials*, vol. 54, no. 1-2, pp. 15–26, 2002.
- [16] M. Kameda, K. Sumaru, T. Kanamori, and T. Shinbo, "Photoresponse gas permeability of azobenzene-functionalized glassy polymer films," *Journal of Applied Polymer Science*, vol. 88, no. 8, pp. 2068–2072, 2003.
- [17] N. Liu, K. Yu, B. Smarsly, D. R. Dunphy, Y. B. Jiang, and C. J. Brinker, "Self-directed assembly of photoactive hybrid silicates derived from an azobenzene-bridged silsesquioxane," *Journal of the American Chemical Society*, vol. 124, no. 49, pp. 14540–14541, 2002.
- [18] N. Liu, D. R. Dunphy, P. Atanassov et al., "Photoregulation of mass transport through a photoresponsive azobenzene-modified nanoporous membrane," *Nano Letters*, vol. 4, no. 4, pp. 551–554, 2004.
- [19] N. Liu, D. R. Dunphy, M. A. Rodriguez, S. Singer, and J. Brinker, "Synthesis and crystallographic structure of a novel photoresponsive azobenzene-containing organosilane," *Chemical Communications*, vol. 9, no. 10, pp. 1144–1145, 2003.

## Research Article

# A Novel Aerosol Method for the Production of Hydrogel Particles

Diana Guzman-Villanueva,<sup>1,2</sup> Hugh D. C. Smyth,<sup>2</sup>  
Dea Herrera-Ruiz,<sup>1</sup> and Ibrahim M. El-Sherbiny<sup>2,3</sup>

<sup>1</sup> Facultad de Farmacia, Universidad Autónoma del Estado de Morelos, 62209 Cuernavaca MOR, Mexico

<sup>2</sup> Division of Pharmaceutics, College of Pharmacy, The University of Texas at Austin, Austin, TX 78712, USA

<sup>3</sup> Polymer Laboratory, Faculty of Science, Mansoura University, Mansoura 35516, Egypt

Correspondence should be addressed to Hugh D. C. Smyth, hsmyth@mail.utexas.edu

Received 27 August 2010; Accepted 1 December 2010

Academic Editor: Yung-Sung Cheng

Copyright © 2011 Diana Guzman-Villanueva et al. This is an open access article distributed under the Creative Commons Attribution License, which permits unrestricted use, distribution, and reproduction in any medium, provided the original work is properly cited.

A novel method of generating hydrogel particles for various applications including drug delivery purposes was developed. This method is based on the production of hydrogel particles from sprayed polymeric nano/microdroplets obtained by a nebulization process that is immediately followed by gelation in a crosslinking fluid. In this study, particle synthesis parameters such as type of nebulizer, type of crosslinker, air pressure, and polymer concentration were investigated for their impact on the mean particle size, swelling behavior, and morphology of the developed particles. Spherical alginate-based hydrogel particles with a mean particle size in the range from 842 to 886 nm were obtained. Using statistical analysis of the factorial design of experiment it was found that the main factors influencing the size and swelling values of the particles are the alginate concentration and the air pressure. Thus, it was demonstrated that the method described in the current study is promising for the generation of hydrogel particles and it constitutes a relatively simple and low-cost system.

## 1. Introduction

Polymeric nanoparticles have been widely used as carriers in drug delivery systems because they offer several advantages over larger particles including a larger surface area, increased dissolution rate, enhanced bioavailability of insoluble drugs, mass transfer from the particles into the surrounding medium, and ability to cross the cellular membranes [1, 2]. Thus, nanoparticles have become a new formulation option, specifically in the aerosol delivery field, where the aerosol droplet size is crucial to the efficacy of inhalation therapy [3].

Technologies such as supercritical fluid extraction (SCF), electrospray, high-pressure homogenization, solvent displacement, and spray drying have been commonly used to produce nano- and microparticles [1, 3, 4]. Supercritical fluid extraction (SCF) is a method that depends on the coprecipitation of a drug and polymer together using mainly carbon dioxide as a supercritical fluid (nonsolvent), to extract the solvent from the drug emulsion or solution. However, when highly viscous solutions are used, unsteady

particle size, particle agglomeration, and incomplete encapsulation can occur which makes the supercritical fluid extraction a very material-specific method [4–6]. Electrospray is a method that depends on dispersion of liquids into small charged droplets when an electrostatic field is applied and it was first described by Lord Rayleigh. The electrospray setup comprises a nozzle connected to a high-voltage supply and to the liquid or solution to be atomized. Once the high electrical field is applied, the electrostatic forces created disperse a liquid stream into highly fine charged droplets. Experiments using electrospray method have demonstrated that particles as small as 250 nm can be produced. However, a wide droplet size distribution can be produced as a consequence of fission of droplets. Also, this method is restricted to high-voltage operation, rising safety and reliability issues in the consumer use [7–9]. High-pressure homogenization is another method that has been used to produce nanosuspensions. Here, an aqueous solution containing the drug is passed through a narrow homogenization gap using very high velocities [10, 11]. The size reduction of the particles occurs due to

induced cavitation forces within the fluid. The main disadvantage of this method is the temperature-induced drug degradation [12]. Solvent displacement is considered a simple method for preparation of nanodispersions or nanospheres. This method involves the mixing of an aqueous phase in presence of an emulsifier with an organic solution containing the dissolved active compound and the polymer [13]. The rapid diffusion of the organic solvent in the aqueous medium leads to an instantaneous precipitation of nanoparticles. Even though solvent displacement offers a rapid obtaining of nanoparticles, the use of suitable water-miscible solvents to produce spontaneous emulsification may make it difficult. Another limitation of this method is that it is used mainly for lipophilic drugs because of the miscibility of solvent with the aqueous medium [14]. Spray drying is a process that force fluid through a nozzle generating a mist, that dried produces a fine powder, and it has become in one of the widely used techniques for the production of micro- and nanoparticles. Spray drying variations such as spray freeze-drying into liquid and air nebulization spray drying have been reported as well [1]. The principal disadvantages of the spray drying technique are the formation of aggregates hardly disintegrated by shaking caused for the stress during the drying process and thermal destabilization [15].

Even though these techniques are industrially relevant and relatively easy to scale up [1, 6], problems such as instability, degradation, contamination by the solvent, and a broad particle size distribution have been associated with these processes. Therefore, particle engineering using appropriate systems that preserve the integrity of particles and offer optimal physicochemical properties for drug delivery has been required. Hence, new nanoparticles production methods have emerged for pharmaceutical applications [7, 16]. Lately, a microfluidic method has been used to direct the assembly of liposomes-poly (*N*-isopropylacrylamide) hybrid nanoparticles. As a result, this method has produced narrowly dispersed lipid-hydrogel hybrid nanoparticles for controlled release applications [17]. In addition, it has been found that this technique is able to provide highly monodisperse spherical polymeric microparticles. Nevertheless, the production of shape-controlled nonspherical microparticles is still limited. Modifications of this method such as surface acoustic wave microfluidic atomization (SAW) have been used to generate aerosols with a narrow size distribution within a size range that is optimal for inhalation therapy [18].

In addition to all these processing techniques, alternative polymeric nanoparticles production methods that involve polyelectrolyte complex formation, solvent evaporation single/double emulsion methods, emulsion polymerization, and ionotropic gelation techniques have been reported [1]. For example, in the polyelectrolyte complex formation technique, a polycation and a polyanion are dissolved and mixed to produce nanoparticles. The formation of polyelectrolyte complexes involves the ionic interactions of the ionogenic groups of the oppositely charged polyelectrolytes and generally the reaction takes place in an aqueous solution. However, precipitation and aggregation can occur when both oppositely charged groups approach to unity and low-molecular weight electrolytes are used [19, 20]. In the case of the solvent

evaporation emulsion method, a polymer is dissolved in an organic solvent, followed by emulsification in an aqueous phase. Here, the polymeric solution is dispersed into nanodroplets using high-energy homogenization and a dispersing agent in a nonsolvent medium. Subsequently, the polymer precipitates as nanospheres. During a second step, the organic solvent is evaporated leading to formation of solid nanoparticles [21]. This method has been designed and used particularly for the incorporation of hydrophobic entities into biodegradable micro- and nanoparticles and it is difficult to scale up because of the high-energy requirements [14]. In the emulsion polymerization method, a monomer is added to an aqueous surfactant-containing solution, followed by in situ polymerization of the dispersed phase generating nanoparticles. Because of the requirement of surfactants, monomers, toxic solvents, and initiator, the use of this method has been reduced [1, 14]. Another method that has been widely used to develop hydrogel nanoparticles is ionotropic gelation, in which polysaccharides are dissolved in an aqueous phase and added to solutions containing counterions. The gelation process is caused by the formation of inter- and intramolecular crosslinks within a charged polymer chain, mediated by the presence of oppositely charged ions. Moreover, it has been described that the quality of those hydrogel nanoparticles can be further improved by the polyelectrolyte complexation technique [20, 22, 23].

Even when a diversity of methods have been designed for hydrogel nanoparticle production, the need for systems that efficiently manufacture particles in a simple way with suitable size and polymeric systems that ensure the production of nanoparticle with optimal properties without using toxic solvents is still required.

This study investigates a novel method of generating hydrogel microparticles using biocompatible polymers, non-toxic solvents, and the potential for continuous processing. The synthesis method includes nebulization of polymeric solutions into a gelation fluid followed by separation and drying. For this new particle generation method, we investigated the effects of various processing parameters such as polymer concentration, air pressure, type of crosslinking agent, and type of nebulizer on the size, swelling, and appearance of the resulting polymeric microparticles.

## 2. Materials and Methods

**2.1. Materials.** Chitosan (Cs) (medium MW, % N-deacetylation; about 76.4%, as determined by elemental analysis), monomethoxy-poly(ethylene glycol) (m-PEG, MW 5000 Da), succinic anhydride and 1-hydroxybenzotriazole (HOBr), sodium alginate (low viscosity, 250 cps for 2% w/v aqueous solution at 25°C), and 4-Dimethylaminopyridine (DMAP) were purchased from Aldrich (St. Louis, MO). 1-ethyl-3-(3-dimethylaminopropyl) carbodiimide hydrochloride (EDC·HCl) was purchased from Fluka Chemical Corp (Milwaukee, WI). Phthalic anhydride, triethyl amine, hydrazine monohydrate, dioxane, and dimethylformamide (DMF) were obtained from Sigma-Aldrich (St. Louis, MO, SIAL). Calcium chloride anhydrous was purchased from

EMD Chemicals Inc. (Darmstadt, Germany). Ethanol of analytic grade and  $\text{CCl}_4$  were used as received.

**2.1.1. Preparation of PEG-g-Chitosan Copolymer.** The synthesis of the copolymer of m-PEG grafted onto chitosan (Cs) was carried out by using a modified method previously reported by our group [24]. Briefly, Cs (10 g) was reacted with phthalic anhydride (44.8 g, 5 mol equivalent to pyranose ring) in DMF (200 mL) at 130°C under nitrogen atmosphere for 8 hours to obtain N-phthaloyl chitosan (NPHCs), which was collected after precipitation in cold water, washed with metanol, and dried under vacuum.

The m-PEG macromer was modified to obtain m-PEG-COOH by reacting with succinic anhydride. In brief, an amount of m-PEG (100 g, 20 mmol) was reacted with succinic anhydride (2.4 g, 24 mmol), DMAP (2.44 g, 20 mmol), and triethylamine (2.02 g, 20 mmol) and dissolved in dry dioxane (350 mL). Then, the mixture was stirred at room temperature under nitrogen atmosphere for 48 h and the dioxane was then evaporated under vacuum. The final mixture was taken up in  $\text{CCl}_4$ , filtered, and precipitated in diethyl ether to obtain m-PEG-COOH.

To graft m-PEG-COOH onto NPHCs, m-PEG-COOH (37.9 g) was stirred with NPHCs (5.0 g, 0.4 mol equivalent to m-PEG-COOH) in DMF containing HOEt (3.4 g, 3 mol equivalent to m-PEG-COOH) until obtaining a clear solution. EDC·HCl (4.25 g, 3 mol equivalent to m-PEG-COOH) was added and stirred at room temperature overnight. The mixture was dialyzed in distilled water and washed thoroughly with ethanol to remove impurities.

To synthesize the PEG-g-Cs copolymer, a deprotection of the masked  $\text{NH}_2$  groups of PEG-g-NPHCs was carried out by using hydrazine monohydrate. Briefly, PEG-g-NPHCs (4.0 g) was heated to 100°C and stirred in 15 mL of DMF under nitrogen atmosphere. Then, hydrazine monohydrate (20 mL) was added and the mixture was stirred for 2 h. The final mixture was then dialyzed against a mixture of water and ethanol (1:1) and dried at 40°C under vacuum.

**N-Phthaloyl Chitosan (NPHCs).** EA ( $\text{C}_8\text{H}_{13}\text{NO}_5$ )<sub>0.2363</sub> ( $\text{C}_6\text{H}_{11}\text{NO}_4$ )<sub>0.016</sub> ( $\text{C}_{14}\text{H}_{13}\text{NO}_6$ )<sub>0.747</sub>, Anal. Calculated (%): C, 55.74; H, 4.84; and N, 5.23, found (%): C, 60.31; H, 4.83; and N, 4.92. FT-IR ( $\nu_{\text{max}}$ ,  $\text{cm}^{-1}$ ), 3281 (OH stretching and NH bending), 2961 (C–H stretching), 1775 and 1698 (C=O anhydride), 1395 (C=C, phthaloyl), 1058 (C–O, pyranose), and 732 (aromatic ring).

**m-PEG-COOH (yield 98%).** EA ( $\text{C}_{23}\text{H}_{46}\text{O}_{117}$ ), Anal. Calculated (%): C, 54.35 and H, 9.02, found (%): C, 56.8 and H, 9.19. FT-IR ( $\nu_{\text{max}}$ ,  $\text{cm}^{-1}$ ) 3496 (OH stretching), 2882 (C–H stretching), 1733 (C=O of carboxylic group), and 1102 (C–O–C stretching).

**PEG-g-NPHCs (5.47 g).** EA, found (%): C, 56.16; H, 4.96; and N, 5.15. FT-IR ( $\nu_{\text{max}}$ ,  $\text{cm}^{-1}$ ) 3423 (OH stretching and NH bending), 2879 (C–H stretching), 1736 (C=O ester and anhydride), 1703 (C=O anhydride), 1096 (C–O–C stretching), and 723 (aromatic ring of phthaloyl).

**PEG-g-Cs.** EA, found (%): C, 40.46; H, 4.71; and N, 14.44. FT-IR ( $\nu_{\text{max}}$ ,  $\text{cm}^{-1}$ ) 3312 (OH stretching, NH bending, and intermolecular H-bonding), 2879 (C–H stretching), 1708 (C=O ester), and 1096 (C–O–C stretching).

## 2.2. Methods

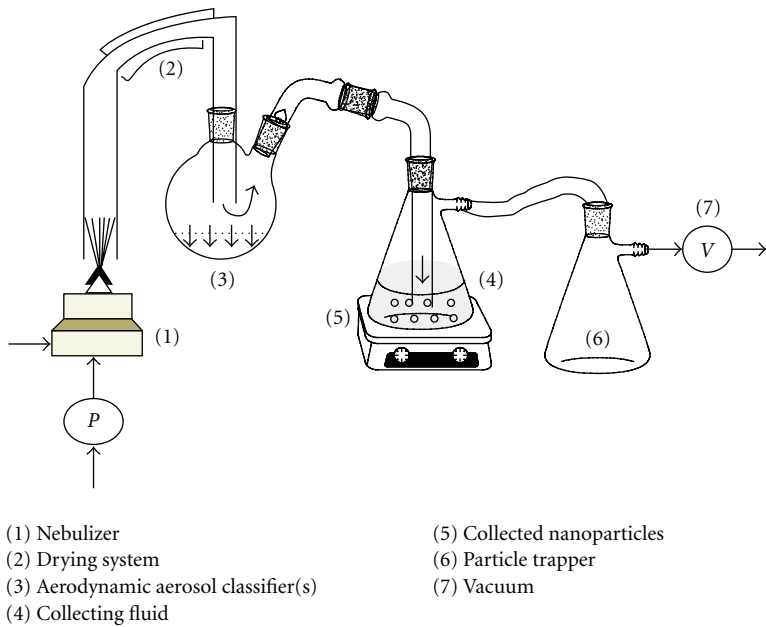
**2.2.1. Spray Gelation-Based System and Preparation of the Hydrogel Particles.** The hydrogel particles were developed via air-jet nebulization of small sprayed droplets of alginate solutions followed by either ionotropic gelation in aqueous  $\text{Ca}^{2+}$  solution or both ionotropic and polyelectrolyte complexation in (1:1) aqueous solution of PEG-g-Cs/ $\text{CaCl}_2$  as crosslinkers. Briefly, an (0.1% w/v) aqueous solution of the synthesized copolymer, PEG-g-Cs was prepared using a few mLs of 0.06 M acetic acid and then made up to the predetermined volume with distilled water. Also, aqueous solutions of  $\text{CaCl}_2$  (0.2 M) and sodium alginate (0.5 and 1% w/v) were prepared. Alginate solutions of different concentrations were added to different air-jet nebulizers (Pari LC Plus and Aerotech II) and aerosolized by using compressed air delivered at controlled pressures of 20 and 40 psi (Table 1). The generated sprayed droplets were then collected into the crosslinking solutions containing either  $\text{CaCl}_2$  (0.2 M) or a (1:1) mixture of PEG-g-Cs/ $\text{CaCl}_2$  under continuous mild stirring throughout a vacuum system leading to gelation of the aerosol droplets. The obtained swollen hydrogel particles were transferred to scintillation vials and freeze-dried. The resulting hydrogel powder was then washed with water to remove any residual crosslinker and then refreeze-dried. The yield (%) of the resulting dry hydrogel particles powders was calculated and then the powders were stored at room temperature in a desiccator until further investigation.

A schematic illustration of the complete spray gelation-based system developed in this study is shown in Scheme 1. The system consists of a regulated compressed air source directly connected to a nebulizer that delivers the polymeric solutions as sprayed droplets to a feed zone comprising tubing carrying droplets. This tubing carrying droplets was assembled to an aerodynamic aerosol classifier connected to a secondary vacuum system responsible of transporting the sprayed droplets to the crosslinker solutions (collecting fluids). An alternate empty glass collector was directly assembled to the primary vacuum system to recover the hydrogel microparticles dragged from the secondary vacuum system.

**2.2.2. Characterization of PEG-g-Cs Graft Copolymer.** The elemental analysis for all products involved in the synthesis of PEG-g-Cs graft copolymer was carried out by using a Costech ECS4010 Elemental Analyzer coupled to a Thermo-Finnigan Delta Plus Isotope Ratio Mass Spectrometer. FT-IR spectra were recorded on a Nicolet 6700 FT-IR spectrometer. Differential Scanning Calorimetry (DSC) was used to analyze all synthesized polymers using a DSC 2920 (Modulated DSC, TA Instruments, Woodland, CA). 10 to 12 mg were weighted into aluminum pans and sealed. All measurements were performed in a range from –40 to 400°C at a heating rate of 10°C/min.

TABLE 1: Parameters and compositions of the hydrogel particles developed by the new spray gelation-based method.

Nebulizer	Sample code	Air pressure (psi)	Crosslinker	% Alginate (w/v)	GSD
Pari LC Plus	PN1	20	CaCl <sub>2</sub>	0.5	1.2
	PN2	20	PEG-g-Cs/CaCl <sub>2</sub>	0.5	1.1
	PN3	40	CaCl <sub>2</sub>	0.5	1.3
	PN4	40	PEG-g-Cs/CaCl <sub>2</sub>	0.5	1.1
	PN5	20	CaCl <sub>2</sub>	1	1.1
	PN6	20	PEG-g-Cs/CaCl <sub>2</sub>	1	1.3
	PN7	40	CaCl <sub>2</sub>	1	1.3
	PN8	40	PEG-g-Cs/CaCl <sub>2</sub>	1	1.2
Aerotech II	AN1	20	CaCl <sub>2</sub>	0.5	1.3
	AN2	20	PEG-g-Cs/CaCl <sub>2</sub>	0.5	1.2
	AN3	40	CaCl <sub>2</sub>	0.5	1.1
	AN4	40	PEG-g-Cs/CaCl <sub>2</sub>	0.5	1.1
	AN5	20	CaCl <sub>2</sub>	1	1.1
	AN6	20	PEG-g-Cs/CaCl <sub>2</sub>	1	1.4
	AN7	40	CaCl <sub>2</sub>	1	1.2
	AN8	40	PEG-g-Cs/CaCl <sub>2</sub>	1	2.2



SCHEME 1: General scheme of the composition of the new spray gelation-based system used for the production of hydrogel particles.

### 2.2.3. Characterization of Hydrogel Particles

**Particle Size Measurements.** The average size of the prepared hydrogel particles suspended in ethanol was determined by dynamic light scattering, DLS (Malvern nanosizer, Malvern Instruments Ltd., Worcestershire, UK). The particle size was also estimated using microscopy techniques including light microscopy (Leica DMI6000B scope) with Leica application suite advanced fluorescence 2.2.0 build 4765 software. Particle sizes for each hydrogel formulation were recorded to be statistically analyzed to obtain the mean particle size, the standard deviation, and the geometric standard deviation (GSD).

**Dynamic Swelling Study.** The swelling behavior of the hydrogel particles in water was studied by determining the increase in the mean particle diameter after 2, 5, 10, 60, and 120 minutes. The measurements of the swollen hydrogel particles were recorded to estimate the swollen mean size.

**Scanning Electron Microscopy (SEM).** Scanning electron microscopy analysis was carried out to study the surface morphology of the developed particles by using a Zeiss Supra 40 VP scanning electron microscope. The dried particles were mounted on aluminum studs and coated with a 50/50 mixture of Au/Pd and scanned using an accelerating voltage of 10 kV.

**2.2.4. Optimization of the Hydrogel Particles by a  $2^k$  Factorial Design.** A  $2^k$  factorial design was used to determine the effect of formulation's variables such as type of nebulizer, type of crosslinker, polymeric concentration and the compressed air pressure on the hydrogel nanoparticle size, and swelling for further optimization and investigations. In addition, statistical significance was determined using ANOVA ( $P < .05$ ) for each response variable (size and swelling). Statgraphics Plus version 5.0 software was used.

### 3. Results and Discussion

In the present study, a novel spray gelation-based method was developed for the production of hydrogel particles by using sprayed microdroplets from nebulizers. In addition, the effects of different processing parameters on the characteristics of the developed hydrogel particles such as size and morphology were assessed. The setup of this novel method is very simple and easy and did not require large amounts of material. It just involved the preparation of the polymeric solution to be sprayed and the crosslinking agent.

**3.1. Synthesis of PEG-g-Cs Copolymer.** The PEG-g-Cs copolymer synthesized through a modified method reported previously by our group was successfully obtained [12]. A 98% yield of m-PEG-COOH was obtained and characterized by FT-IR and elemental analysis (EA). In the same way, the synthesis of NPHCs was confirmed by FT-IR through the appearance of the bands at 1395 and  $732\text{ cm}^{-1}$ , which correspond to the aromatic C=C and the aromatic ring of the phthaloyl group, respectively. The grafting of m-PEG-COOH onto NPHCs was carried out in DMF (grafting %; 9.34). Afterwards, the PEG-g-Cs copolymer was obtained by deprotection of NH<sub>2</sub> groups of PEG-g-NPHCs copolymer using N<sub>2</sub>H<sub>4</sub>·H<sub>2</sub>O. The FT-IR and EA were also used to confirm the synthesis of the PEG-g-Cs copolymer. In the DSC of Cs, (data were reported elsewhere) [12], endothermic and exothermic peaks were shown at 90°C and 312°C, respectively. The former peak is attributed to the loss of moisture and the exothermic peak observed is mainly due to the decomposition of Cs. In the case of PEG-g-Cs, an endothermic peak at 55°C corresponding to the melting of the grafted PEG was observed. In addition, an endothermic peak was shown at 119°C as a consequence of the loss of water. Moreover, two exothermic events appeared at 261 and 310°C and were related to the crystallization and decomposition of the graft copolymer, respectively [12].

**3.2. Preparation of Hydrogel Particles.** Different concentrations of alginate solutions were used to prepare hydrogel particles through a spray gelation process for drug delivery applications. As shown in Table 1, several hydrogel particle formulations were obtained based on the combination of parameter such as nebulizers, crosslinkers, and applied air pressure. In addition, the geometric standard deviation (GSD) of the different formulations was listed.

Since nebulizers have been therapeutically used to convert liquids into aerosols and it has been proven that they

can produce fine droplets ( $\sim 1\text{ }\mu\text{m}$ ) [1], we proposed that nebulizers may be appropriate for delivering the alginate solutions, as example for other polymer solutions, into small droplets under the principles of jet nebulization as a new alternative method for production of hydrogel particles. Alginate solutions of different concentrations were added to the nebulizer and the driving force for the atomization of the alginate droplets was generated by the high-velocity air that passes through a small nozzle within the device and at the same time draws fluid to be nebulized via the venturi effect [25]. Then, after the sprayed anionic polyelectrolyte alginate solutions were passed directly into an aqueous solution containing divalent cations such as Ca<sup>2+</sup> or polycation such as PEG-g-Cs copolymer. Following this rapid reaction, insoluble network structures were formed and gelation was induced because of the diffusion of cations into the alginate droplets or by the formation of polyelectrolyte complexes, forming three-dimensional lattice of ionically crosslinked polymer resulting in the formation of hydrogel particles, which were later dried by freeze-drying. After the final powder was collected and weighed, the spray gelation yield was calculated resulting in a range between 30% and 90%.

Aerotech II and Pari LC Plus nebulizers were chosen in this study because of the several literature reports [26–28], in addition to our prestudy screening experiments using different types of nebulizers. Also, Aerotech II and Pari LC Plus were found to have greater aerosol output efficiencies, produce droplets with small sizes ( $<5\text{ }\mu\text{m}$ ), and show higher efficiency in the aerosolization of viscous formulations. Also, it has been reported [25] that the main determinants of a droplet size produced by a nebulizer include the characteristics of the solutions such as viscosity and the velocity of the gas. Thus, the influence of polymer concentration, air pressure, and crosslinker type on droplet sizes was studied in these investigations.

**3.3. Particle Size Analysis.** Figure 1 shows the influence of the formulation's parameters on the mean size of the hydrogel particles. The mean size of the particles developed using the Pari LC Plus and Aerotech II nebulizers was found to be 842 and 886 nm, respectively, with a standard deviation of 7%–12%. The particle size of the obtained hydrogels was also confirmed by DLS technique where, according to the data, Pari LC Plus and Aerotech II showed very similar sizes (around 858 nm and 889 nm, resp.).

To verify the existence of significant differences between both sets of particle size data upon using different nebulizers (Pari LC Plus or Aerotech II), statistical analysis was carried out. The obtained results showed minor statistical differences ( $P = .0445$ ) (Table 2). These minor statistical differences can be attributed to practical differences. As shown in Figure 1(a), Pari LC Plus nebulizer generated hydrogel particles with hardly comparable sizes (PN1 = PN5, PN4 > PN8, PN6 > PN2) of particles with different alginate concentrations, even when it seemed that 0.5% produced smaller particle size. The data also showed that the air pressure is a determinant factor on the droplet size because upon applying higher pressure (40 psi), all formulations

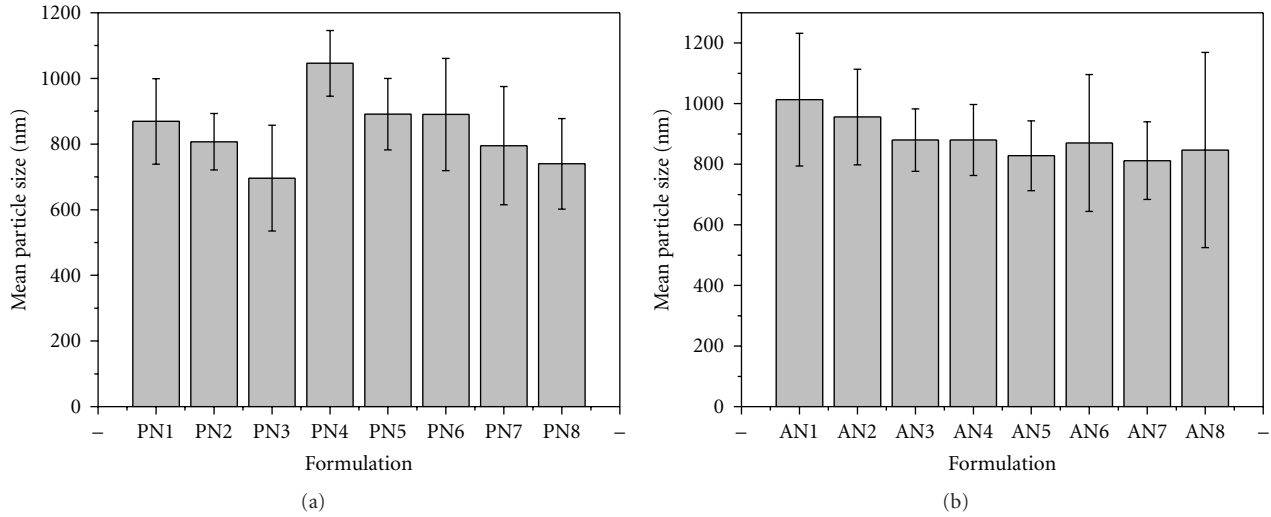


FIGURE 1: Mean particle size (diameter,  $d$ , nm) of the dried hydrogel particles produced by spray gelation-based method using the (a) Pari LC Plus and (b) Aerotech II nebulizers.

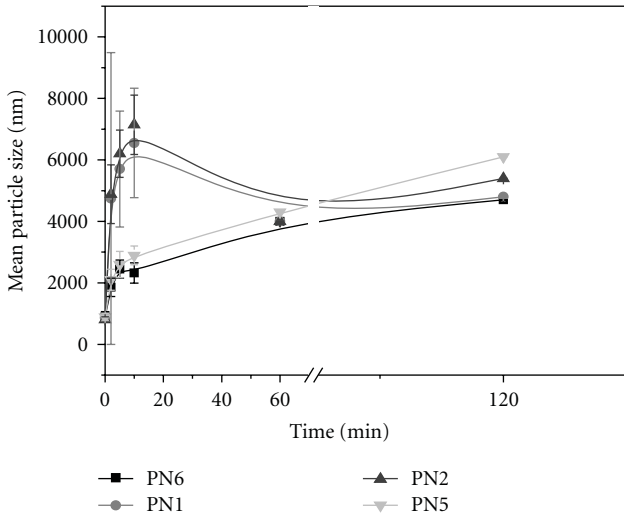


FIGURE 2: Swelling behavior of hydrogel particles based on the concentration of alginate solutions (PN1 and PN2, 0.5% and PN5 and PN6, 1%) after 2, 5, 10, 60, and 120 minutes.

(PN3, PN7, and PN8) showed the smallest particles size, except for PN4. The influence of the type of crosslinker on the particle size was not clearly seen.

On the other hand, in comparison with Pari LC Plus, Aerotech II formulations showed very slightly larger particle sizes and as mentioned before, we attributed this increase to practical differences (Figure 1(b)). Nevertheless, they presented more uniform sizes. This effect may be related to the presence of a baffle that covers the aerosol stream region preventing the formation of larger particles due to the centered pressure applied during atomization into a constant direction. In the case of Aerotech II formulations, relatively smaller hydrogel particles were produced when 1% alginate solutions were used, particularly this effect could be seen

in AN7 and AN5 formulations. This was probably because a higher concentration of polymer shows a larger capacity of being crosslinked leading to the formation of smaller size. In addition, it appears that the type of the crosslinkers used in this study has no significant effect onto the size of the developed particles (see Table 2).

**3.4. Swelling Equilibrium Study.** The swelling profiles of the hydrogel particles in water are shown in Figure 2. The effect of alginate concentrations and type of crosslinker on the swelling behavior of the formulations developed using Pari LC Plus (PN1, PN2, PN5, and PN6) was investigated. The swelling extents were estimated by determination of the increase in the mean diameter (nm) of hydrogel particles after 2, 5, 10, 60, and 120 minutes by microscopy. As seen in Figure 2, the formulations containing 0.5% alginate (PN1 and PN2) showed a faster initial swelling after 2 min in comparison with the formulations of 1% alginate, increasing their size more than four times. For example, the size of PN1 and PN2 increased from 869 and 807 nm when dried to 4,647 and 4,884 nm after 2 min, respectively. A continuous increase in the mean diameter was observed after 10 min, where the hydrogel particles reached values of 6,551 and 7,144 nm, respectively. From the figure, it can be noted that increasing the alginate concentration to 1% has reduced the swelling values of the hydrogel particles. These data are consistent with the crosslinking extent, where as the alginate concentration increases, the interaction of alginate with the divalent cations is enhanced, leading to the formation of a smaller mesh size in the meshwork that limits the access of water. In this way, PN5 and PN6 formulations showed smaller sizes when swollen. In the effect of type of crosslinker onto swelling, it was observed that, with keeping the alginate concentration constant at 0.5%, both  $\text{CaCl}_2$  and the  $\text{PEG-g-Cs/CaCl}_2$  mixture showed a similar effect on the swelling of the hydrogel particles. The same phenomenon was observed in the 1% alginate formulations. These data were confirmed

TABLE 2: Summary of the analysis of variance for mean particle size.

Factor	Sum of squares	DF	Mean square	F-ratio	*P-value
Nebulizer	23232.0	1	23232.0	4.34	.0445
Crosslinker	11907.0	1	11907.0	2.23	.1446
Alginate	42126.8	1	42126.8	7.88	.0081
Air Pressure	34347.0	1	34347.0	6.42	.0159

\* P < .05, DF: Degree of Freedom.

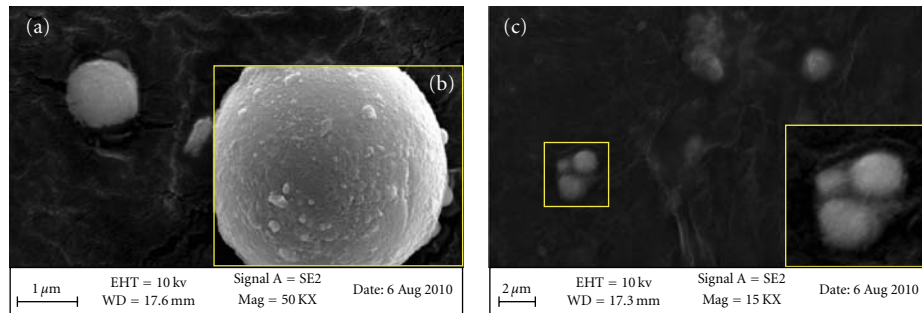


FIGURE 3: Scanning electron micrographs of alginate particles produced using the Aerotech II nebulizer using spray gelation: (a, b) AN7 and (c) AN8.

by the *P*-value obtained by the analysis of variance, which showed a nonsignificant difference between both crosslinkers (Table 2). After 60 min, a continuous increment in the swelling behavior of formulations containing 1% alginate was also seen. However, from the figure, it can be noted also that some of the hydrogel formulations (with 0.5% alginate such as PN1 and PN2) showed a swelling decrease at equilibrium. Generally, the fast initial swelling of hydrogel formulations is attributed to their hydrophilic nature (osmotic driving forces). This is followed by occurrence of a resistance due to the cohesive forces exerted by the crosslinked polymer chains. These cohesive forces tend to resist further hydrogel expansion and encourage some of swelling fluid to be expelled which explains the swelling decrease stage [29]. The extent of these two opposing forces (osmotic and cohesive) depends mainly on the crosslinking magnitude of hydrogels, and generally, the equilibrium is reached when a balance is achieved between these two forces.

**3.5. Scanning Electronic Microscopy.** It is well known that the final particle morphology (hollow and solid particles) and the size of the sprayed or aerosol particles are dependent on the solution characteristics, precursor concentration, viscosity, droplet size, evaporation rate, and operating parameters such aerosol generator, flow rate, and drying technique [30, 31]. Hence, in this study we investigated the effect of different concentrations, two aerosol generators (nebulizers), and different air pressures on the appearance of the hydrogel particles. Figure 3 shows some scanning electron micrographs of the morphology of hydrogel particles generated by the spray gelation method. The developed hydrogel particles presented, in general, spherical shapes with highly rough surfaces, especially in Pari LC Plus formulations, where 1% alginate solutions and 40 psi air pressure were applied

(Figure 3(b)). Furthermore, Aerotech II formulations also presented spherical shapes under the same conditions (Figure 3(c)). It seems that the concentration of both polymer and crosslinker used played an important role in the formation of spherical, solid, and well-crosslinked particles; however, the type of nebulizer did not significantly change the morphology of the particles. This may be attributed to the fact that both nebulizers operated under the same mechanism. Further investigation of the drying mechanism along with some other parameters has to be carried out to determine their effects on the hydrogel morphology.

**3.6. Analysis of the Hydrogel Particles Synthesis by a 2<sup>k</sup> Factorial Design.** In this study, a discontinuous 2<sup>k</sup> factorial design was carried out to determine the effects of nebulizer, crosslinker, air pressure, and alginate concentration and their interaction on the obtained hydrogel formulations. Considering that the combination of those factors would modify the properties of the particles, variations of each factor in two levels were analyzed. The two levels of each factor were coded with a low and high level to be analyzed by response surface methodology and Pareto charts. In this design, the particle size and equilibrium swelling values were used as response variables. Since type of nebulizer and crosslinker are not numeric values, -1 and 1 levels were assigned for each nebulizer and crosslinker.

The analysis of variance for particle size obtained by Statgraphics 5.0 shows the most influential factors in the size and swelling behavior of the hydrogel particles at the 95% confidence level. Then, all those factors and/or interactions with a *P* < .05 value were considered the most relevant factor for either particle size or swelling. Thus, the obtained results showed that four effects are influencing the particle size. Those effects and their interactions can be clearly

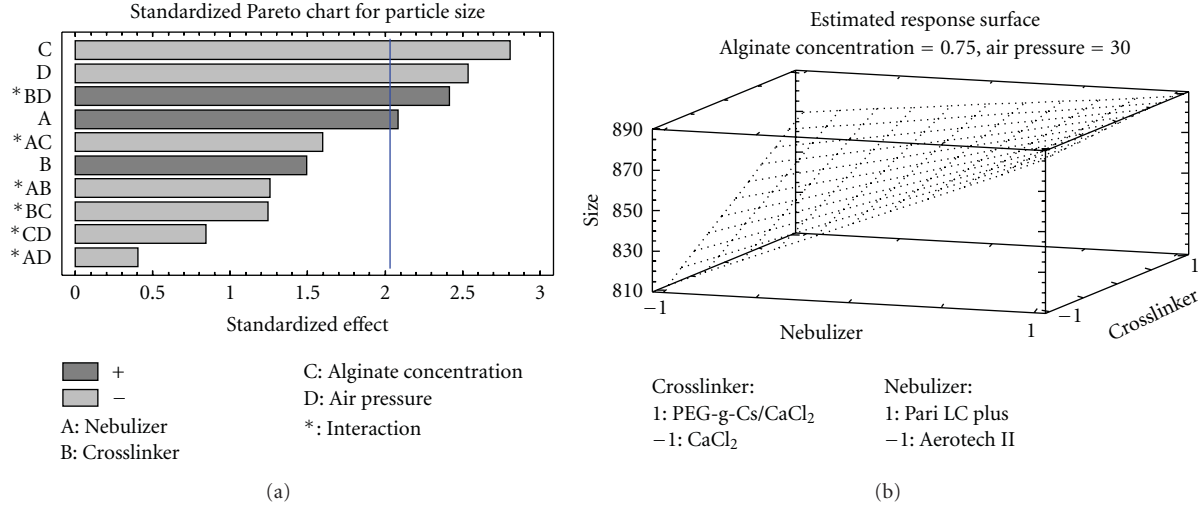


FIGURE 4: Statistical estimation of the effect of formulation's parameters and their interactions on the particle size of hydrogel particles represented by (a) Pareto chart and (b) response surface methodology.

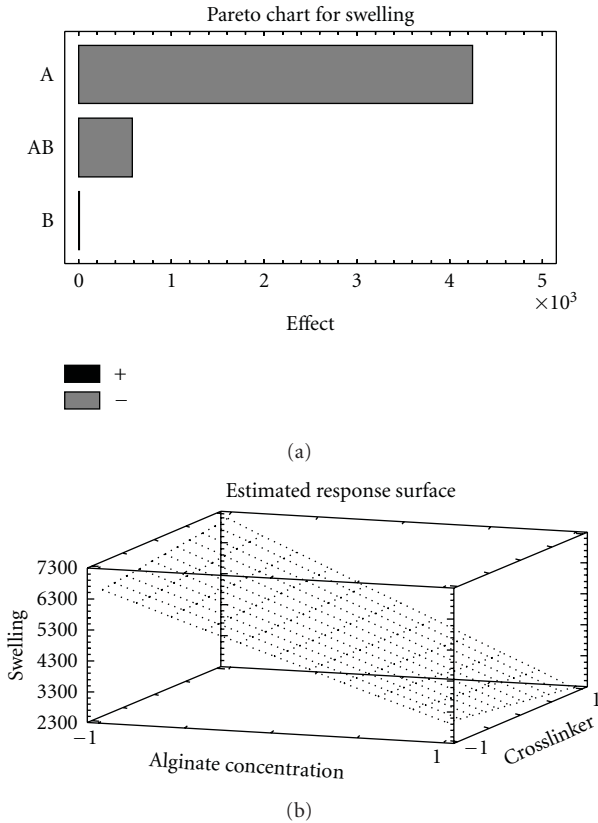


FIGURE 5: (a) Pareto chart and (b) response surface methodology graph of the effect of alginate concentration and crosslinker on the swelling behavior of hydrogel particles.

seen in the standardized Pareto chart (Figure 4(a)), where it is showed that alginate concentration, air pressure, the interaction between crosslinker and air pressure, and the type of nebulizer are the main factors that modify the size

of the hydrogel particles. The order in which they appear corresponds to their importance in affecting the particle size. From the figure, it seems that the alginate concentration is the principal determinant of the size of particles, followed by the air pressure. Therefore, modification of any of these two factors would have a more relevant effect on the particle size than the other factors. We also used surface response methodology to illustrate the way in which particle size would respond to variations in the parameter used during the production of particles (Figure 4(b)). The results showed that when the alginate concentration and air pressure are maintained in their intermediate values, by using Pari LC Plus nebulizer, smaller particle sizes can be obtained. The effect of the type of crosslinker is considered not significantly different. This effect can be clearly observed by the pronounced slope that gives rises to the minimum peak on the presented surface. Therefore, the data shown here are consistent with the particle size data found experimentally, where Pari LC produced relatively smaller particle sizes than Aerotech II.

In the case of the swelling behavior, the crosslinker and alginate concentration were the factors modified in this study for Pari LC Plus formulations and the results in Pareto chart (Figure 5(a)) showed that alginate concentration is a fundamental factor in the processing of the particles and any modification in its value would lead to an increase or reduction in the swelling values. According to the surface response methodology graph, particles with 0.5% alginate would reach a larger size when swollen than the formulations with 1% alginate (Figure 5(b)). These data are very consistent with our experimental results, as seen in Figure 2. Also, the interaction between both factors plays an important function, showing dependence on the alginate concentration used. However, the type of the crosslinker by itself does not have an effect on the swelling behavior of particles (Figure 5).

## 4. Conclusion

It has been demonstrated that the spray gelation-based system described in this study can be used as an alternative method for the preparation of hydrogel particles with well-defined shapes and sizes around 840 nm. Moreover, the obtained results indicated that the size of the hydrogel particles can be optimized by changing the polymer concentration and the applied air pressure. In addition, the developed method offers many advantages over other methods such relative simplicity, low cost, and ease of collecting fluid and it does not involve the use of toxic solvents. All these advantages make this new technique valuable for the preparation of hydrogel particles for various applications particularly for drug delivery purposes. However, as a novel method, additional effort has to be done for the investigation and optimization of the particle size and aerosolization.

## References

- [1] M. M. Bailey and C. J. Berkland, "Nanoparticle formulations in pulmonary drug delivery," *Medicinal Research Reviews*, vol. 29, no. 1, pp. 196–212, 2009.
- [2] W. Yang, J. I. Peters, and R. O. Williams, "Inhaled nanoparticles—a current review," *International Journal of Pharmaceutics*, vol. 356, no. 1-2, pp. 239–247, 2008.
- [3] A. B. Watts, J. T. McConville, and R. O. Williams, "Current therapies and technological advances in aqueous aerosol drug delivery," *Drug Development and Industrial Pharmacy*, vol. 34, no. 9, pp. 913–922, 2008.
- [4] G. Della Porta, C. de Vittori, and E. Reverchon, "Supercritical assisted atomization: a novel technology for microparticles preparation of an asthma-controlling drug," *AAPS PharmSciTech*, vol. 6, no. 3, pp. E421–E428, 2005.
- [5] P. Chattopadhyay, R. Huff, and B. Y. Shekunov, "Drug encapsulation using supercritical fluid extraction of emulsions," *Journal of Pharmaceutical Sciences*, vol. 95, no. 3, pp. 667–679, 2006.
- [6] B. Y. Shekunov, P. Chattopadhyay, J. Seitzinger, and R. Huff, "Nanoparticles of poorly water-soluble drugs prepared by supercritical fluid extraction of emulsions," *Pharmaceutical Research*, vol. 23, no. 1, pp. 196–204, 2006.
- [7] J. Xie, L. K. Lim, Y. Phua, J. Hua, and C. H. Wang, "Electrohydrodynamic atomization for biodegradable polymeric particle production," *Journal of Colloid and Interface Science*, vol. 302, no. 1, pp. 103–112, 2006.
- [8] M. Trotta, R. Cavalli, C. Trotta, R. Bussano, and L. Costa, "Electrospray technique for solid lipid-based particle production," *Drug Development and Industrial Pharmacy*, vol. 36, no. 4, pp. 431–438, 2010.
- [9] F. Bagheri-Tar, M. Sahimi, and T. T. Tsotsis, "Preparation of polyetherimide nanoparticles by an electrospray technique," *Industrial and Engineering Chemistry Research*, vol. 46, no. 10, pp. 3348–3357, 2007.
- [10] K. P. Krause and R. H. Müller, "Production and characterisation of highly concentrated nanosuspensions by high pressure homogenisation," *International Journal of Pharmaceutics*, vol. 214, no. 1-2, pp. 21–24, 2001.
- [11] R. Ambrus, A. Pomázi, J. Kristl, P. Kocbek, and P. Szabó-Révész, "Effect of high-pressure homogenization on the formulation of micro- and nanocrystals containing poorl watersoluble meloxicam," *Scientia Pharmaceutica*, p. 571, 2010.
- [12] N. A. Al Haj, R. Abdullah, S. Ibrahim, and A. Bustamam, "Tamoxifen drug loading solid lipid nanoparticles prepared by hot high pressure homogenization techniques," *American Journal of Pharmacology and Toxicology*, vol. 3, no. 3, pp. 219–224, 2008.
- [13] B. S. Chu, S. Ichikawa, S. Kanafusa, and M. Nakajima, "Preparation and characterization of β-carotene nanodispersions prepared by solvent displacement technique," *Journal of Agricultural and Food Chemistry*, vol. 55, no. 16, pp. 6754–6760, 2007.
- [14] C. Pinto Reis, R. J. Neufeld, A. J. Ribeiro, and F. Veiga, "Nanoencapsulation I. Methods for preparation of drug-loaded polymeric nanoparticles," *Nanomedicine: Nanotechnology, Biology, and Medicine*, vol. 2, no. 1, pp. 8–21, 2006.
- [15] M. V. Chaubal and C. Popescu, "Conversion of nanosuspensions into dry powders by spray drying: a case study," *Pharmaceutical Research*, vol. 25, no. 10, pp. 2302–2308, 2008.
- [16] K. Liu, H. J. Ding, J. Liu, Y. Chen, and X. Z. Zhao, "Shape-controlled production of biodegradable calcium alginate gel microparticles using a novel microfluidic device," *Langmuir*, vol. 22, no. 22, pp. 9453–9457, 2006.
- [17] J. S. Hong, S. M. Stavis, S. H. Depaoli Lacerda, L. E. Locascio, S. R. Raghavan, and M. Gaitan, "Microfluidic directed self-assembly of liposome-hydrogel hybrid nanoparticles," *Langmuir*, vol. 26, no. 13, pp. 11581–11588, 2010.
- [18] A. Qi, J. R. Friend, L. Y. Yeo, D. A. V. Morton, M. P. McIntosh, and L. Spiccia, "Miniature inhalation therapy platform using surface acoustic wave microfluidic atomization," *Lab on a Chip*, vol. 9, no. 15, pp. 2184–2193, 2009.
- [19] R. Mincheva, F. Bougard, D. Paneva et al., "Polyelectrolyte complex nanoparticles from n-carboxyethylchitosan and polycationic double hydrophilic diblock copolymers," *Journal of Polymer Science A*, vol. 47, no. 8, pp. 2105–2117, 2009.
- [20] J. S. Patil, M. V. Kamalapur, S. C. Marapur, and D. V. Kadam, "Ionotropic gelation and polyelectrolyte complexation: the novel techniques to design hydrogel particulate sustained, modulated drug delivery system: a review," *Digest Journal of Nanomaterials and Biostructures*, vol. 5, no. 1, pp. 241–248, 2010.
- [21] R. C. Mundargi, V. R. Babu, V. Rangaswamy, P. Patel, and T. M. Aminabhavi, "Nano/micro technologies for delivering macromolecular therapeutics using poly(d,L-lactide-co-glycolide) and its derivatives," *Journal of Controlled Release*, vol. 125, no. 3, pp. 193–209, 2008.
- [22] ř. Racoviă, S. Vasiliu, M. Popa, and C. Luca, "Polysaccharides based on micro- and nanoparticles obtained by ionic gelation and their applications as drug delivery systems," *Revue Roumaine de Chimie*, vol. 54, no. 9, pp. 709–718, 2009.
- [23] I. M. El-Sherbiny, "Enhanced pH-responsive carrier system based on alginate and chemically modified carboxymethyl chitosan for oral delivery of protein drugs: preparation and in-vitro assessment," *Carbohydrate Polymers*, vol. 80, no. 4, pp. 1125–1136, 2010.
- [24] I. M. El-Sherbiny, S. McGill, and H. D. C. Smyth, "Swellable microparticles as carriers for sustained pulmonary drug delivery," *Journal of Pharmaceutical Sciences*, vol. 99, no. 5, pp. 2343–2356, 2010.
- [25] D. R. Hess, "Nebulizers: principles and performance," *Respiratory Care*, vol. 45, no. 6, pp. 609–622, 2000.

- [26] M. McPeck, R. Tandon, K. Hughes, and G. C. Smaldone, "Aerosol delivery during continuous nebulization," *Chest*, vol. 111, no. 5, pp. 1200–1205, 1997.
- [27] P. W. Barry and C. O'Callaghan, "An in vitro analysis of the output of salbutamol from different nebulizers," *European Respiratory Journal*, vol. 13, no. 5, pp. 1164–1169, 1999.
- [28] A. Bauer, P. McGlynn, L. L. Bovet, P. L. Mims, L. A. Curry, and J. P. Hanrahan, "Output and aerosol properties of 5 nebulizer/compressor systems with arformoterol inhalation solution," *Respiratory Care*, vol. 54, no. 10, pp. 1342–1347, 2009.
- [29] J. M. Guenet, *Thermoreversible 546 Gelation of Polymers and Biopolymers*, Academic Press, New York, NY, USA, 1992.
- [30] X. Jiang, T. L. Ward, F. V. Swol, and C. J. Brinker, "Numerical simulation of ethanol-water-nacl droplet evaporation," *Industrial and Engineering Chemistry Research*, vol. 49, no. 12, pp. 5631–5643, 2010.
- [31] J. C. Lin and J. W. Gentry, "Spray drying drop morphology: experimental study," *Aerosol Science and Technology*, vol. 37, no. 1, pp. 15–32, 2003.

## Research Article

# Smart Magnetically Responsive Hydrogel Nanoparticles Prepared by a Novel Aerosol-Assisted Method for Biomedical and Drug Delivery Applications

Ibrahim M. El-Sherbiny<sup>1,2</sup> and Hugh D. C. Smyth<sup>2</sup>

<sup>1</sup> Polymer Laboratory, Chemistry Department, Faculty of Science, Mansoura University, 35516 Mansoura, Egypt

<sup>2</sup> Division of Pharmaceutics, College of Pharmacy, The University of Texas at Austin, Austin, TX 78712, USA

Correspondence should be addressed to Ibrahim M. El-Sherbiny, imelsherbiny@gmail.com

Received 27 August 2010; Accepted 14 December 2010

Academic Editor: Xingmao Jiang

Copyright © 2011 I. M. El-Sherbiny and H. D. C. Smyth. This is an open access article distributed under the Creative Commons Attribution License, which permits unrestricted use, distribution, and reproduction in any medium, provided the original work is properly cited.

We have developed a novel spray gelation-based method to synthesize a new series of magnetically responsive hydrogel nanoparticles for biomedical and drug delivery applications. The method is based on the production of hydrogel nanoparticles from sprayed polymeric microdroplets obtained by an air-jet nebulization process that is immediately followed by gelation in a crosslinking fluid. Oligoguluronate (G-blocks) was prepared through the partial acid hydrolysis of sodium alginate. PEG-grafted chitosan was also synthesized and characterized (FTIR, EA, and DSC). Then, magnetically responsive hydrogel nanoparticles based on alginate and alginate/G-blocks were synthesized via aerosolization followed by either ionotropic gelation or both ionotropic and polyelectrolyte complexation using  $\text{CaCl}_2$  or PEG-g-chitosan/ $\text{CaCl}_2$  as crosslinking agents, respectively. Particle size and dynamic swelling were determined using dynamic light scattering (DLS) and microscopy. Surface morphology of the nanoparticles was examined using SEM. The distribution of magnetic cores within the hydrogels nanoparticles was also examined using TEM. In addition, the iron and calcium contents of the particles were estimated using EDS. Spherical magnetic hydrogel nanoparticles with average particle size of  $811 \pm 162$  to  $941 \pm 2$  nm were obtained. This study showed that the developed method is promising for the manufacture of hydrogel nanoparticles, and it represents a relatively simple and potential low-cost system.

## 1. Introduction

Over the last two decades, stimuli-responsive “smart” hydrogels, which can respond reversibly to external stimuli, such as pH, temperature, and electric field, have attracted a great deal of interest due to their potential applications in various fields especially in controlled drug delivery [1]. In the recent years, a significant body of research has focused on the development of biocompatible magnetically responsive nanoparticles for various drug delivery and biomedical applications such as magnetic drug targeting, enzyme immobilization, hyperthermia anticancer treatment, and the magnetic resonance imaging for clinical diagnosis [2–9]. The efficiency of magnetic nanoparticles in most of these applications depends particularly on the particle size distribution and the morphology of the polymer/magnetic nanoparticles [10, 11].

The magnetically responsive hydrogel nanoparticles with high-saturation magnetization and high susceptibility showed a good ability to trigger drug release upon applying external magnetic stimuli [12]. The major advantage of this drug delivery technology is attributed to the magnetic characteristics of the carrier system, which can be controlled remotely, and the biocompatibility of both the encapsulated iron oxide nanoparticles (e.g., magnetite ( $\text{Fe}_3\text{O}_4$ ) and maghemite ( $\gamma\text{-Fe}_2\text{O}_3$ )) and the polymeric hydrogel matrices. Superparamagnetic iron oxide nanoparticles (SPIONs) which can be easily magnetized and concentrated in a specific site by applying an external magnetic field and redispersed again once the magnetic field is removed have also found a recent considerable interest for drug delivery purposes [13].

The production of hydrogel nanoparticles such as acrylate-based hydrogels typically utilizes bioincompatible solvents such as dimethylformamide and acetone. Moreover,

the processing can be costly, and particle size distributions are typically very broad. Thus there is a need for new processes that can efficiently produce nanoparticles with desirable particle size in addition to exploring new biocompatible polymeric systems that ensure the production of the nanoparticles with optimal characteristics using biocompatible solvents relevant to actual clinical use. This current contribution involves the development of a novel spray gelation-based method (aerosol-mediated method) which has been utilized to synthesize a series of magnetically responsive “smart” alginate-based hydrogel nanoparticles for biomedical and drug delivery applications. This method is based on the production of hydrogel nanoparticles from sprayed polymeric microdroplets obtained through an air-jet nebulization process that is immediately followed by a gelation step in a crosslinking fluid. The synthesized magnetically responsive hydrogel nanoparticles are comprised of either sodium alginate or a combination of sodium alginate with oligoguluronate (G-blocks) aerosolized as microdroplets followed by either ionotropic gelation in aqueous  $\text{Ca}^{2+}$  solution or both ionotropic and polyelectrolyte complexation in aqueous solution of PEG-g-chitosan/ $\text{CaCl}_2$  as crosslinkers.

Sodium alginate is a natural nontoxic biodegradable polyanionic copolymer consisting of 1,4-linked  $\beta$ -D-mannuronic acid (M) and  $\alpha$ -L-guluronic acid (G) residues arranged either as consecutive blocks or in a random distribution. Sodium alginate has a unique ability to form hydrogels in the presence of divalent cations such as  $\text{Ca}^{2+}$ ,  $\text{Ba}^{2+}$ , or  $\text{Sr}^{2+}$  ions [14] through lateral association of chain segments (ionotropic crosslinking). It has been reported that this ionotropic chelation/crosslinking occurs particularly between the cations and the G-blocks of alginate as described by the “egg-box” model [15, 16] in which each divalent cation interacts with two adjacent G residues as well as with two G residues in an opposing alginate chain. Therefore, the gel strength of the alginate-based hydrogels depends mainly on the G content in addition to other parameters such as the divalent cation concentration and the concentration and molecular weight of the alginate. It has been also found that sodium alginate has a strong ability to form hydrogels via polyelectrolyte complexation with cationic polymers such as chitosan (Cs) and its derivatives [14].

Chitosan (Cs), a cationic polymer obtained through the alkaline N-deacetylation of chitin, has various desirable properties such as nontoxicity, biodegradability, and biocompatibility [17]. Grafting of various synthetic polymers onto the Cs backbone can further improve its characteristics and accordingly expand its potential applications. One of these polymers that is commonly grafted onto Cs is the poly(ethylene glycol) (PEG). PEG is a water-soluble nontoxic and biocompatible polymer [18]. Owing to the characteristics of PEG, the development of polymeric micro- and nanohydrogel particles based on PEG graft copolymerized onto Cs (PEG-g-Cs) has received increased attention in many applications specifically for drug delivery purposes [19–22].

In this study, oligoguluronate residues (G-blocks) were prepared through partial acid hydrolysis of sodium alginate. PEG-g-Cs was also synthesized and characterized. Then a new series of magnetic hydrogel nanoparticles was developed

using a new method. The magnetic hydrogel nanoparticles are based on a combination of alginate with the G-blocks and crosslinked either with  $\text{Ca}^{2+}$  (ionotropic gelation) or through polyelectrolyte complexation with the cationic PEG-g-Cs.

## 2. Materials and Methods

**2.1. Materials.** Chitosan (medium MW, %N-deacetylation; 76.4%, as determined by FTIR spectroscopy and elemental analysis), monomethoxy-poly-(ethylene glycol) (m-PEG, Mn 5 kDa), succinic anhydride, and 1-hydroxybenzotriazole (HOBr) were supplied by Aldrich (USA). 1-Ethyl-3-(3-dimethylaminopropyl) carbodiimide hydrochloride (EDC.HCl) was obtained from Fluka Chemical Corp. (Milwaukee, WI, USA). 4-Dimethylaminopyridine (DMAP) was provided by Sigma (St. Louis, MO, USA). Sodium alginate (low viscosity; 250 cps for a 2% solution at 25°C), phthalic anhydride, dioxane, triethyl amine, and dimethyl formamide (DMF) were obtained from Sigma-Aldrich (St Louis, MO, USA). The superparamagnetic iron oxide nanoparticles (SPIONs) and fluidMAG-D of size 100 nm were purchased from Chemicell (Berlin, Germany). Ethanol, phosphate buffer saline (PBS pH 7.4), and all other reagents were of analytical grade and used as received.

### 2.2. Methods

**2.2.1. Preparation of Oligoguluronate (G-Blocks).** The oligoguluronate residues (G-blocks) were prepared using a method similar to that described by Haug et al. [23, 24]. Briefly, sodium alginate (10 g) was dissolved in distilled water and made up to 1 L with 0.3 M HCl. The mixture was then heated at 100°C for 6 h. The oligomannuronate and oligoguluronate homopolymeric blocks that remained intact as solid residues were collected via centrifugation for 5 min at 4000 rpm, washed, and resuspended in distilled water. The residue was dissolved by the dropwise addition of 0.3 M NaOH. Afterwards, NaCl was added to make up a final concentration of 0.5% (w/v). Ethanol (2 volumes) was added and the resulting precipitate was collected by centrifugation for 5 min at 4000 rpm. The precipitate was then washed and redissolved in water, and the pH was adjusted to 2.85 with 1 M HCl. At this pH value, the oligoguluronate blocks were precipitated and then collected leaving the oligomannuronate blocks in solution. The oligoguluronate fractions were desalted and freeze-dried.

**2.2.2. Preparation of Cs Grafted with PEG.** The PEG-g-Cs copolymer was synthesized as described in our earlier study [25] and summarized as follows.

(i) **Preparation of N-Phthaloyl Cs (NPHCs).** Phthalic anhydride (44.8 g, 5 mol equivalent to pyranose rings) was allowed to react with 10 g of Cs in 200 ml DMF at 130°C under dry nitrogen atmosphere for 8 h. The resulting NPHCs (pale brown solid) was then collected by filtration after precipitation in ice-water, washed with methanol, and dried under vacuum at 40°C.

(ii) Preparation of m-PEG-COOH. m-PEG (100 g, 20 mmol), DMAP (2.44 g, 20 mmol), triethylamine (2.02 g, 20 mmol), and succinic anhydride (2.4 g, 24 mmol) were dissolved in dry dioxane (350 ml) and then stirred for 2 days at room temperature under a dry nitrogen atmosphere. The dioxane was evaporated using a rotary evaporator, and the residue was taken up in CCl<sub>4</sub>, filtered, and precipitated by diethyl ether to produce m-PEG-COOH (white powder).

(iii) Preparation of PEG-g-NPHCs. m-PEG-COOH (37.9 g) and NPHCs (5.0 g, 0.4 mol equivalent to m-PEG-COOH) were dissolved in 75 ml of DMF. The HOBT (3.4 g, 3 mol equivalent to m-PEG-COOH) was then added, as a catalyst, with stirring at room temperature until obtaining a clear solution. Afterwards, the EDC.HCl (4.25 g, 3 mol equivalent to m-PEG-COOH) was added, and the mixture was stirred overnight at room temperature. A purified PEG-g-NPHCs copolymer (5.47 g, white solid) was obtained after dialysis of the reaction mixture against distilled water and washing with ethanol.

(iv) Preparation of PEG-g-Cs. The PEG-g-NPHCs (4.0 g) was dissolved in 15 ml of DMF and heated to 100°C with stirring under nitrogen. Afterwards, 20 ml of hydrazine monohydrate was added, and the reaction was continued for 2 h. The resulting PEG-g-Cs copolymer was purified via dialysis against a mixture of deionized ethanol and water (1 : 1) then dried under vacuum at 40°C.

NPHCs. FTIR ( $\nu_{\text{max}}$ , cm<sup>-1</sup>): 3281(OH stretching and NH bending), 2961 (C–H stretching), 1775, and 1698 (C=O anhydride), 1395 (C=C, phthaloyl), 1058 (C–O, pyranose), and 732 (aromatic ring of phthaloyl). Elemental analysis (EA), (C<sub>8</sub>H<sub>13</sub>NO<sub>5</sub>)<sub>0.2363</sub> (C<sub>6</sub>H<sub>11</sub>NO<sub>4</sub>)<sub>0.016</sub> (C<sub>14</sub>H<sub>13</sub>NO<sub>6</sub>)<sub>0.747</sub>, Anal. calculated (DS = 0.98) (%): C, 55.74; H, 4.84; N, 5.23, found (%): C, 60.31; H, 4.83; N, 4.92. m-PEG-COOH; FTIR ( $\nu_{\text{max}}$ , cm<sup>-1</sup>) 3496 (OH stretching), 2882 (C–H stretching), 1733 (C=O of carboxylic group), and 1102 (C–O–C stretching); EA, (C<sub>231</sub>H<sub>460</sub>O<sub>117</sub>), Anal. calculated (%): C, 54.35, and H, 9.02, found (%): C, 56.8, and H, 9.19. PEG-g-NPHCs (5.47 g); FTIR ( $\nu_{\text{max}}$ , cm<sup>-1</sup>) 3423 (OH stretching and NH bending), 2879 (C–H stretching), 1736 (C=O ester and anhydride), 1703 (C=O anhydride), 1096 (C–O–C stretching), and 723 (aromatic ring of phthaloyl). EA, found (%): C, 56.16; H, 4.69; N, 5.15. PEG-g-Cs; FTIR ( $\nu_{\text{max}}$ , cm<sup>-1</sup>) 3312 (OH stretching, NH bending, and intermolecular H-bonding), 2879 (C–H stretching), 1708 (C=O ester), and 1096 (C–O–C stretching). EA, found (%): C, 40.46; H, 4.71; N, 14.44.

**2.2.3. Characterization of the Synthesized Polymers.** The elemental analysis (EA) was carried out using Costech ECS4010 elemental analyzer coupled to a Thermo-Finnigan Delta Plus isotope ratio mass spectrometer. The FTIR spectra were recorded using Nicolet 6700 FTIR spectrometer, and the differential scanning calorimetry (DSC) was carried out using a DSC 2920 (Modulated DSC, TA Instruments) in a nitrogen atmosphere with a temperature range of -40°C

to 400°C at a heating rate of 10°C min<sup>-1</sup> for preweighed samples of 10–15 mg. The peaks' temperatures and the enthalpy values were recorded.

**2.2.4. Preparation of the Magnetic Hydrogel Nanoparticles Using a Novel Aerosol-Mediated Method.** The magnetic hydrogel nanoparticles were prepared using a novel aerosol-assisted method. This method depends on the manufacture of hydrogel nanoparticles from sprayed polymeric microdroplets obtained by an air-jet nebulization process which is immediately followed by gelation/hardening in a collecting crosslinking fluid. Specifically, 2% w/v aqueous solutions of either sodium alginate or mixtures of sodium alginate with oligoguluronate of different compositions (Table 1) were prepared. Also, a 0.1% w/v aqueous solution of the synthesized copolymer, PEG-g-Cs, was prepared by dissolving it in 10 ml of 0.06 M acetic acid and made up to the precalculated volume with distilled water. Predetermined volumes of the SPIONs suspensions were added to the alginate or alginate/oligoguluronate solutions (3% SPIONs based on the total polymer weight) and homogenously distributed by sonication for 2 min. Then, the polymer/SPIONs mixtures were transferred to an Aerotech II air-jet nebulizer and aerosolized with the aid of compressed air delivered at a controlled pressure of 30 psi. The generated aerosols of SPIONs/polymer microdroplets were directed, under vacuum, into 10 ml of a crosslinking solution of either CaCl<sub>2</sub> (0.2 M) or a (1 : 1) mixture of PEG-g-Cs/CaCl<sub>2</sub> under continuous mild stirring. The resulting suspensions of the swollen magnetic hydrogel nanoparticles were collected and freeze dried. The dried hydrogel powders were then washed with distilled water to remove any residual crosslinker and then refreezing-dried. The yield (%) of the resulting dry powders of hydrogel nanoparticles was determined, and the powders were stored in a desiccator at room temperature until further use.

**2.2.5. Determination of Hydrogel Particle Size.** The average size of the prepared magnetic hydrogel nanoparticles suspended in 2 ml of ethanol (0.2% w/v) was determined by dynamic light scattering (DLS) (Malvern nanosizer, Malvern Instruments Ltd., Worcestershire, UK). The size of the particles was also estimated using microscopy techniques including light microscopy (Leica DMI6000B scope) with Leica Application Suite Advanced Fluorescence 2.2.0 build 4765 software. The average diameters ( $d$ , nm) of about 100 magnetic hydrogel nanoparticles ( $n = 100$ ) were recorded.

**2.2.6. Surface Morphology of Hydrogel Nanoparticles.** The morphology of the developed magnetic hydrogel nanoparticles was investigated by SEM (Zeiss supra 40 VP scanning electron microscope). Dry magnetic nanoparticles were mounted on aluminum stubs with double-sided conducting carbon tapes and coated with a 50/50 mixture of Pt/Pd to minimize surface charging. The samples were scanned at an accelerating voltage of 10 kV.

TABLE 1: Different compositions and particle size of the developed magnetic hydrogel nanoparticles.

Formulation code	Polymer aq. solution (2% w/v)		Crosslinking fluid		Particle size, ( $d$ , nm) $\pm$ SD		
	Alginate (w%)	G-block (w%)	CaCl <sub>2</sub> (0.2 M)	CaCl <sub>2</sub> /PEG-g-Cs (1:1)	<sup>1</sup> Dry (DLS)	<sup>2</sup> Dry (LM)	<sup>2</sup> Swelled (LM)
IA	100	00	†	—	936 $\pm$ 40	852 $\pm$ 145	1546 $\pm$ 84
IB	100	00	—	†	926 $\pm$ 13	811 $\pm$ 105	1498 $\pm$ 102
IIA	80	20	†	—	811 $\pm$ 162	770 $\pm$ 122	1571 $\pm$ 61
IIB	80	20	—	†	929 $\pm$ 12	794 $\pm$ 177	1427 $\pm$ 179
IIIA	70	30	†	—	941 $\pm$ 2	855 $\pm$ 89	1640 $\pm$ 75
IIIB	70	30	—	†	886 $\pm$ 2	800 $\pm$ 152	1592 $\pm$ 126

<sup>1</sup>Determined using DLS. <sup>2</sup>Estimated using light microscopy (LM).

**2.2.7. Transmission Electron Microscopy Analysis of Hydrogel Nanoparticles.** A Jeol 2010F field emission transmission electron microscope (TEM) was used to obtain transmission electron micrographs of the developed magnetic hydrogel nanoparticles at accelerating voltage of 200 kV. Also, the iron and calcium contents of the particles were estimated using energy-dispersive X-ray spectroscopy (EDS) (Oxford INCA) attached to the TEM with the aid of silicon detector at an accelerating voltage of 20 kV and a magnification of 120,000X.

**2.2.8. Dynamic Swelling Study of Hydrogel Nanoparticles.** The swelling characteristics of the developed magnetic hydrogel nanoparticles (2-3 mg) in 500  $\mu$ L of PBS (pH 7.4) were investigated by determining the increase in the particle diameter ( $d$ , nm) at different time intervals; 2, 5, and 10 min using light microscopy (Leica DMI6000B scope) with Leica Application Suite Advanced Fluorescence 2.2.0 build 4765 software.

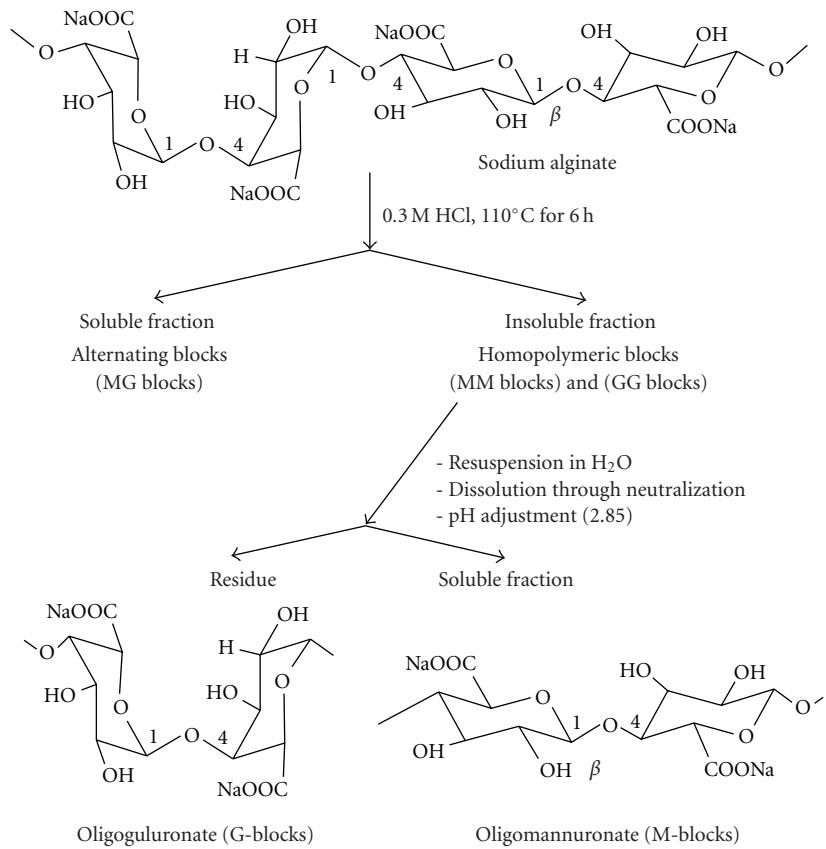
**2.2.9. Statistical Analysis and Optimization of the Magnetic Hydrogel Nanoparticles by a  $2^k$  Factorial Design.** The obtained results were analyzed and expressed as mean  $\pm$  SD. A  $2^k$  factorial design was used to estimate the effect of the different formulation's parameters such as the alginate % and the type of crosslinking agent on the characteristics of the developed magnetic hydrogel nanoparticles such as particle size and equilibrium swelling for further optimizations. Also, the statistical significance was analyzed using ANOVA (Statgraphics Plus version 5.0 software). Differences were considered significant at the level of  $P < .05$ .

### 3. Results and Discussion

**3.1. Preparation of Oligoguluronate (G-Blocks).** The oligoguluronate residues (G-blocks) were obtained through the partial acid hydrolysis of sodium alginate followed by fractionation of the products. The hydrolysis was achieved using dilute HCl in boiling water through a method similar to that described by Haug et al. [23, 24]. The partial hydrolysis process of the alginate led to two fractions; the soluble fraction consists mainly of blocks with an alternating sequence of mannuronic and guluronic acid residues (MG blocks) whereas the insoluble fraction consists

of homopolymeric blocks of mannuronic acid (MM blocks) and guluronic acid residues (GG blocks) as illustrated in Scheme 1. The fractionation process was achieved through collecting the oligomannuronic (MM) and oligoguluronate (GG) homopolymeric blocks that remained intact as residues via centrifugation. This separated mixture of homopolymeric blocks was resuspended in water and then dissolved through neutralization with dilute alkali (NaOH, 0.3 M). Afterwards, the oligoguluronate blocks were precipitated and collected leaving the oligomannuronate blocks in solution via adjusting the pH value of the homopolymeric mixtures at 2.85.

**3.2. Synthesis of PEG-Cs Graft Copolymer.** The PEG-g-Cs copolymer was synthesized through a modified method reported in our earlier study [25]. The copolymer synthesis started with the modification of m-PEG into carboxyl-capped m-PEG precursor (m-PEG-COOH) using succinic anhydride. The prepared m-PEG-COOH was characterized using EA and FTIR. The free NH<sub>2</sub> groups of Cs were protected through phthaloylation process using phthalic anhydride to produce N-phthaloyl Cs (NPHCs). The preparation of NPHCs was confirmed by FTIR through appearance of peaks at 1395 and 732 cm<sup>-1</sup> which stand for the “aromatic C=C” and “aromatic C-H” bonds of the phthaloyl moieties, respectively. Afterwards, grafting of m-PEG-COOH onto NPHCs was carried out in DMF, and the grafting % of the resulting PEG-g-NPHCs was found to be about 9.3%. The resulting PEG-g-NPHCs copolymer was also characterized by EA and FTIR. The PEG-g-Cs copolymer was then produced through the dephthaloylation of the protected NH<sub>2</sub> groups of PEG-g-NPHCs copolymer using hydrazine monohydrate. The overall synthesis of the PEG-g-Cs copolymer is demonstrated in Scheme 2. The synthesis of the PEG-g-Cs copolymer was confirmed by comparing the FTIR spectra of the copolymer with those of the starting material (Cs) as shown in Figure 1. The synthesis of the PEG-g-Cs was also proved by studying its thermal behavior in comparison with that of starting materials, PEG-COOH and Cs, as apparent in Figure 2. For instance, the DSC thermogram of PEG-COOH (Figure 2(a)) showed an endothermic band at about 65°C which stands for its melting process. In case of the Cs thermogram (Figure 2(b)), it shows an endothermic peak started at about



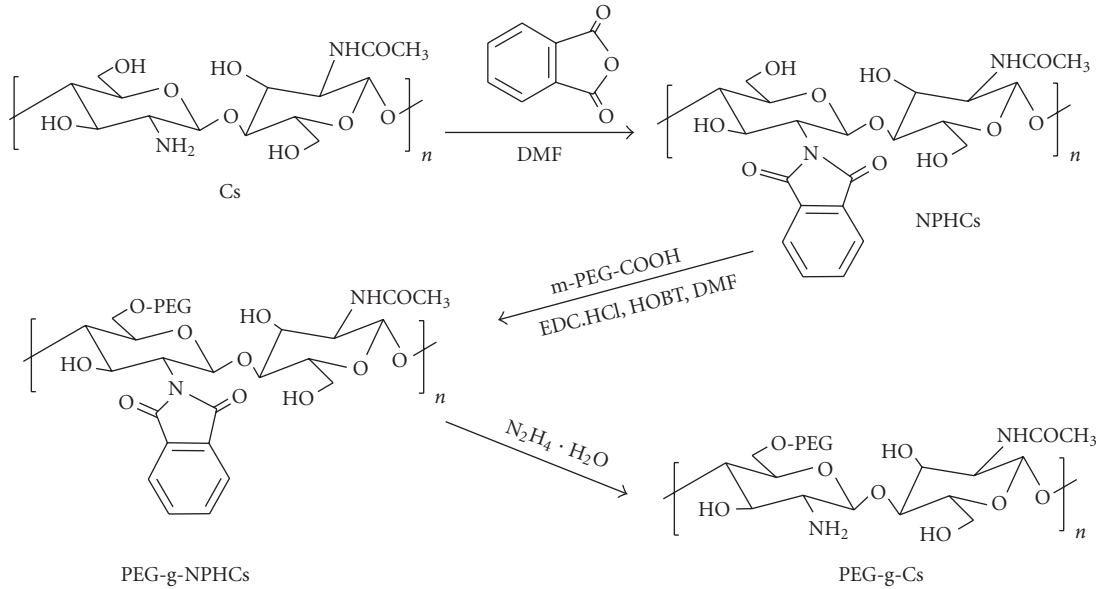
SCHEME 1: Schematic illustration of the preparation of oligoguluronate blocks (G-blocks).

90°C, which can be ascribed to the loss of bound water. The Cs thermogram shows also an exotherm at 312°C which may be attributed to the decomposition of the glucosamine units [26, 27]. The thermogram of PEG-g-Cs (Figure 2(c)) shows an endothermic peak at 55°C which can be attributed to the melting of the grafted PEG side chains. Also, an endotherm was observed at 119°C which is due to the loss of bound water. The exotherms appearing at 261 and 310°C may be ascribed to the crystallization and decomposition of the PEG-g-Cs copolymer, respectively.

**3.3. Aerosol-Assisted Preparation of the Magnetic Hydrogel Nanoparticles.** The magnetic hydrogel nanoparticles developed in this study were obtained using a novel spray method as illustrated in Figure 3(a). The system consists of a regulated source of compressed air connected directly to an air-jet nebulizer that delivers the polymeric solutions as sprayed microdroplets to a feed zone comprising tubing carrying droplets. This tubing was assembled to one or more of aerodynamic aerosol classifiers connected to a secondary vacuum system responsible of transporting the sprayed droplets to the crosslinker solution (collecting fluid). Then, an alternate empty glass collector was directly assembled to the primary vacuum system to recover the large hydrogel nanoparticles dragged from the secondary vacuum system.

The prepared hydrogel nanoparticles are based on either sodium alginate or a combination of sodium alginate with

oligoguluronate residue (G-blocks) aerosolized as micro-droplets followed by either ionotropic gelation in aqueous  $\text{Ca}^{2+}$  solution or both ionotropic and polyelectrolyte complexation in (1:1) aqueous solution of PEG-g-Cs/CaCl<sub>2</sub> as crosslinkers as illustrated in Figure 3(b). In case of the ionotropic gelation of sodium alginate with  $\text{Ca}^{2+}$ , the carboxylate groups of subsequent guluronate (G) units in the alginate chains have suitable geometry and spacing for the binding with the  $\text{Ca}^{2+}$  ions [28]. This affinity of the G units towards binding with the  $\text{Ca}^{2+}$  has been found to be higher than their mannuronate (M) counterparts [29]. Also, this type of binding has been described by the “egg-box” model [15, 16]. Therefore, the gel strength of alginate-based hydrogels depends mainly on the G content of the alginate in addition to the other factors such as the calcium ion concentration and the molecular weight and concentration of the alginate. In a recent study [14], free G-blocks were added to alginate solutions and the effects of this addition onto the gel strength, gelling kinetics, and syneresis of the formed alginate-based hydrogels were investigated. The results of the study showed that the free G-blocks are involved in the  $\text{Ca}^{2+}$ -mediated bonds formed between guluronic acid sequences within the polymeric alginates (Figure 3(b)) [14]. In other words, the added oligoguluronate (G-blocks) competes with the alginate chains for the  $\text{Ca}^{2+}$  ions. However, the study indicated that the presence of free G-blocks led to an increase in the gelation time. Also, the gel strength of the formed



SCHEME 2: Schematic illustration of the synthesis of PEG-g-Cs copolymer.

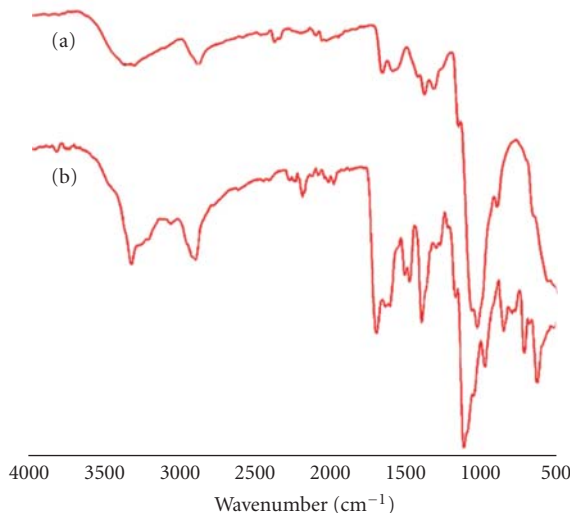


FIGURE 1: FTIR spectra of (a) Cs as compared to (b) the synthesized PEG-g-Cs copolymer.

alginate hydrogels was found to decrease with increasing amount of the free G-blocks. This reduction in the gel strength can be attributed to the lower molecular weight and viscosity of the added oligoguluronate (G-blocks) as compared to the polymeric alginate.

The developed hydrogel nanoparticles showed a considerable magnetically responsive nature as apparent in Figure 4. The figure reveals the relatively fast response of the hydrogel nanoparticles in their aqueous suspension to an external magnetic field.

#### 3.4. Particle Size Analysis of Hydrogel Nanoparticles.

Development of magnetic nanoparticles with appropriate size

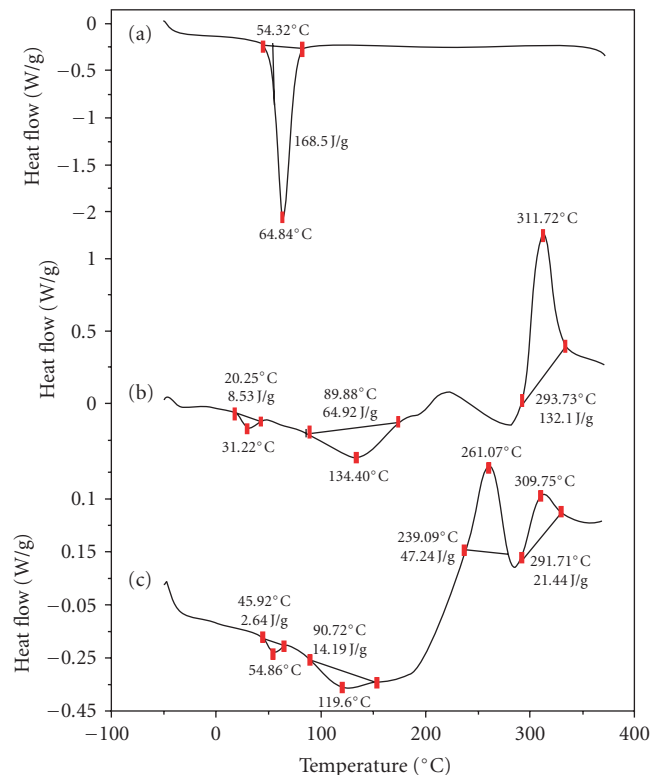


FIGURE 2: DSC characterizations of the synthesized PEG-g-Cs copolymer (c) as compared to the starting materials; (a) PEG-COOH and (b) Cs.

represents an important issue in many applications. As shown in Table 1, the size of the developed magnetic hydrogel nanoparticles was found to be in the range of  $811 \pm 162$  to  $941 \pm 2$  nm as determined by dynamic light scattering

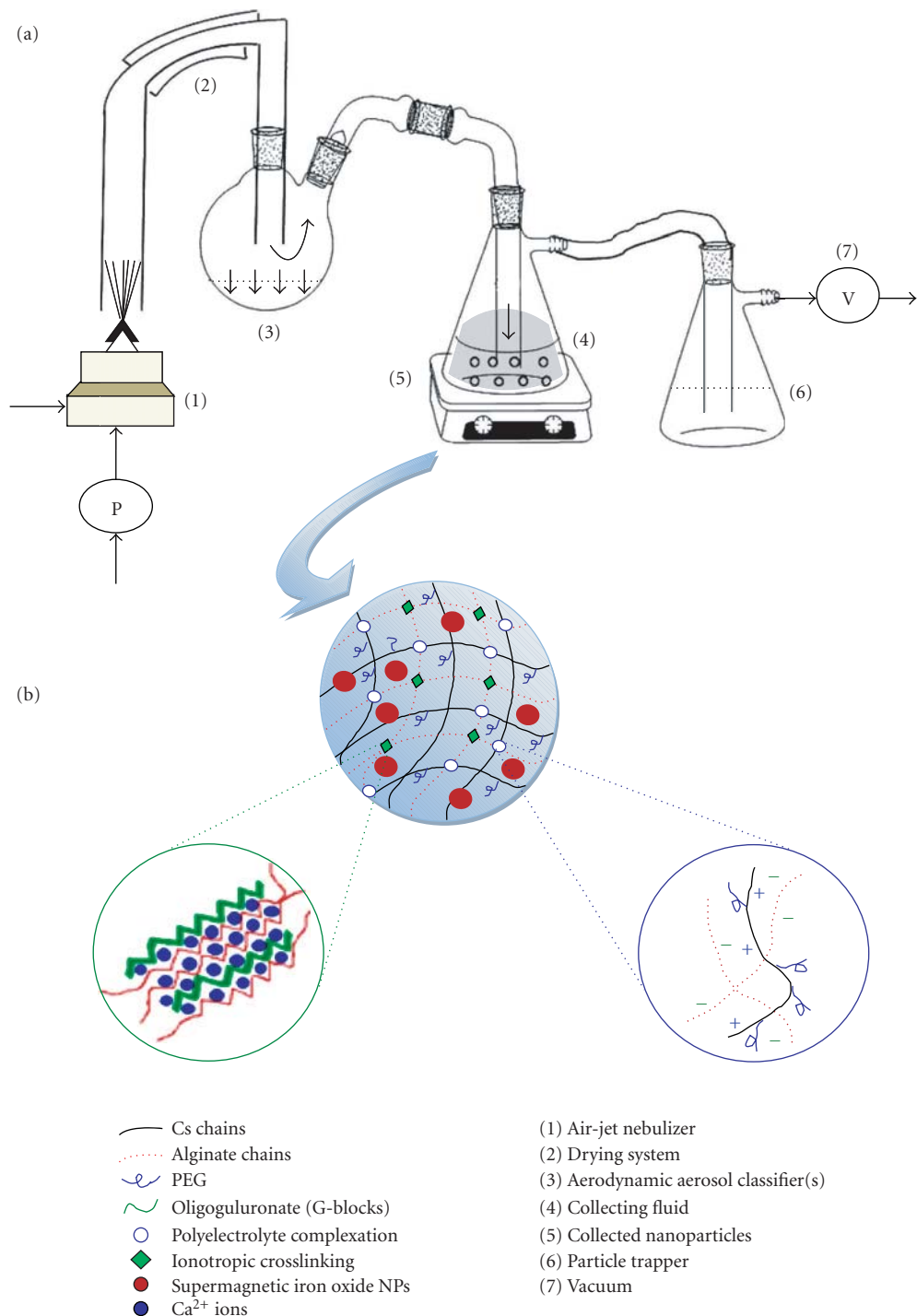


FIGURE 3: (a) An illustration of the new spray gelation-based method used in the development of the hydrogel nanoparticles. (b) Schematic illustration of the developed magnetically responsive hydrogel nanoparticles.

(DLS). From the table, it seems, in most formulations, that crosslinking of the hydrogel nanoparticles with a mixture of Ca<sup>2+</sup>/PEG-g-Cs (1:1) relatively reduces the particle size as compared to the particles crosslinked with only one crosslinking agent (Ca<sup>2+</sup>). For instance, the particles IIIA (crosslinked with Ca<sup>2+</sup> only) showed an average size of  $941 \pm 2$  nm when analyzed by DLS. This size was reduced

to  $886 \pm 2$  nm in case of the particles IIIB (crosslinked with Ca<sup>2+</sup>/PEG-g-Cs). This effect of the crosslinking agents on the size of the developed hydrogel nanoparticles was found to be statistically significant ( $P = .0415$ ). Also, it was noted from the size data that, in general, increasing the percentage of alginate in the magnetic hydrogel nanoparticles has no significant effect on the particle size ( $P = .7702$ ). This can

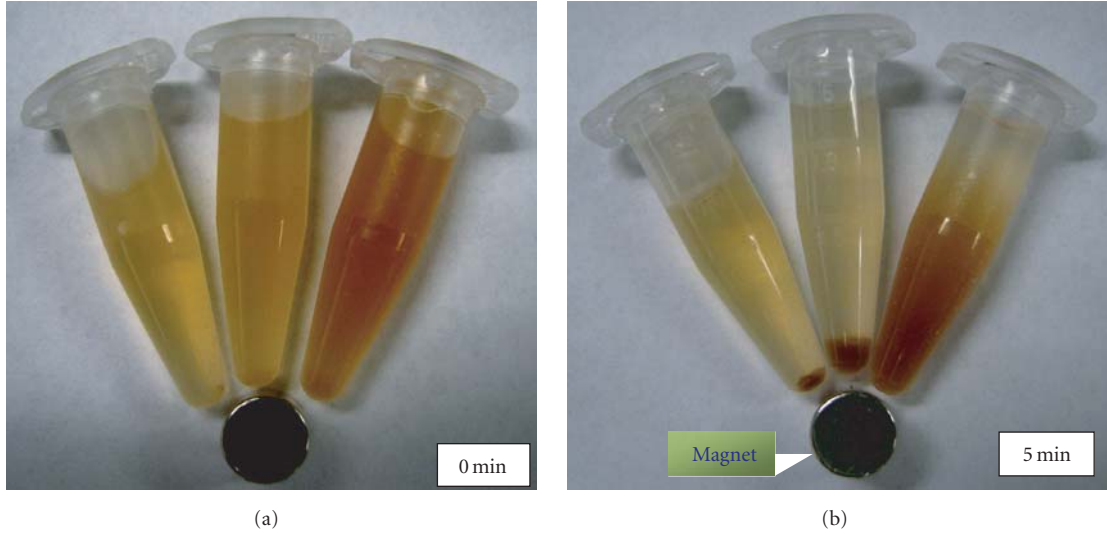


FIGURE 4: Photographs showing the magnetic nature of the developed hydrogel nanoparticles (aqueous suspensions of different concentrations).

be attributed to the fact that not only sodium alginate but also the oligoguluronate (G-blocks) is participating in the crosslinking process either ionotropically with the  $\text{Ca}^{2+}$  ions or through polyelectrolyte complexation with the cationic PEG-g-Cs copolymer [14]. These effects of both the type of crosslinking agent and alginate % on the particle size were also confirmed through the particle size determinations using light microscopy as shown in Table 1. Further studies have been initiated to assess particle size modulation using different experimental parameters (as discussed below).

**3.5. Scanning Electron Microscopy Analysis of the Hydrogel Nanoparticles.** Figure 5 shows the scanning electron micrographs of some of the developed magnetic hydrogel nanoparticles. From the figure, the hydrogel nanoparticles have, in general, spherical shapes with relatively smooth surfaces. However, the extent of surface regularity and smoothness seems to vary upon changing the type of the used crosslinking agent. For instance, the hydrogel nanoparticles developed using only  $\text{Ca}^{2+}$  as a crosslinking agent (Figure 5(a)) showed a spherical morphology with highly smooth, dense, and integrated surfaces. However, nanoparticles showed a relatively rough surface when crosslinked with a mixture of  $\text{Ca}^{2+}$  and PEG-g-Cs (Figure 5(b)). This surface morphology of the nanoparticles crosslinked with both  $\text{Ca}^{2+}$  and PEG-g-Cs can be seen more clearly in Figure 5(c).

**3.6. Transmission Electron Microscopy Analysis of the Hydrogel Nanoparticles.** Figure 6(a) shows the TEM images of the developed magnetic hydrogel nanoparticles. The figure reveals a relatively homogenous distribution of the magnetic cores (SPIONs) throughout the matrix of the hydrogel particles. The content of the iron cores (atomic %) within the hydrogel nanoparticles was also estimated with the aid of energy-dispersive X-ray spectroscopy (EDS) as illustrated

in Figure 6(b). From the figure, the atomic iron content (%) was found to be about 20%.

**3.7. Dynamic Swelling Study of the Hydrogel Nanoparticles.** The swelling patterns of the prepared magnetic hydrogel nanoparticles in PBS, pH 7.4 are illustrated in Figures 7 and 8. The swelling data was obtained by measuring the increase in the diameters ( $d$ , nm) of the hydrogel nanoparticles with time using light microscopy. From the swelling data, it seems that the hydrogel nanoparticles prepared using a mixture of  $\text{Ca}^{2+}$  and PEG-g-Cs as a crosslinking agent attained relatively lower swelling values than the corresponding formulations that crosslinked only with  $\text{Ca}^{2+}$ . For instance, after 10 min of swelling, the hydrogel nanoparticles, IIIB (crosslinked with both  $\text{Ca}^{2+}$  and PEG-g-Cs), attained a swelled size of  $1592 \pm 126$  nm as compared to the nanoparticles, IIIA (crosslinked with  $\text{Ca}^{2+}$ ), which attained a swelled size of  $1639 \pm 75$  nm. This behavior can be attributed to increasing the crosslinking extent of the particles upon using two types of crosslinkings (ionotropic and polyelectrolyte complexation) than using only ionotropic crosslinking with  $\text{Ca}^{2+}$ . This effect of the crosslinker type on the swelling values attained at equilibrium was found to be statistically significant ( $P = .0001$ ). Moreover, from the swelling patterns shown in both Figures 7 and 8, although both alginate and oligoguluronate (G-blocks) contribute in the crosslinking process, it seems, in general, that increasing the alginate percentage in the developed nanoparticles tends to increase the crosslinking extent and consequently reduces the swelled sizes. This confirms the higher ability of the alginate as compared to the G-blocks to interact with the crosslinking agents, which is in agreement with the literature [14]. Figure 9 shows some microscopic images that illustrate the differences in size of some developed magnetic hydrogel nanoparticles, including before and after attaining the equilibrium swelling.

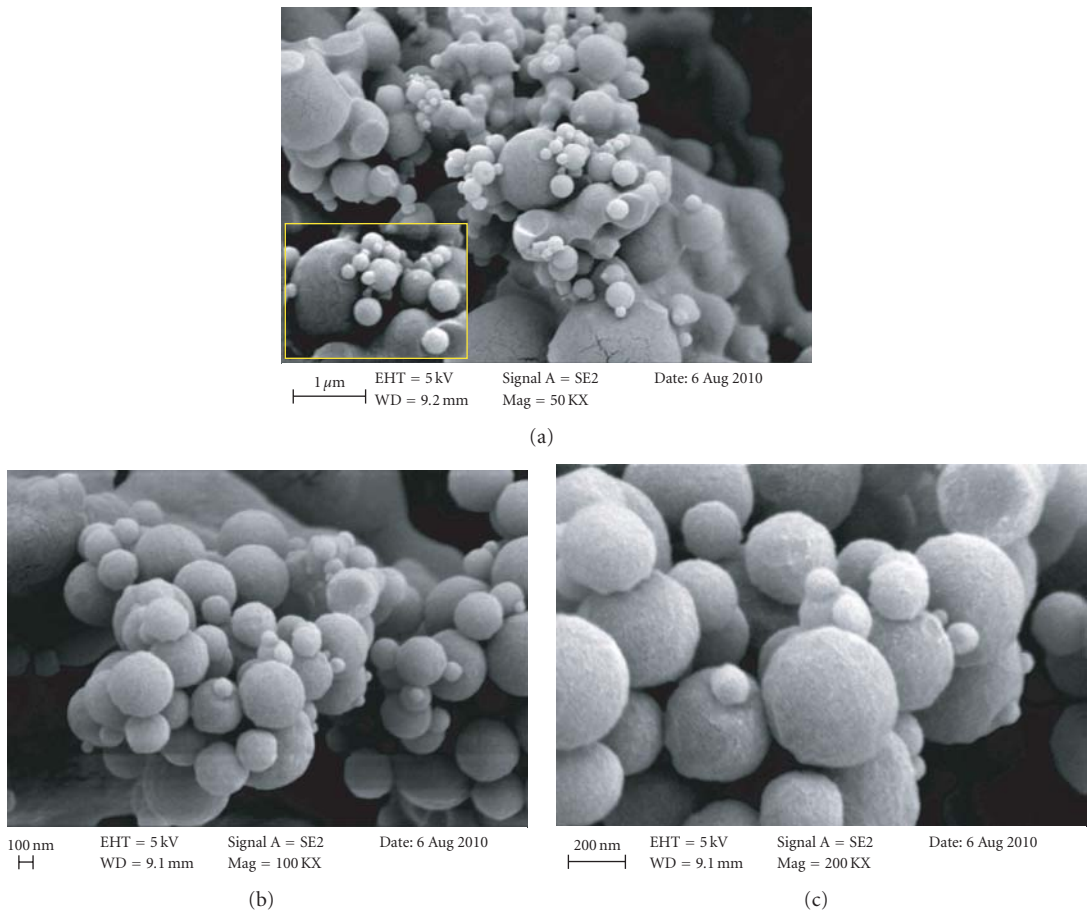


FIGURE 5: Scanning electron micrographs of some developed magnetic hydrogel nanoparticles; IIIA (a) and IIIB (b and c) showing the spherical nature of the developed nanoparticles.

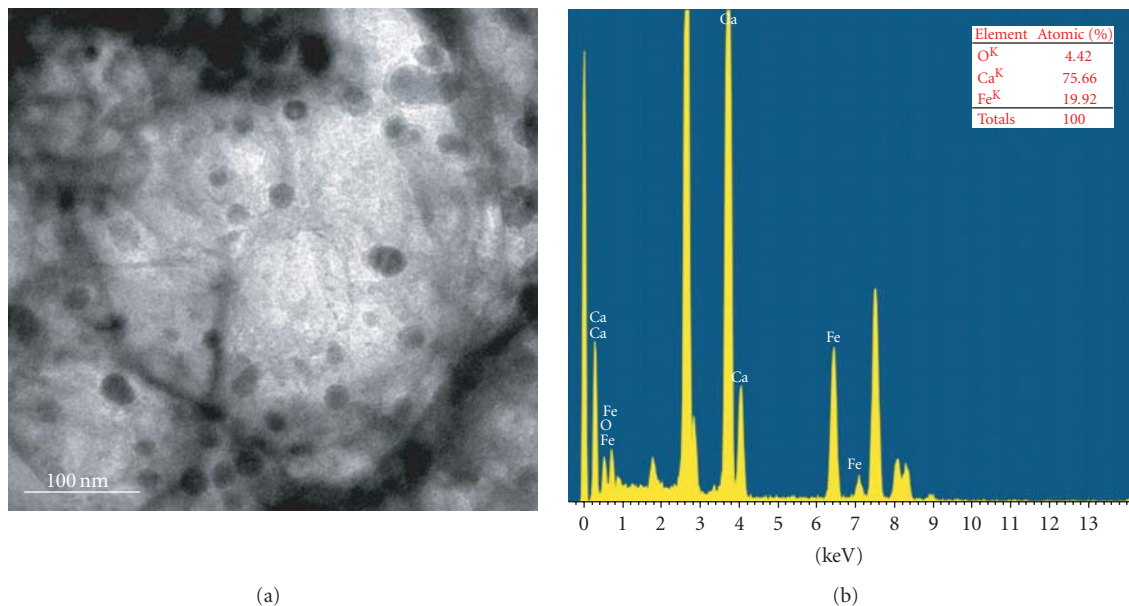


FIGURE 6: (a) Transmission electron micrographs (TEM) of the developed magnetic hydrogel nanoparticles. (b) The iron and calcium contents of the magnetic hydrogels as determined by the EDS.

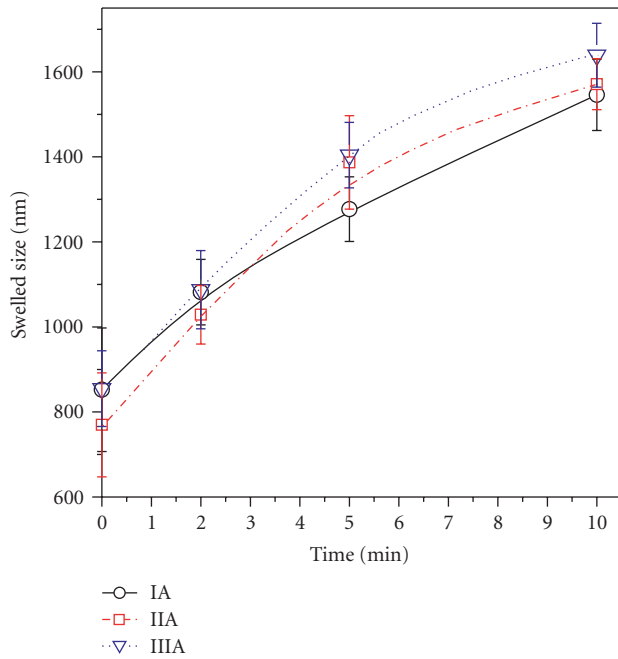


FIGURE 7: Dynamic swelling of the magnetic hydrogel nanoparticles crosslinked with  $\text{CaCl}_2$  in PBS, 7.4.

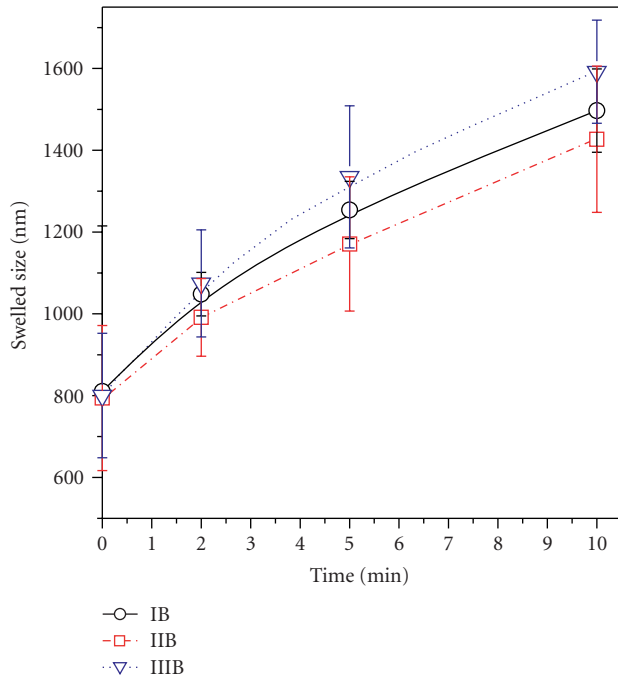
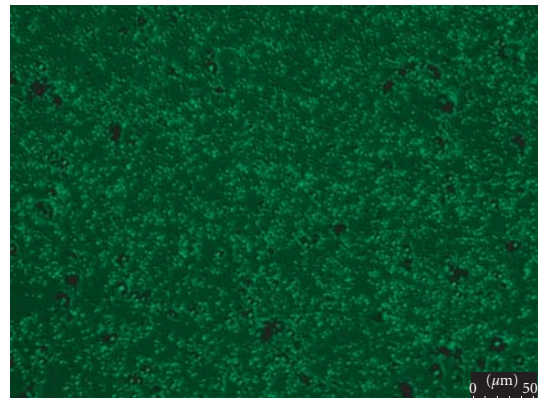


FIGURE 8: Dynamic swelling of the magnetic hydrogel nanoparticles crosslinked with  $\text{CaCl}_2/\text{PEG-g-Cs}$  (1 : 1) in PBS, 7.4.

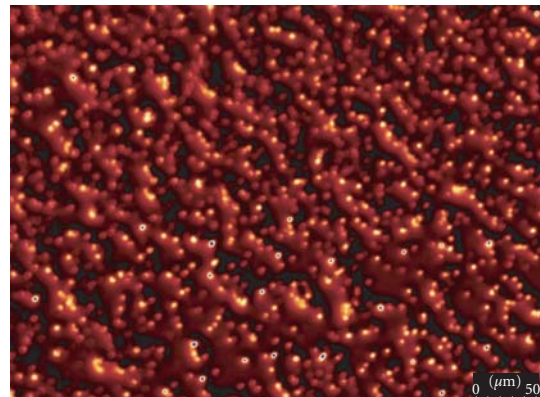
**3.8. Analysis of the Characteristics of the Magnetic Hydrogel Nanoparticles by a  $2^k$  Factorial Design.** A discontinuous  $2^k$  factorial design was performed to investigate the effect of the alginate % and type of crosslinking agent and their interaction on the characteristics of prepared magnetic hydrogel nanoparticles. The analysis was performed using Pareto



(a)



(b)



(c)

FIGURE 9: Microscopic images illustrating the differences in size of some developed magnetic hydrogel nanoparticles (a) dry IIIB NPs, (b) dry IIIA NPs, and (c) swelled IIIA NPs in PBS, pH 7.4.

charts, response surface methodology, and the contour of estimated response surface for three levels of variations in the alginate (%) factor (70, 80, and 100%, coded as -1, 0, and +1, resp.) plus two levels of variations in the second factor, the crosslinker type ( $\text{Ca}^{2+}$  and  $\text{Ca}^{2+}/\text{copolymer}$ , coded as -1 and +1, resp.). Both the particle size and equilibrium swelling values were used as response variables. The analysis

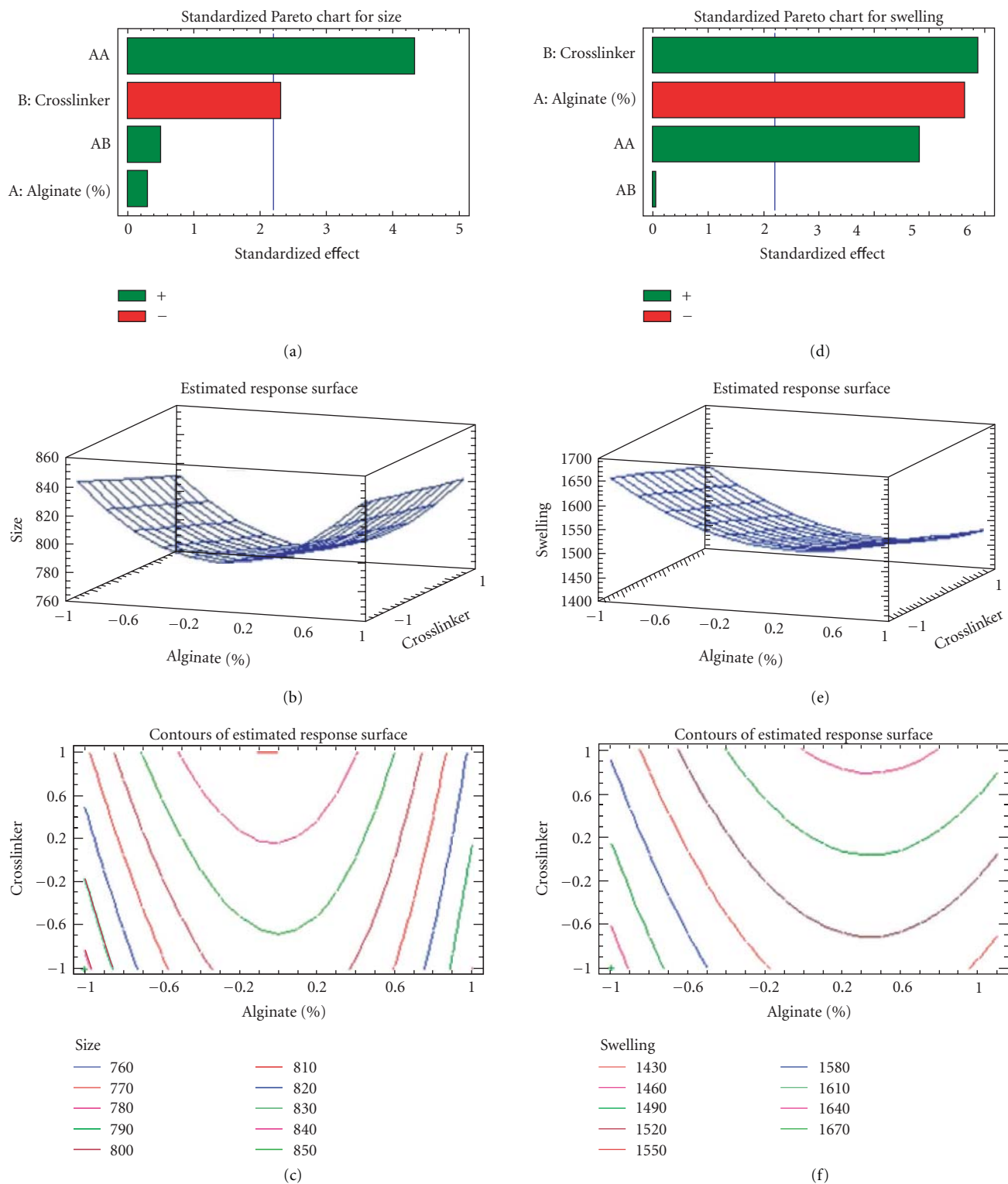


FIGURE 10: Statistical analysis of the effect of the formulation's parameters on both particle size and equilibrium swelling of the developed magnetic hydrogel nanoparticles.

of variance for both particle size and equilibrium swelling was performed by Statgraphics 5.0, and the most influential factors were estimated at 95% confidence level.

In case of particle size, as apparent from the standardized Pareto chart (Figure 10(a)), the type of crosslinking agent can be considered the main factor that controls the size of the developed magnetic hydrogel nanoparticles, but as mentioned previously, these differences in particle size do not appear to be practically significant. The surface response methodology was also applied to investigate the way in which the particle size would respond to the parameters variations (Figure 10(b)). The diagram reveals that the smallest particle sizes were obtained when the alginate % was maintained between -0.2 and +0.2 (knowing that -1 and +1 correspond to 70% and 100% alginate, resp.) with the use of a crosslinker mixture (coded as +1). These obtained results are consistent with the particle size data determined experimentally and can be used in future studies to design experimental parameters that may result in a wider range of particle sizes produced. These parameters include the following, among other factors, different atomizer output particle size, drying/conditioning of aerosol prior to crosslinking, concentrations of the hydrogel components, and reaction temperatures.

In the case of the equilibrium swelling, as shown in the standardized Pareto chart (Figure 10(d)), the type of crosslinking agent can be considered the major factor that controls the equilibrium swelling of the hydrogel nanoparticles, followed closely by the alginate %. Hence, variation of any of these two parameters would likely have a more relevant influence on the swelling values attained at equilibrium. As apparent in the surface response diagram (Figure 10(e)), the lowest swelling values were attained when the alginate % was maintained in its higher value (+1 corresponding to 100%) with the use of a  $\text{Ca}^{2+}$ /copolymer mixture as a crosslinking agent (coded as +1). These results are in agreement with the equilibrium swelling data as determined experimentally.

## 4. Conclusion

A new series of magnetically responsive “smart” hydrogel nanoparticles based on alginate-oligoguluronate was developed using a novel spray gelation-based method. The magnetic nanoparticles showed promising characteristics which can be further optimized by controlling the parameters of the used new method in addition to controlling the relative compositions of the polymeric components.

## References

- [1] Y. Qiu and K. Park, “Environment-sensitive hydrogels for drug delivery,” *Advanced Drug Delivery Reviews*, vol. 53, no. 3, pp. 321–339, 2001.
- [2] M. A. Morales, P. V. Finotelli, J. A. H. Coaquira et al., “In situ synthesis and magnetic studies of iron oxide nanoparticles in calcium-alginate matrix for biomedical applications,” *Materials Science and Engineering C*, vol. 28, no. 2, pp. 253–257, 2008.
- [3] D. K. Kim, Y. Zhang, J. Kehr, T. Klason, B. Bjelke, and M. Muhammed, “Characterization and MRI study of surfactant-coated superparamagnetic nanoparticles administered into the rat brain,” *Journal of Magnetism and Magnetic Materials*, vol. 225, no. 1-2, pp. 256–261, 2001.
- [4] C. H. Reynolds, N. Annan, K. Beshah et al., “Gadolinium-loaded nanoparticles: new contrast agents for magnetic resonance imaging,” *Journal of the American Chemical Society*, vol. 122, no. 37, pp. 8940–8945, 2000.
- [5] A. S. Lübbe, C. Bergemann, H. Riess et al., “Clinical experiences with magnetic drug targeting: a phase I study with 4'-epidoxorubicin in 14 patients with advanced solid tumors,” *Cancer Research*, vol. 56, no. 20, pp. 4686–4693, 1996.
- [6] C. Bergemann, D. Müller-Schulte, J. Oster, L. A Brassard, and A. S. Lübbe, “Magnetic ion-exchange nano- and microparticles for medical, biochemical and molecular biological applications,” *Journal of Magnetism and Magnetic Materials*, vol. 194, no. 1, pp. 45–52, 1999.
- [7] D. C. F. Chan, D. B. Kirpotin, and J. P. A. Bunn, “Synthesis and evaluation of colloidal magnetic iron oxides for the site-specific radiofrequency-induced hyperthermia of cancer,” *Journal of Magnetism and Magnetic Materials*, vol. 122, no. 1–3, pp. 374–378, 1993.
- [8] A. Jordan, R. Scholz, P. Wust et al., “Endocytosis of dextran and silan-coated magnetite nanoparticles and the effect of intracellular hyperthermia on human mammary carcinoma cells in vitro,” *Journal of Magnetism and Magnetic Materials*, vol. 194, no. 1, pp. 185–196, 1999.
- [9] A. Dyal, K. Loos, M. Noto et al., “Activity of *Candida rugosa* lipase immobilized on  $\gamma\text{-Fe}_2\text{O}_3$  magnetic nanoparticles,” *Journal of the American Chemical Society*, vol. 125, no. 7, pp. 1684–1685, 2003.
- [10] R. Weissleder, G. Elizondo, J. Wittenberg, C. A. Rabito, H. H. Bengele, and L. Josephson, “Ultrasmall superparamagnetic iron oxide: characterization of a new class of contrast agents for MR imaging,” *Radiology*, vol. 175, no. 2, pp. 489–493, 1990.
- [11] K. Thode, M. Lück, W. Schröder et al., “The influence of the sample preparation on plasma protein adsorption patterns on polysaccharide-stabilized iron oxide particles and N-terminal microsequencing of unknown proteins,” *Journal of Drug Targeting*, vol. 5, no. 1, pp. 35–43, 1997.
- [12] T. Y. Liu, S. H. Hu, K. H. Liu, D. M. Liu, and S. Y. Chen, “Preparation and characterization of smart magnetic hydrogels and its use for drug release,” *Journal of Magnetism and Magnetic Materials*, vol. 304, no. 1, pp. e397–e399, 2006.
- [13] S. L. McGill, C. L. Cuylear, N. L. Adolphi, M. Osiński, and H. D. C. Smyth, “Magnetically responsive nanoparticles for drug delivery applications using low magnetic field strengths,” *IEEE Transactions on Nanobioscience*, vol. 8, no. 1, Article ID 4801978, pp. 33–42, 2009.
- [14] T. E. Jørgensen, M. Sletmoen, K. I. Draget, and B. T. Stokke, “Influence of oligoguluronates on alginate gelation, kinetics, and polymer organization,” *Biomacromolecules*, vol. 8, no. 8, pp. 2388–2397, 2007.
- [15] E. R. Morris, D. A. Rees, D. Thom, and J. Boyd, “Chiroptical and stoichiometric evidence of a specific, primary dimerisation process in alginate gelation,” *Carbohydrate Research*, vol. 66, no. 1, pp. 145–154, 1978.
- [16] G. T. Grant, E. R. Morris, and D. A. Rees, “Biological interactions between polysaccharides and divalent cations: the egg box model,” *FEBS Letters*, vol. 32, no. 1, pp. 195–198, 1973.
- [17] N. V. Majeti and R. Kumar, “A review of chitin and chitosan applications,” *Reactive and Functional Polymers*, vol. 46, no. 1, pp. 1–27, 2000.

- [18] Y. Ohya, R. Cai, H. Nishizawa, K. Hara, and T. Ouchi, “Preparation of PEG-grafted chitosan nanoparticles as peptide drug carriers,” *S.T.P. Pharma Sciences*, vol. 10, no. 1, pp. 77–82, 2000.
- [19] P. Opanasopit, T. Ngawhirunpat, T. Rojanarata, C. Choochot-tiros, and S. Chirachanchai, “N-Phthaloylchitosan-g-mPEG design for all-trans retinoic acid-loaded polymeric micelles,” *European Journal of Pharmaceutical Sciences*, vol. 30, no. 5, pp. 424–431, 2007.
- [20] C. Prego, D. Torres, E. Fernandez-Megia, R. Novoa-Carballal, E. Quiñoá, and M. J. Alonso, “Chitosan-PEG nanocapsules as new carriers for oral peptide delivery: effect of chitosan pegylation degree,” *Journal of Controlled Release*, vol. 111, no. 3, pp. 299–308, 2006.
- [21] Z. Yao, C. Zhang, Q. Ping, and L. Yu, “A series of novel chitosan derivatives: synthesis, characterization and micellar solubilization of paclitaxel,” *Carbohydrate Polymers*, vol. 68, no. 4, pp. 781–792, 2007.
- [22] X. Zhang, H. Zhang, Z. Wu, Z. Wang, H. Niu, and C. Li, “Nasal absorption enhancement of insulin using PEG-grafted chitosan nanoparticles,” *European Journal of Pharmaceutics and Biopharmaceutics*, vol. 68, no. 3, pp. 526–534, 2008.
- [23] A. Haug, B. Larsen, and O. Smidsrød, “A study of the constitution of alginic acid by partial acid hydrolysis,” *Acta Chemica Scandinavica*, vol. 20, pp. 183–190, 1966.
- [24] A. Haug, B. Larsen, and O. Smidsrød, “Uronic acid sequence in alginate from different sources,” *Carbohydrate Research*, vol. 32, no. 2, pp. 217–225, 1974.
- [25] I. M. El-Sherbiny, S. McGill, and H. D. C. Smyth, “Swellable microparticles as carriers for sustained pulmonary drug delivery,” *Journal of Pharmaceutical Sciences*, vol. 99, no. 5, pp. 2343–2356, 2010.
- [26] L. S. Guinesi and E. T. G. Cavalheiro, “The use of DSC curves to determine the acetylation degree of chitin/chitosan samples,” *Thermochimica Acta*, vol. 444, no. 2, pp. 128–133, 2006.
- [27] F. S. Kittur, K. V. H. Prashanth, K. Udaya Sankar, and R. N. Tharanathan, “Characterization of chitin, chitosan and their carboxymethyl derivatives by differential scanning calorimetry,” *Carbohydrate Polymers*, vol. 49, no. 2, pp. 185–193, 2002.
- [28] M. L. Dheu-Andries and S. Pérez, “Geometrical features of calcium-carbohydrate interactions,” *Carbohydrate Research*, vol. 124, no. 2, pp. 324–332, 1983.
- [29] C. A. Steginsky, J. M. Beale, H. G. Floss, and R. M. Mayer, “Structural determination of alginic acid and the effects of calcium binding as determined by high-field n.m.r,” *Carbohydrate Research*, vol. 225, no. 1, pp. 11–26, 1992.

## Research Article

# Pilot Study of Inhaled Aerosols Targeted via Magnetic Alignment of High Aspect Ratio Particles in Rabbits

Gillian E. S. Redman,<sup>1</sup> Andrew R. Martin,<sup>1,2</sup> Paul Waszak,<sup>3</sup> Richard B. Thompson,<sup>4</sup> Po-Yin Cheung,<sup>3</sup> Bernard Thébaud,<sup>3</sup> and Warren H. Finlay<sup>1</sup>

<sup>1</sup>Department of Mechanical Engineering, University of Alberta, Edmonton, Canada T6G 2G8

<sup>2</sup>Air Liquide Centre de Recherche Claude-Delorme, 78354, Les Loges-en-Josas, France

<sup>3</sup>Department of Pediatrics, Faculty of Medicine and Dentistry, University of Alberta, Edmonton, Canada T6G 2S2

<sup>4</sup>Department of Biomedical Engineering, University of Alberta, Edmonton, Canada T6G 2V2

Correspondence should be addressed to Gillian E. S. Redman, gillian.redman@gmail.com

Received 17 August 2010; Accepted 5 October 2010

Academic Editor: Xingmao Jiang

Copyright © 2011 Gillian E. S. Redman et al. This is an open access article distributed under the Creative Commons Attribution License, which permits unrestricted use, distribution, and reproduction in any medium, provided the original work is properly cited.

Recently, inhaled pharmaceutical aerosols have seen increased investigation in the treatment of lung cancer, where the inability to deliver adequate therapeutic drug concentrations to tumour sites may be overcome with improved targeted delivery to the site of the tumour. In this study, the feasibility of magnetically targeted delivery of high aspect ratio particles loaded with iron oxide nanoparticles was studied in 19 New Zealand White rabbits. Half of the exposed rabbits had a magnetic field placed externally over their right lung. Iron sensitive magnetic resonance images of the lungs were acquired to determine the iron concentrations in the right and left lung of each animal. The right/left ratio increased in the middle and basal regions of the lung where, due to the morphology of the rabbit lung, this method of targeting is most effective. With further optimization, this technique could be an effective method for increasing the dose of drug delivered to a specific site within the lung.

## 1. Introduction

Pharmaceutical aerosols remain a growing field of interest in developing new methods of delivering therapeutic agents to the body. The large surface area of the lung offers excellent possibilities as a portal for fast and efficient drug delivery. Local drug delivery to the lung is common for the treatment of diseases such as asthma and chronic pulmonary infections. More recently, inhaled pharmaceuticals have attracted increased interest for the treatment of lung cancer [1–3]. One of the major obstacles in the treatment of lung cancer is the inability to deliver adequate therapeutic drug concentrations to the site of the tumour [1]. The use of inhaled chemotherapy in the treatment of lung cancer attempts to overcome this problem. Drug concentrations in the lung can be greatly increased without causing systemic toxicity, which results in greater drug concentrations at the site of interest and a decrease in the systemic side

effects experienced by the patient [3]. The cytotoxic effect of the drug may result from direct topical application to the tumour, as well as absorption of the drug into the bronchial circulation which supplies blood to the tumour. In addition, tumours will often locally destroy the bronchial cilia, which in the case of aerosol delivery aids in retaining the drug at the desired site over a longer period of time [2]. However, these benefits could be further increased by better targeting delivery locally within the lung to the site of the tumour.

Indeed, there are a variety of methods to target a selected range of generations within the lung, including optimizing the particle density or size, or varying the inhalation flow rate [4–6]. However, these techniques are not able to target specific physical locations within the lung, which would be of interest for treatment of a disease such as lung cancer where often only one lobe of the lung is affected. Over recent years, there have been several different approaches to site-specific targeted drug delivery. One of these methods utilizes

an intratracheal nebulizing catheter to aerosolize the drug inside the targeted lobe or lung. Although this method has been shown to be effective in dogs, it is an invasive procedure with additional health risks associated with intubation of the subject [7]. In contrast, Dames et al. [8] have investigated a noninvasive method of magnetically targeted drug delivery in mice through the use of nebulized droplets containing superparamagnetic iron oxide nanoparticles. They found an increase in deposition of 7.9 times with the tip of an electromagnet centered 1mm above the surgically exposed right lobe of the lung. Although this is a promising result, several complications could arise in attempting to apply this procedure for humans. Importantly, when moving the magnet tip to 5 mm away from the target site, the magnetic flux decreased by approximately 90% [8]. Study into the design of magnetic fields for the purpose of magnetic drug targeting have shown that it remains feasible for superficial sites, but the rapid reduction in magnetic flux with distance from the source makes it a difficult method for targeting tissues deeper in the body without the use of surgically implanted ferromagnetic stents [9]. An alternative noninvasive approach to magnetic targeting in the lung is to utilize high aspect ratio particles (HARPs) in conjunction with superparamagnetic nanoparticles to target specific areas within the lung by controlling particle orientation with the use of a magnetic field [10–12].

The probability of deposition of HARPs is highly dependent on their orientation as they travel through the airways. HARPs will tend to align with their long axis parallel to the direction of flow, as seen in Figure 1(a), for which the probability of deposition is at its lowest [13]. As the tracheobronchial region transitions into the alveolar region, the dominant mechanism of deposition becomes interception, which occurs when the particle tip collides with the airway wall while the center of mass of the particle remains on a streamline. Airways are oriented in a random fashion within the lung. By aligning the HARPs in one direction, the particles would become randomly oriented with respect to the direction of flow in the airways, leading to a higher probability of deposition [14]. By loading HARPs with superparamagnetic nanoparticles, a preferred axis of magnetization is created along the length of the particle [10]. By placing a select region of the lung in a magnetic field, the orientation of the particles can be controlled by using the magnetic torque to align the long axis of the particles in the direction of the field, as seen in Figure 1(b). Martin and Finlay investigated the feasibility of this technique and found that the magnetic torque exerted on the particle was enough to overcome the shear forces of fluid flow in the lung for the range of particle aspect ratios of interest [10].

Using an airway model representative of the terminal bronchioles of the lung, Martin and Finlay showed an increase in deposition of cromoglycic acid (CA) HARPs of approximately 1.7 times with the application of a magnetic field compared to without [11]. The HARPs with and without magnetite had VMDs of 0.47 and 0.32  $\mu\text{m}$ , respectively, and VMLs of 3.0 and 2.0  $\mu\text{m}$ , respectively. Although (CA) is not intended for cancer therapy, it was chosen as a model drug, as it forms acicular crystals. The anticancer drug

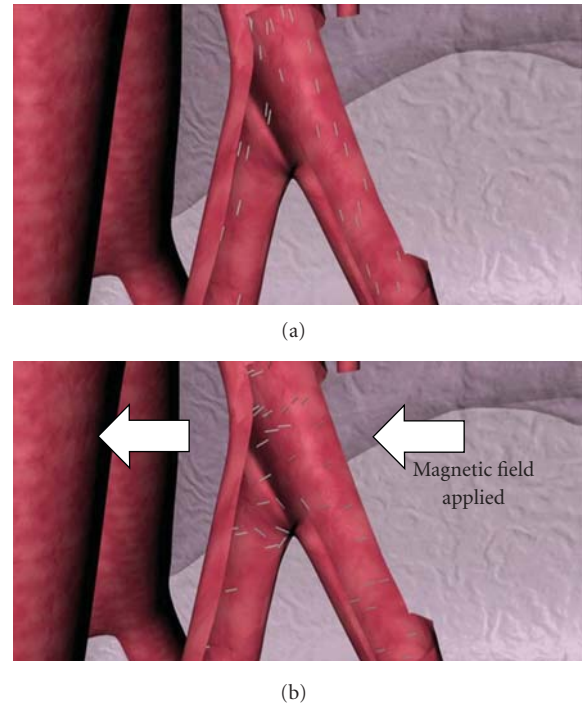


FIGURE 1: Alignment of HARPs in the lung (a) naturally (b) in the presence of a magnetic field.

paclitaxel has been loaded onto HARPs and shown to be more effective at shrinking tumours in this shape [15]. To further strengthen this positive result and the feasibility of this technique of magnetic targeting in the lung, an *in vivo* study was completed, as described herein. In the present study, New Zealand white rabbits were selected to determine the increase in aerosol deposition in a lung targeted with the application of a magnetic field. The use of laboratory animals for the study of inhaled particle deposition is common, as the total and regional particle deposition is qualitatively similar to humans [16]. The iron oxide nanoparticles also functioned as a magnetic resonance imaging (MRI) contrast agent, allowing the signal intensity of the images to be related to the concentration of iron [17]. This data was then used to calculate iron concentrations in the lungs of targeted and nontargeted rabbits, which were compared to show regional differences in deposition [18].

## 2. Methods

**2.1. Aerosol Production.** HARPs of cromoglycic acid (CA) were prepared following the crystallization method of Chan and Gonda [19] using cromolyn sodium salt purchased from Sigma-Aldrich Canada (Oakville, ON). To create one dose of suspension for nebulization, 10 mg of CA was combined with 150  $\mu\text{L}$  of colloidal super paramagnetic iron oxide, FeREX (BioPAL, Worcester, MA), and 5 mL of deionized water. The FeREX had a concentration of 10 mg Fe/ml. Dried CA particles and FeREX were dispersed by pipette to form an aqueous suspension prior to nebulization. These suspensions

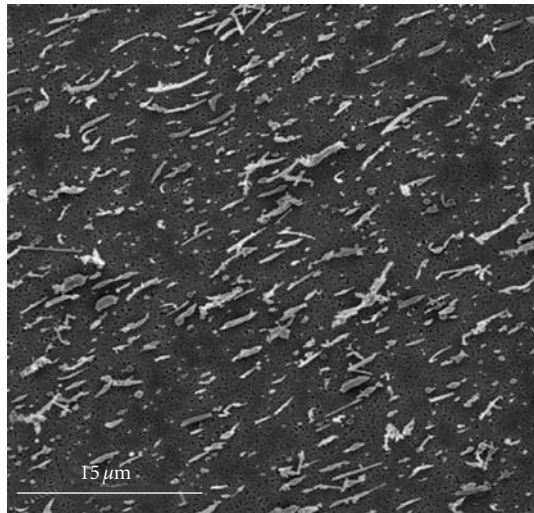


FIGURE 2: SEM image of high aspect ratio particles (HARPs) of CA and FeREX. The light-coloured aligned particles are the HARPs, and the small black dots are the pores of the membrane.

were nebulized using a clinically marketed vibrating mesh nebulizer (Aeroneb Pro; Aerogen, Galway, Ireland) and subsequently dried using a diffusion dryer containing silica gel (Component of Model 3475 Monodisperse Aerosol Generator; TSI, Shoreview, MN). This resulted in HARPs, similar to those previously created for an in vitro study, with diameters on the order of 500 nanometers and lengths varying from 1 to 10 micrometers [11]. The FeREX particles were specified to be in the range of 50–150 nm by the manufacturer. An SEM image taken of the HARPs generated can be seen in Figure 2. These HARPs were collected on a 0.2  $\mu\text{m}$  polycarbonate membrane (Isopore GTTP04700; Millipore, Billerica, MA) with a magnetic field produced across the face of the membrane to demonstrate alignment.

In order to ensure that regional lung distributions of iron are representative of regional distributions of CA throughout the lung, the distribution of iron across the range of HARP sizes was examined. This was done by drawing aerosol from the nebulizer and diffusion dryer through a cascade impactor (Mark II Andersen Impactor; Thermo Andersen, Smyrna, GA) at 28.3 l/min. UV spectrophotometry was used to determine the masses of CA and iron deposited on each stage of the impactor. The mass of CA was found by washing with 0.01 N sodium hydroxide and assaying by UV spectrophotometry at a wavelength of 326 nm. The mass of the iron was determined by methods similar to those described previously by Suwa et al. [20]. Prior to spectrophotometry at 468 nm, the water insoluble FeREX was transformed to soluble  $\text{Fe}^{3+}$  using concentrated hydrochloric acid, and the CA was removed from suspension with the use of a 0.8  $\mu\text{m}$  filter.

**2.2. Animals.** This study involved 19 male New Zealand White Rabbits with weights ranging from 3.4 to 4.5 kg. The animals were housed under conventional conditions under the guidelines of the Canadian Council on Animal Care

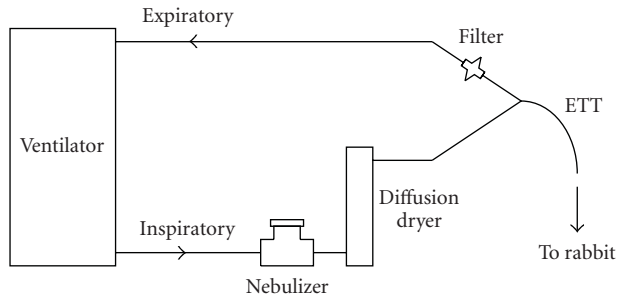


FIGURE 3: Schematic of mechanical ventilation circuit used to expose rabbits to aerosol. ETT: endotracheal tube.

for one week prior to the study. All animal procedures were approved by the University of Alberta Health Sciences Animal Policy and Welfare Committee.

**2.3. Exposure.** The nebulizer and diffusion dryer were added to the inspiratory line of a mechanical ventilation circuit (InfantStar; Infrasonics Inc., San Diego, CA) to deliver the aerosol to the lungs of ventilated rabbits. This circuit is outlined below in Figure 3 where the rabbit lung is ventilated via a 3.5 mm endotracheal tube. All excess aerosol (not deposited in the respiratory system of the rabbit) was collected on a filter (Respirgard; Vital Signs, Totowa, NJ) in the expiratory line. After the animals were anesthetized using intravenous ketamine and xylazine infusions, a tracheostomy was performed, and a 3.5 mm endotracheal tube was inserted, connecting the rabbit to the mechanical ventilation circuit. The animals were then paralyzed using a pancuronium (0.2 mg/kg) intravenous infusion. All drug infusions were repeated as needed. Mechanical ventilation was performed using 100% oxygen with a peak inspiratory pressure of 14 cm  $\text{H}_2\text{O}$ , a positive end-expiratory pressure of 2 cm  $\text{H}_2\text{O}$ , a continuous flow of 6 l/min, and an inspiratory time of 0.5 s. The oxygen was neither warmed nor humidified prior to inspiration. Blood gases were monitored at interval throughout ventilation by arterial blood sampling and analyzed by ABL500 (Radiometer, Copenhagen, Denmark). To maintain an arterial  $\text{PCO}_2$  between  $40 \pm 5$  mm Hg, the breath frequency was adjusted between 20 and 25 breaths/min.

The animals were separated into three different categories of exposure: (1) no aerosol delivered, (2) aerosol delivered with no magnetic field applied, and (3) aerosol delivered with the application of a magnetic field. Three rabbits were mechanically ventilated for approximately 30 minutes but were not exposed to aerosol. Eight rabbits were exposed to two doses of the aerosol described above. Upon the completion of nebulization of the first dose, the reservoir in the nebulizer was refilled without opening the breathing circuit, and the second dose then ran to completion. The final eight rabbits were exposed to the aerosol but additionally had a magnetic field applied over the right lung. This was accomplished with the use of neodymium permanent magnets (two stacks of three, 2"  $\times$  2"  $\times$  0.5" magnets; Indigo Instruments Waterloo, ON). The two stacks of magnets were separated by 20 cm and positioned above and below the

rabbit to create a field strength and gradient which decreased from approximately 35 mT and 1.5 T/m, respectively, at the posterior side of the right lung to 20 mT and 0.1 T/m at the anterior side. In this position, magnetic field lines ran parallel to the direction of gravity, and the field gradient was directed so that small translational magnetic forces acting on particles augmented, rather than subtracted from, the force of gravity.

For all exposed rabbits ventilation lasted on average for approximately 45 minutes, with aerosol produced on average for approximately 23 minutes. All rabbits were euthanized with a pentobarbital intravenous infusion upon the completion of ventilation. The time between death and MRI scan was between 40 and 70 minutes for all rabbits.

**2.4. Measurement of Deposition.** MRI measurements were performed using a Siemens Sonata 1.5 T, 60 cm bore system (Siemens Medical Systems, Erlangen, Germany). Each rabbit was oriented in the prone position, in a 16 cm diameter volume birdcage coil, with the lungs placed at the centre of the coil to maximize reception sensitivity and uniformity. Iron oxide functions as an MRI contrast agent [17] which allows the signal intensity of the images to be related to the iron concentration. Specifically, the  $T_1$  relaxation time, which describes the rate of recovery of the magnetization to thermal equilibrium, is directly related to the iron concentration according to the following relationship [20, 21]:

$$\frac{1}{T_1} = \frac{1}{T_{1,0}} + \alpha \cdot c, \quad (1)$$

where  $T_{1,0}$  is the baseline relaxation time (determined from the 3 baseline rabbits),  $c$  is the tissue concentration of iron, and  $\alpha$  is a constant specific to the contrast agent as determined from previous work [18].  $T_1$  and  $T_{1,0}$  values were calculated by inverting the MRI signal intensity and then fitting the magnitude of the recovered MRI signal intensity measured at increasing delays following the inversion preparation, as shown in

$$SI = \text{abs}\left[ SI_\infty \left( 1 - k \cdot e^{-T_i/T_1} \right) \right], \quad (2)$$

where  $SI$  is the signal intensity at inversion time  $T_i$ , and the constants  $SI_\infty$ ,  $k$ , and  $T_1$  were determined by nonlinear regression.

To acquire the  $SI$  values, an inversion recovery fast spin echo pulse sequence with either 8 or 11  $T_i$  times from 100 to 4000 ms, in addition to the case of no inversion, was used to map the longitudinal relaxation time within the lung. The image parameters were as follows: 108 × 25 mm field of view and a 448 × 105 matrix (in-plane spatial resolution interpolated to 250 × 250  $\mu\text{m}$ ). There were 24 2.5 mm thick axial slices taken in two serial experiments (to prevent cross-talk between neighboring slices) which spanned the lung from the apex to the diaphragm. The pulse sequence had a repetition time, TR, of 5120 ms and an echo time, TE, of 12 ms. The total acquisition time for each rabbit was approximately 30 minutes.

The images attained from the MRI scans were post-processed to map iron concentrations in the right and left

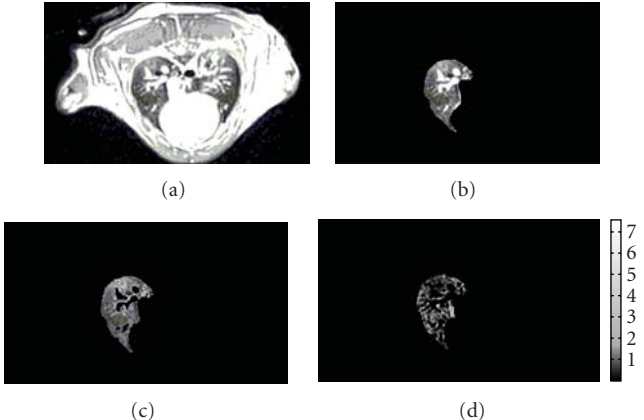


FIGURE 4: Sample of image processing: (a) original MRI image, (b) after selection of region of interest, (c) after removal of vasculature, and (d) iron concentrations in  $\mu\text{g}/\text{cm}^3$ .

lung for each rabbit. The lungs were manually segmented, and regions of high signal strength associated with lung vasculature were removed using a threshold filter as shown in Figure 4. A MATLAB (The Mathworks, Natick, MA) script was written to calculate the average  $T_1$  relaxation times for user-selected regions of interest within the right and left lungs, in apical, medial, and basal subregions.

Using the regionally calculated  $T_1$  and  $T_{1,0}$  values, the iron concentrations were then compared between the right and left lung for each rabbit, globally, and in the apical, medial, and basal subregions. On average 18 of the 24 2.5 mm axial slices spanned the lung from top to bottom, in which case each subregion was comprised of 6 slices.

### 3. Results

Aerosol drawn through the cascade impactor showed a reasonably even distribution of iron oxide over the size range of CA particles created, ensuring that regional lung distributions of iron were representative of regional distributions of CA. This can be seen below in Figure 5 where statistically significant differences in the iron and CA-weighted size distributions were only seen for the plates 1, 2, and 3.

For the three baseline rabbits an average  $T_{1,0}$  relaxation time of  $1531 \pm 45$  ms was measured. The average whole-lung  $T_1$  relaxation time and iron concentration for the sixteen exposed rabbits were 1211 ms and  $1.17 \pm 0.12 \mu\text{g}/\text{cm}^3$ , respectively. The  $T_1$  values and iron concentrations for both the left and right lungs of the exposed rabbits are shown in Table 1. The ratio of right to left lung iron concentration was  $1.09 \pm 0.07$  in the nontargeted rabbits and  $1.17 \pm 0.14$  in the targeted rabbits. Nontargeted refers to rabbits exposed without the application of a magnetic field, and targeted refers to those with a magnetic field applied over the right lung.

The regional apical, medial, and basal analyses are summarized in Figure 5. It can be seen in Figure 6 that with application of the magnetic field, deposition in the targeted lung is decreased in the apical region and increased

TABLE 1: Regional and total area-averaged  $T_1$  relaxation times and iron concentrations for the left and right lung of nontargeted and targeted rabbits.

Rabbit	Region	Left Lung		Right Lung		$[Fe]_R/[Fe]_L$
		$T_1$ [ms]	[Fe] [ $\mu\text{g}/\text{cm}^3$ ]	$T_1$ [ms]	[Fe] [ $\mu\text{g}/\text{cm}^3$ ]	
Nontargeted	Total	1206 $\pm$ 63	0.61 $\pm$ 0.28	1200 $\pm$ 60	0.64 $\pm$ 0.26	1.09
	Apex	1159 $\pm$ 29	0.84 $\pm$ 0.15	1140 $\pm$ 34	0.95 $\pm$ 0.18	1.22
	Middle	1210 $\pm$ 28	0.59 $\pm$ 0.13	1193 $\pm$ 24	0.67 $\pm$ 0.11	1.30
	Base	1205 $\pm$ 32	0.62 $\pm$ 0.14	1225 $\pm$ 26	0.52 $\pm$ 0.11	0.96
Targeted	Total	1224 $\pm$ 44	0.52 $\pm$ 0.20	1213 $\pm$ 42	0.57 $\pm$ 0.18	1.17
	Apex	1178 $\pm$ 20	0.73 $\pm$ 0.10	1182 $\pm$ 28	0.72 $\pm$ 0.13	0.94
	Middle	1233 $\pm$ 20	0.48 $\pm$ 0.09	1205 $\pm$ 18	0.60 $\pm$ 0.08	1.62
	Base	1216 $\pm$ 23	0.56 $\pm$ 0.11	1211 $\pm$ 19	0.58 $\pm$ 0.09	1.18

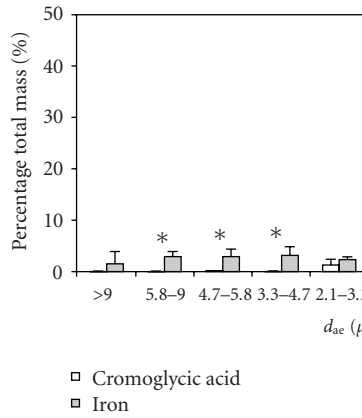


FIGURE 5: Aerodynamic diameter ( $d_{ae}$ ) size distributions weighted by mass of iron and mass of cromoglycic acid, as determined by cascade impaction for the iron oxide-loaded cromoglycic acid aerosol. Asterisks indicate statistically significant differences between the two distributions ( $P < .05$ ; two-tailed student's  $t$ -test for independent samples).

in the middle and basal regions. When comparing the iron concentration in the middle and base of the lung with the apex of the lung, it can be seen in Figure 7 that in the right lung of the targeted rabbits there is a targeted increase in deposition in the more basal regions.

#### 4. Discussion

With the right lung being targeted, an increase in the ratio of the right to left lung iron concentrations was expected. After postprocessing the images from the 19 rabbits, it was found that the ratio of right/left iron concentration of the untargeted rabbits was similar to that of the targeted rabbits, which were 1.09 and 1.17, respectively. However, examining the data in more detail, a larger increase in deposition in the middle and basal regions of the lung can be seen. In the middle region of the lung the ratio of right to left lung deposition increased from  $1.30 \pm 0.13$  to  $1.62 \pm 0.41$  and in the basal region deposition increased from  $0.96 \pm 0.16$  to  $1.18 \pm 0.17$ .

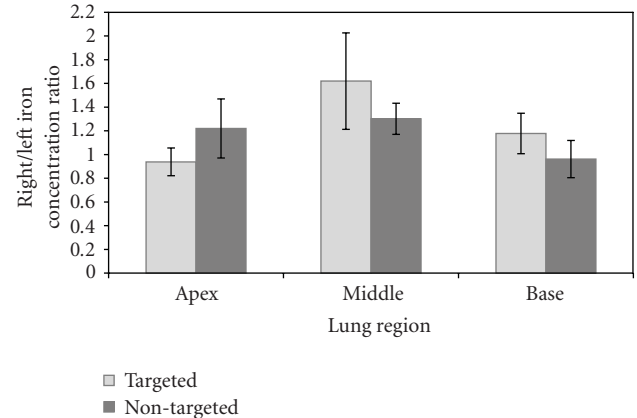


FIGURE 6: Ratios of regional right to left lung iron concentrations in targeted and nontargeted rabbits. Error bars represent standard errors of the mean.

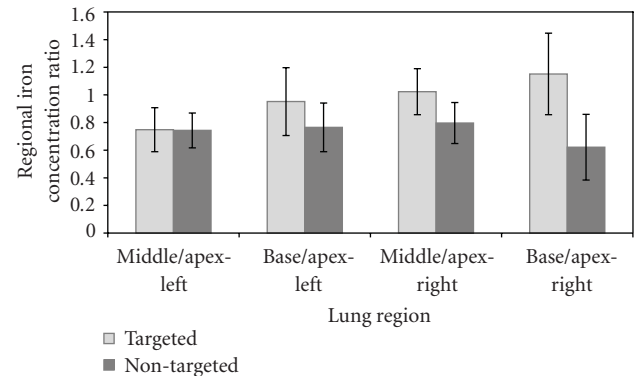


FIGURE 7: Ratios of iron concentration between middle and apical, and basal and apical regions of the left and right lungs of targeted and nontargeted rabbits. Error bars represent standard errors of the mean.

CA particles were loaded with iron oxide for the purpose of magnetic alignment, but also acted as an MRI contrast agent. As was seen in Figure 5, there were statistically significant differences in the iron and CA-weighted size distributions seen for plates 1, 2, and 3. However, this represents a small fraction of the overall mass and is likely

due to diffusional losses of iron oxide nanoparticles not associated with the larger CA particles.

Although laboratory animals are commonly used for aerosol deposition studies, rodents such as the rabbit have a different lung morphometry than humans. In humans the airways branch dichotomously, meaning each parent airway divides into two equal sized daughter airways. The lung of the rabbit exhibits monopodial branching where multiple smaller daughter airways can branch off a single, longer parent airway [22]. In dichotomous branching, the distance a particle must travel from the trachea to the alveoli is similar for all the lobes whereas these distances can vary significantly in monopodial branching. The shortest distances occur in the upper lobes, which can result in these lobes experiencing higher concentrations of inhaled material for longer periods of time [23]. Thus, in the upper lobes, particles have a longer exposure time, increasing deposition by settling due to gravity; this mechanism likely dominates the probability of deposition over interception. Therefore, it is possible that this would result in a minimal effect observed from alignment of the HARP<sub>s</sub> in the upper region of the lung. This hypothesis is further supported by the higher total iron concentrations in the apical region of the lung compared with the middle and basal regions. This is seen in Figure 7 where the ratios of middle/apex and base/apex for the right and left lungs are all less than one for the untargeted rabbits. Despite the decreased efficiency of targeting in the apex, the effect of targeting is seen in the middle and basal regions of the lung where interception is expected to have a larger impact on the probability of deposition. In the apical region, iron concentrations were decreased with the application of the magnetic field. The method used to divide the lungs into three regions was rather crude and may have resulted in some of the conducting airways of the apex being incorrectly classified as part of the middle region. Targeting is expected to increase deposition in these incorrectly classified conducting apical airways, decreasing the total aerosol that would continue for possible deposition into the apically classified region. This would result in a perceived decrease in deposition in the apical region. A more detailed and accurate method of separating the regions of the lung, similar to the computer models of lung morphology used in conjunction with single photon emission computed tomography (SPECT) images by Schroeter et al. [24], would provide valuable data regarding regional deposition.

It is important to note that these results were not statistically significant ( $P > .05$ ). For example, when performing an unpaired two-tailed student's *t*-test for independent samples on the data from Figure 7, the *P* values were found to be .98 and .55 in the middle and basal regions of the untargeted left lung, respectively. In the middle and basal regions of the targeted right lung, these *P* values were found to decrease to .33 and .18, respectively. Statistical significance could potentially be obtained by increasing the number of subjects. However, a more desirable solution would be to decrease variability in the experimental methodology by eliminating some of the limitations present in this study.

A number of these limitations are as follows.

Within the study group, consisting of 19 subjects, considerable intersubject variability existed. This variability, in conjunction with the small number of subjects, led to results which were not statistically significant, although the data shows promise. Specifically, the baseline relaxation time ( $T_{1,0}$ ) determined from the three baseline rabbits varied from 1249 to 1444 ms. This value, representing the properties of the lung tissue without the presence of iron, is critical in determining the iron concentration of the lungs in the exposed rabbits, and our use of an average baseline relaxation time, rather than subject specific times, limits the discriminating power of the present study. Specifically, iron concentrations were determined from variation in  $T_1$  times only as averages for each group; mapping of iron concentrations in individual rabbits would be possible only with individual  $T_{1,0}$  baselines values.

Additionally, the ventilator used in this study did not measure the inhalation tidal volumes, eliminating the possibility of determining the total deposition fraction. If the majority of the aerosol entering the respiratory system deposits without the presence of a magnetic field, any further increase in deposition with the application of a magnetic field is limited. The results of this limitation would be a decrease in observed effectiveness of the targeting.

In moving forward with this study, the limitations of intersubject variability could be overcome by increasing the number of subjects, obtaining individual baselines for each subject, or increasing the effectiveness of the targeting. By measuring the individual baseline relaxation time ( $T_{1,0}$ ) for each subject, a much more accurate estimate of iron concentration would be calculated in each animal. This would require an MRI scan to be taken of each subject before and after aerosol exposure, which would allow each rabbit to be its own baseline. Increasing the effectiveness of the targeting through optimization of the HARP<sub>s</sub> could further help in overcoming intersubject variability. The probability of deposition with the application of the magnetic field will be increased by increasing the length of the HARP<sub>s</sub>. Alignment of longer particles with an external magnetic field would further increase interception with the airway walls [11].

## 5. Conclusion

This pilot study showed an increase in deposition of high aspect ratio particles (HARP<sub>s</sub>) of cromoglycic acid (CA) loaded with iron oxide nanoparticles with the application of a magnetic field in the middle and basal regions of the lung. As interception is not the dominant mechanism of particle deposition in the apex of rabbits, minimal effect was seen in the apical region. Further work must be done to decrease the effect of the intersubject variability through the use of individual baseline relaxation times ( $T_{1,0}$ ) and optimized HARP lengths to yield results that will be statistically significant. With further optimization of this technique, and the delivery system, it may be an effective method for the treatment of diseases such as lung cancer by increasing the dose of drug delivered to a specific site within the lung.

## Acknowledgments

This paper was funded in part by an NSERC Special Research Opportunity grant. Kelvin Chow is gratefully acknowledged for supplying the MATLAB script to filter out vasculature.

## References

- [1] G. A. Otterson, M. A. Villalona-Calero, S. Sharma et al., "Phase I study of inhaled doxorubicin for patients with metastatic tumors to the lungs," *Clinical Cancer Research*, vol. 13, no. 4, pp. 1246–1252, 2007.
- [2] T. Tatsumura, S. Koyama, M. Tsujimoto, M. Kitagawa, and S. Kagamimori, "Further study of nebulisation chemotherapy, a new chemotherapeutic method in the treatment of lung carcinomas: fundamental and clinical," *British Journal of Cancer*, vol. 68, no. 6, pp. 1146–1149, 1993.
- [3] S. Sharma, D. White, A. R. Imondi, M. E. Placke, and D. M. Vail, "Development of inhalational agents for oncologic use," *Journal of Clinical Oncology*, vol. 19, no. 6, pp. 1839–1847, 2001.
- [4] W. H. Finlay, *The Mechanics of Inhaled Pharmaceutical Aerosols: An Introduction*, Academic Press, London, UK, 2001.
- [5] D. A. Edwards, J. Hanes, G. Caponetti et al., "Large porous particles for pulmonary drug delivery," *Science*, vol. 276, no. 5320, pp. 1868–1871, 1997.
- [6] P. Camner, M. Anderson, K. Philipson et al., "Human bronchiolar deposition and retention of 6-, 8-, and 10- $\mu\text{m}$  particles," *Experimental Lung Research*, vol. 23, no. 6, pp. 517–535, 1997.
- [7] K. Selting, J. C. Waldrep, C. Reinero et al., "Feasibility and safety of targeted cisplatin delivery to a select lung lobe in dogs via the AeroProbe intracorporeal nebulization catheter," *Journal of Aerosol Medicine and Pulmonary Drug Delivery*, vol. 21, no. 3, pp. 255–268, 2008.
- [8] P. Dames, B. Gleich, A. Flemmer et al., "Targeted delivery of magnetic aerosol droplets to the lung," *Nature Nanotechnology*, vol. 2, no. 8, pp. 495–499, 2007.
- [9] B. Gleich, N. Hellwig, H. Bridell et al., "Design and evaluation of magnetic fields for nanoparticle drug targeting in cancer," *IEEE Transactions on Nanotechnology*, vol. 6, no. 2, pp. 164–169, 2007.
- [10] A. R. Martin and W. H. Finlay, "Magnetic alignment of aerosol particles for targeted pulmonary drug delivery: comparison of magnetic and aerodynamic torques," *Journal of Computational and Theoretical Nanoscience*, vol. 5, no. 10, pp. 2067–2070, 2008.
- [11] A. R. Martin and W. H. Finlay, "Enhanced deposition of high aspect ratio aerosols in small airway bifurcations using magnetic field alignment," *Journal of Aerosol Science*, vol. 39, no. 8, pp. 679–690, 2008.
- [12] A. R. Martin and W. H. Finlay, "Alignment of magnetite-loaded high aspect ratio aerosol drug particles with magnetic fields," *Aerosol Science and Technology*, vol. 42, pp. 295–298, 2008.
- [13] T. Myojo, "Deposition of fibrous aerosol in model bifurcating tubes," *Journal of Aerosol Science*, vol. 18, no. 3, pp. 337–347, 1987.
- [14] I. Báláshazy, T. B. Martonen, and W. Hofmann, "Fiber deposition in airway bifurcations," *Journal of Aerosol Medicine*, vol. 3, pp. 243–260, 1990.
- [15] Y. Geng, P. Dalhaimer, S. Cai et al., "Shape effects of filaments versus spherical particles in flow and drug delivery," *Nature Nanotechnology*, vol. 2, no. 4, pp. 249–255, 2007.
- [16] R. F. Phalen, M. J. Oldham, and R. K. Wolff, "The relevance of animal models for aerosol studies," *Journal of Aerosol Medicine and Pulmonary Drug Delivery*, vol. 21, no. 1, pp. 113–124, 2008.
- [17] M.-F. Bellin, "MR contrast agents, the old and the new," *European Journal of Radiology*, vol. 60, no. 3, pp. 314–323, 2006.
- [18] A. R. Martin, R. B. Thompson, and W. H. Finlay, "MRI measurement of regional lung deposition in mice exposed nose-only to nebulized superparamagnetic iron oxide nanoparticles," *Journal of Aerosol Medicine and Pulmonary Drug Delivery*, vol. 21, no. 4, pp. 335–341, 2008.
- [19] H.-K. Chan and I. Gonda, "Aerodynamic properties of elongated particles of cromoglycic acid," *Journal of Aerosol Science*, vol. 20, no. 2, pp. 157–168, 1989.
- [20] T. Suwa, S. Ozawa, M. Ueda, N. Ando, and M. Kitajima, "Magnetic resonance imaging of esophageal squamous cell carcinoma using magnetite particles coated with anti-epidermal growth factor receptor antibody," *International Journal of Cancer*, vol. 75, no. 4, pp. 626–634, 1998.
- [21] S. Gohr-Rosenthal, H. Schmitt-Willich, W. Ebert, and J. Conrad, "The demonstration of human tumors on nude mice using gadolinium-labelled monoclonal antibodies for magnetic resonance imaging," *Investigative Radiology*, vol. 28, no. 9, pp. 789–795, 1993.
- [22] R. B. Schlesinger and L. A. McFadden, "Comparative morphometry of the upper bronchial tree in six mammalian species," *Anatomical Record*, vol. 199, no. 1, pp. 99–108, 1981.
- [23] F. J. Miller, R. R. Mercer, and J. D. Crapo, "Lower respiratory tract structure of laboratory animals and humans: dosimetry implications," *Aerosol Science and Technology*, vol. 18, no. 3, pp. 257–271, 1993.
- [24] J. D. Schroeter, J. S. Fleming, D. Hwang, and T. B. Martonen, "A computer model of lung morphology to analyze SPECT images," *Computerized Medical Imaging and Graphics*, vol. 26, no. 4, pp. 237–246, 2002.

## Review Article

# Facilitating Effects of Nanoparticles/Materials on Sensitive Immune-Related Lung Disorders

Ken-ichiro Inoue<sup>1</sup> and Hirohisa Takano<sup>2</sup>

<sup>1</sup>Department of Public Health and Molecular Toxicology, School of Pharmacy Sciences, Kitasato University, 5-9-1 Shirokane, Minato-ku, Tokyo 108-8641, Japan

<sup>2</sup>Environmental Health Sciences Division, National Institute for Environmental Studies, Tsukuba, Ibaraki 305-8506, Japan

Correspondence should be addressed to Ken-ichiro Inoue, inouek@pharm.kitasato-u.ac.jp

Received 8 June 2010; Accepted 5 July 2010

Academic Editor: Hugh D. Smyth

Copyright © 2011 K.-i. Inoue and H. Takano. This is an open access article distributed under the Creative Commons Attribution License, which permits unrestricted use, distribution, and reproduction in any medium, provided the original work is properly cited.

Although the adverse health effects of nanoparticles/materials have been proposed and are being clarified, their facilitating effects on preexisting pathological conditions have not been fully examined. In this paper, we provide insights into the immunotoxicity of nanoparticles/materials as an aggravating factor in hypersusceptible subjects, especially those with immune-related respiratory disorders using our *in vivo* experimental model. We first exhibit the effects of nanoparticles/materials on lung inflammation induced by bacterial endotoxin (lipopolysaccharide: LPS) *in vivo* as a disease model in innate immunity, and demonstrated that nanoparticles instilled through both an intratracheal tube and an inhalation system can exacerbate the lung inflammation. Secondly, we introduce the effects of nanoparticles/materials on allergic asthma *in vivo* as a disease model in adaptive immunity, and showed that repetitive pulmonary exposure to nanoparticles has aggravating effects on allergic airway inflammation, including adjuvant effects on Th2-milieu. Taken together, nanoparticle exposure may synergistically facilitate pathological inflammatory conditions in the lung via both innate and adaptive immunological abnormalities.

## 1. Introduction

Epidemiological studies have demonstrated a correlation between exposure to air pollutant particles at the concentrations currently found in major metropolitan areas and mortality and morbidity [1]. The concentration of particulate matter (PM) with a mass median aerodynamic diameter (a density-dependent unit of measure used to describe the diameter of the particle)  $\leq 2.5 \mu\text{m}$  (PM<sub>2.5</sub>) is more closely associated with both acute and chronic respiratory effects and subsequent mortality than larger particles of  $\leq 10 \mu\text{m}$  (PM<sub>10</sub>) [2]. In addition, one intriguing aspect of the epidemiologic data is that health effects of PM<sub>2.5</sub> are primarily seen in subjects with predisposing factors, including pneumonia, asthma, chronic obstructive pulmonary disease, compromised immune systems, atherosclerosis, age over 65 years old, and maybe depressive states [3–6]. Partially consistent with the epidemiological studies, we and others have experimentally demonstrated

that diesel exhaust particles (DEP), major contributors to environmental PM<sub>2.5</sub> in urban areas, exhibit respiratory toxicity with or without predisposing pathologies including allergic asthma, pulmonary emphysema, and acute renal failure *in vivo* [7–15].

To date, nanoparticles, particles less than  $0.1 \mu\text{m}$  in mass median aerodynamic diameter, have been shown to be increasing in ambient air [16]. Recent measurements indicate that nanoparticle numbers in ambient air range from  $2 \times 10^4/\text{cm}^3$  to  $2 \times 10^5/\text{cm}^3$ , with mass concentrations of more than  $50 \mu\text{g}/\text{m}^3$  near major highways [17, 18]. Also, nanoparticles have been implicated in cardiopulmonary system effects [19]. Furthermore, compared to larger particles, nanoparticles have a higher deposition rate in the peripheral lung, can cross the pulmonary epithelium, reach the interstitium [20], and may thus be systemically distributed in the bloodstream [21]. Nanoparticles have an enhanced capacity to produce reactive oxygen species, and consequently have a widespread toxicity [22–24].

Further, nanotechnology is now advancing at such an incredible pace that it has created an alternative industrial revolution over the past few years [25]. Consistent with this, the use of engineered nanomaterials has been rapidly increasing in commercial applications. As these materials have become more widespread, many questions have arisen regarding the adverse effects they may have on the environment as alternative inhalable toxicants. Due to their sizes, characteristics, and/or existing pattern, nanoparticles/materials have been implicated in cardiopulmonary system effects [19]. Compared to larger particles, nanoparticles have a higher deposition rate in the peripheral lung, can cross the pulmonary epithelium reach the interstitium [20], and, furthermore, may be systemically distributed in the bloodstream [21]. Furthermore, nanoparticles have an enhanced capacity to produce reactive oxygen species, and, consequently, have a widespread toxicity [22–24]. Nanoparticle exposure also reportedly influences cardiopulmonary systems in the presence or absence of predisposing diseases in human studies [26, 27]. However, biological evidence concerning the promoting effects of nanoparticles/materials on predisposing subjects has been less studied. Besides their toxic effects on health, therefore, it should be experimentally ascertained whether they also aggravate preexisting pathological conditions, and their underlying mechanisms should be resolved. In this paper, therefore, we will discuss the impact of nanoparticles/materials as immunological enhancers.

## **2. Effects of Nanoparticles on Acute Lung Inflammation Induced by Bacterial Endotoxin**

A glycolipid of gram-negative bacteria, known as endotoxin or lipopolysaccharide (LPS), stimulates host cells via innate immunity [28]. In animal models, intratracheal administration of LPS causes lung cytokine expression, neutrophil recruitment, and lung injury [29]. LPS is found in bronchoalveolar lavage (BAL) fluid of patients with pneumonia [30] and acute respiratory distress syndrome [31], which sometimes results in a fatal outcome. In addition, LPS is a significant constituent of many air pollutant particles and has accordingly been implicated in the adverse effects of PM [32]. In accordance with the close links among LPS, lung inflammation (injury), and PM, we have previously shown that intratracheal administration of DEPs and their components facilitates lung inflammation induced by LPS [13, 33] and subsequent systemic inflammation with coagulatory impairment [14].

We next examined the effects of pulmonary exposure to nanoparticles on lung inflammation related to LPS in mice. Vehicle, two sizes (14 and 56 nm) of carbon black nanoparticles, LPS, or LPS + nanoparticles was administered intratracheally, and parameters of lung inflammation and coagulation were evaluated. Nanoparticles alone induced slight lung inflammation and significant pulmonary edema as compared with the vehicle. Fourteen-nm nanoparticles intensively aggravated LPS-elicited lung inflamma-

tion and pulmonary edema, which was concomitant with the enhanced lung expression of interleukin (IL)-1 $\beta$ , macrophage inflammatory protein (MIP)-1 $\alpha$ , macrophage chemoattractant protein (MCP)-1, MIP-2, and keratinocyte chemoattractant (KC) in overall trend, whereas 56-nm nanoparticles did not show apparent effects. Immunoreactivity for 8-hydroxyguanosine (OHdG), a proper marker for oxidative stress, was more intense in the lung from the LPS + 14-nm nanoparticle group than that from the LPS group. The circulatory fibrinogen level was higher in the LPS + 14-nm nanoparticle group than that in the LPS group. Taken together, nanoparticles can aggravate lung inflammation related to bacterial endotoxin, which is more prominent with smaller particles. The enhancing effect may be mediated, at least partly, via the increased local expression of proinflammatory cytokines and via the oxidative stress. Furthermore, nanoparticles can promote coagulatory disturbance accompanied by lung inflammation [34].

Furthermore, we examined the adverse effects of nanoparticles on this pathological model. In brief, ICR male mice were divided into 8 experimental groups that intratracheally received vehicle, three sizes (15, 50, 100 nm) of TiO<sub>2</sub> nanomaterials, LPS, or LPS plus nanomaterials. Twenty four hours after the treatment, both nanomaterials exacerbated the lung inflammation and edema elicited by LPS, with an overall trend of amplified lung expressions of cytokines such as IL-1 $\beta$ , MCP-1, and KC. LPS plus nanomaterials, especially with size less than 50 nm, elevated circulatory levels of fibrinogen, IL-1 $\beta$ , MCP-1, KC, and von Willebrand factor as compared with LPS alone. The enhancement tended overall to be greater with the smaller nanomaterials than that with the larger ones. cDNA microarray analyses revealed that gene expression pattern was not different between the LPS group and the LPS + nanomaterial groups. These results suggest that nanomaterials exacerbate lung inflammation related to LPS with systemic inflammation and coagulatory impairment, and the exacerbation is more prominent with smaller nanomaterials than that with larger ones ([35] and unpublished data). Additionally, we demonstrated that latex nanoparticles [36] and carbon nanotubes [37] have similar adverse effects on the lung pathophysiology.

Our next study was conducted to determine whether inhaled exposure to diesel engine-derived nanoparticles also exacerbates the model. ICR mice were exposed for 5 hours to clean air or diesel engine-derived nanoparticles at a concentration of 15, 36, or 169  $\mu\text{g}/\text{m}^3$  after intratracheal challenge with LPS or vehicle, and were sacrificed for evaluation 24 hours after the intratracheal challenge. Exposure to nanoparticles alone did not elicit lung inflammation. Nanoparticle inhalation exaggerated LPS-elicited inflammatory cell recruitment in the BAL fluid and lung parenchyma as compared with clean air inhalation in a concentration-dependent manner. Lung homogenates derived from the LPS + nanoparticle groups tended to have an increased tumor necrosis factor- $\alpha$  level and chemotaxis activity for polymorphonuclear leukocytes as compared with those from the LPS group or the corresponding nanoparticle groups. Nanoparticle inhalation did not significantly increase the lung expression of proinflammatory cytokines or influence

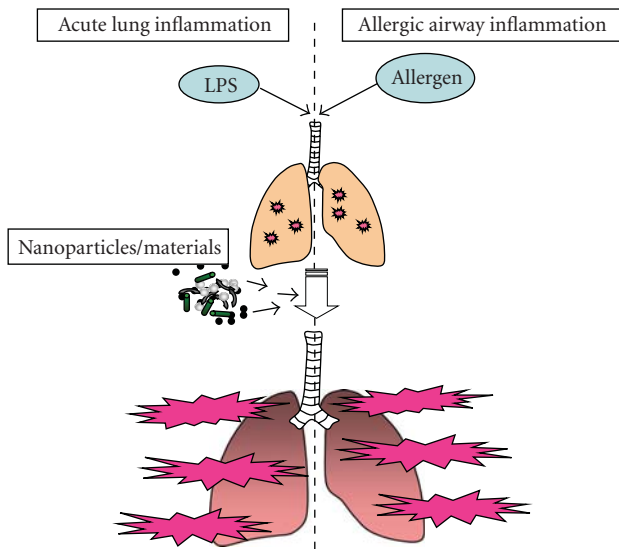


FIGURE 1: Proposal schema for enhancement of nanoparticles/materials on sensitive immune-related lung disorders.

systemic inflammation. Isolated alveolar macrophages from nanoparticle-exposed mice showed a greater production of IL-1 $\beta$  and KC stimulated with ex vivo LPS challenge than those from clean air-exposed mice although the differences did not reach significance. These results suggest that acute exposure to diesel-nanoparticles exacerbates lung inflammation induced by LPS [38]. In sum, nanoparticle/material exposure exacerbates acute lung inflammation related to bacterial endotoxin (Figure 1).

### 3. Effects of Nanoparticles on Allergic Airway Inflammation

Bronchial asthma has been recognized as chronic airway inflammation with hyperresponsiveness that is characterized by an increase in the number of activated lymphocytes and eosinophils [39]. A number of studies have shown that various particles including carbon black can enhance allergic sensitization [40–42], which is referred to as “adjuvant effect” as well. Carbon black has been demonstrated to enhance the proliferation of antibody-forming cells and both IgE and IgG levels [43, 44]. Ultrafine particles (PM and carbon black) reportedly exaggerate allergic airway inflammation *in vivo* [45, 46]. However, all studies have failed to pay attention to the size of particles. Therefore, no research has addressed the size effects of particles or nanoparticles on airway biology in the presence or absence of allergen *in vivo*. Given the hypothesis, we investigated the effects of carbon black nanoparticles with a diameter of 14 nm or 56 nm on allergen-related airway inflammation. ICR mice were divided into six experimental groups. Vehicle, two sizes of carbon nanoparticles, ovalbumin (OVA) and OVA + nanoparticles, were administered intratracheally. The cellular profile of BAL fluid, lung histology, expression of cytokines, chemokines, 8-OHdG, and immunoglobulin production were studied.

Nanoparticles with a diameter of 14 nm or 56 nm aggravated antigen-related airway inflammation characterized by the infiltration of eosinophils, neutrophils, and mononuclear cells, and by an increase in the number of goblet cells in the bronchial epithelium. Nanoparticles with antigen increased protein levels of IL-5, IL-6, IL-13, eotaxin, MCP-1, and regulated upon activation and normal T-cells expressed and secreted (RANTES) in the lung as compared with antigen alone. The formation of 8-OHdG was moderately induced by nanoparticles or allergen alone, and was markedly enhanced by allergen plus nanoparticles as compared with nanoparticles or allergen alone. The aggravation was more prominent with 14 nm nanoparticles than that with 56-nm particles in terms of the overall trend. Particles with a diameter of 14 nm exhibited an adjuvant activity for total IgE and antigen-specific IgG and IgE. Nanoparticles can aggravate allergen-related airway inflammation and immunoglobulin production, which become more prominent with smaller particles. The enhancement may be mediated, at least partly, by the increased local expression of IL-5 and eotaxin, and also by the modulated expression of IL-13, RANTES, MCP-1, and IL-6 [47]. Consistent with our study, de Haar and colleagues have previously shown that nanoparticles (14 and 29 nm) potently facilitate allergic airway inflammation as compared with fine particles (250 and 260 nm) [48].

In ongoing reports, nanoparticles alone or OVA alone moderately enhanced cholinergic airway reactivity, as assessed by total respiratory system resistance ( $R$ ) and Newtonian resistance ( $R_n$ ). All the parameters of lung responsiveness, such as  $R$ , compliance, elastance,  $R_n$ , tissue damping, and tissue elastance, were worse in the OVA + nanoparticle groups than those in the vehicle group, the corresponding nanoparticle groups, or the OVA group. The lung mRNA level for Muc5ac was significantly higher in the OVA group than that in the vehicle group, and further increased in the OVA + nanoparticle groups than that in the OVA or nanoparticle groups. These data suggest that carbon nanoparticles can enhance lung hyperresponsiveness, especially in the presence of allergen. The effects may be mediated, at least partly, through the enhanced lung expression of Muc5ac [49].

Furthermore, we recently demonstrated that (single-walled and multiwalled) carbon nanotubes promote allergic airway inflammation in mice, which may be partly through enhanced oxidative stress in the airway and the inappropriate activation of antigen-presenting cells including dendritic cells (*in vitro*) [50, 51]. In addition, other groups have reported the similar impacts of nanomaterials (carbon nanotubes, TiO<sub>2</sub>, and gold) us as on animal allergic asthma models [48, 52–54]. Moreover, as for cellular contribution, we and others have claimed that antigen-presenting cells such as dendritic cells are important target cell populations for the adjuvant activity of nanoparticles/materials [55–57]. Taken together, nanoparticle/material exposure can exacerbate allergic asthma (Figure 1).

### 4. Considerations for Future Directions

**4.1. Risk Factors Regarding Nanoparticles.** One important point to be taken into consideration in these studies is the

surface characteristics and numbers of nanoparticles used. Our results indicate that nanoparticles, particularly smaller ones (14 nm in diameter), can aggravate lung inflammation related to LPS and allergic airway inflammation when the weights of particles are equal. On the other hand, the surface area of the 14-nm nanoparticles was 6.7 fold larger than that of 56-nm nanoparticles ( $300 \text{ m}^2/\text{g}$  versus  $45 \text{ m}^2/\text{g}$ , resp.). The surface area of particles exposed to is reportedly correlated with lung inflammation [37]. Alternatively, our studies have demonstrated not only the size effects of nanoparticles on lung inflammation, but also the effects of their surface area and/or their numbers on the inflammation.

Unfortunately, we could not examine the effects of nanoparticles with the same particle number in these studies. The number of smaller nanoparticles is greater than that of larger nanoparticles when the particles comprise the same weight.

**4.2. Possibility of Migration and Influence of Nanoparticles Exposed to the Airway into Systemic Circulation.** It also remains to be argued whether nano-level particles/materials delivered through the airway enter the systemic circulation and cause serve adverse effects such as systemic inflammation and thrombus formation. Nanoparticles are reportedly able to penetrate deeply into the respiratory tract and can even pass the lung to reach systemic circulation [58, 59]. Nemmar et al. have previously demonstrated that nanoparticles can migrate into the circulation [59]. In our study, the LPS + nanoparticle groups, specifically the LPS + 14-nm nanoparticle group, showed significantly higher fibrinogen levels when compared to the LPS group. Additionally, although not significant, the enhanced activity of vWF induced by LPS was further increased by its combination with 14-nm nanoparticles [34]. These findings suggest that smaller nanoparticles can facilitate coagulatory disturbance accompanied by lung inflammation. The enhancing effects of 14-nm nanoparticles on LPS-elicited pulmonary edema further support this concept. Interestingly, exposure to nanoparticles alone did not induce significant fibrinogen production/release nor did it activate vWF. It might be hypothesized that endothelial-epithelial damage induced by LPS and subsequent infiltrating effector leukocytes allow a large amount of smaller nanoparticles to pass easily into the circulation, resulting in synergistic effects on hemostasis including coagulatory disturbance. On the other hand, exposure to environmental particles reportedly generates local and systemic oxidative stress, which, in turn, induces/enhances inflammation and blood coagulation [58]. Further, Nemmar and colleagues have demonstrated that nanoparticles instilled intratracheally rapidly diffuse from the lung into the systemic circulation *in vivo* [59]. Therefore, it is also possible that intratracheally instilled nanoparticles enter the circulation by themselves and contribute to a high susceptibility to LPS-elicited systemic inflammation and coagulatory disturbance. Future studies are needed to confirm the penetration and address the above-mentioned hypothesis.

**4.3. Model's Relevance to the Actual Situation.** In reality, we inhale suspended particulate matters in ambient

air, but do not intratracheally receive them in aliquot. Nevertheless, the impacts of inhalation exposure to these particles/materials, the more realistic exposure, on this lung inflammation model had less been conducted by us and others. In our previous study, nanoparticle-rich diesel exhaust inhalation exaggerated lung inflammation induced by LPS [38]. Nonetheless, we have not completed/examined the effects of the inhalation on other disease models. In future, therefore, more realistic research considering the effects of the mode of nanoparticles/materials administration (instillation versus aerosolization, droplets versus powder, etc.) on the *in vivo* response would be very valuable to toxicologists, environmental scientists, and immunologists.

## Acknowledgments

Special thanks to Professor Takamichi Ichinose, Professor Seishiro Hirano, Dr. Rie Yanagisawa, and Dr. Eiko Koike for greatly contributing to the work in the paper. The authors are supported by NIES Grants.

## References

- [1] J. M. Samet, F. Dominici, F. C. Curriero, I. Coursac, and S. L. Zeger, "Fine particulate air pollution and mortality in 20 U.S. cities, 1987–1994," *New England Journal of Medicine*, vol. 343, no. 24, pp. 1742–1749, 2000.
- [2] A. Peters, H. E. Wichmann, T. Tuch, J. Heinrich, and J. Heyder, "Respiratory effects are associated with the number of ultrafine particles," *American Journal of Respiratory and Critical Care Medicine*, vol. 155, no. 4, pp. 1376–1383, 1997.
- [3] M. Szyszkowicz, "Air pollution and emergency department visits for depression in Edmonton, Canada," *International Journal of Occupational Medicine and Environmental Health*, vol. 20, no. 3, pp. 241–245, 2007.
- [4] N. Künzli, P.-O. Bridevaux, L.-J. S. Liu et al., "Traffic-related air pollution correlates with adult-onset asthma among never-smokers," *Thorax*, vol. 64, no. 8, pp. 664–670, 2009.
- [5] B. Neupane, M. Jerrett, R. T. Burnett, T. Marrie, A. Arain, and M. Loeb, "Long-term exposure to ambient air pollution and risk of hospitalization with community-acquired pneumonia in older adults," *American Journal of Respiratory and Critical Care Medicine*, vol. 181, no. 1, pp. 47–53, 2010.
- [6] D. W. Dockery, C. A. Pope III, X. Xu et al., "An association between air pollution and mortality in six U.S. cities," *New England Journal of Medicine*, vol. 329, no. 24, pp. 1753–1759, 1993.
- [7] A. Nemmar, S. Al-Salam, S. Zia, J. Yasin, I. Al Husseni, and B. H. Ali, "Diesel exhaust particles in the lung aggravate experimental acute renal failure," *Toxicological Sciences*, vol. 113, no. 1, pp. 267–277, 2009.
- [8] F. D. T. Q. S. Lopes, T. S. Pinto, F. M. Arantes-Costa et al., "Exposure to ambient levels of particles emitted by traffic worsens emphysema in mice," *Environmental Research*, vol. 109, no. 5, pp. 544–551, 2009.
- [9] K.-I. Inoue, H. Takano, R. Yanagisawa, T. Ichinose, A. Shimada, and T. Yoshikawa, "Pulmonary exposure to diesel exhaust particles induces airway inflammation and cytokine expression in NC/Nga mice," *Archives of Toxicology*, vol. 79, no. 10, pp. 595–599, 2005.

- [10] T. Ichinose, A. Furuyama, and M. Sagai, "Biological effects of diesel exhaust particles (DEP). II. Acute toxicity of DEP introduced into lung by intratracheal instillation," *Toxicology*, vol. 99, no. 3, pp. 153–167, 1995.
- [11] T. Ichinose, Y. Yajima, M. Nagashima, S. Takenoshita, Y. Nagamachi, and M. Sagai, "Lung carcinogenesis and formation of 8-hydroxy-deoxyguanosine in mice by diesel exhaust particles," *Carcinogenesis*, vol. 18, no. 1, pp. 185–192, 1997.
- [12] H. Takano, T. Yoshikawa, T. Ichinose, Y. Miyabara, K. Imaoka, and M. Sagai, "Diesel exhaust particles enhance antigen-induced airway inflammation and local cytokine expression in mice," *American Journal of Respiratory and Critical Care Medicine*, vol. 156, no. 1, pp. 36–42, 1997.
- [13] H. Takano, R. Yanagisawa, T. Ichinose et al., "Diesel exhaust particles enhance lung injury related to bacterial endotoxin through expression of proinflammatory cytokines, chemokines, and intercellular adhesion molecule-1," *American Journal of Respiratory and Critical Care Medicine*, vol. 165, no. 9, pp. 1329–1335, 2002.
- [14] K.-I. Inoue, H. Takano, M. Sakurai et al., "Pulmonary exposure to diesel exhaust particles enhances coagulatory disturbance with endothelial damage and systemic inflammation related to lung inflammation," *Experimental Biology and Medicine*, vol. 231, no. 10, pp. 1626–1632, 2006.
- [15] K.-I. Inoue, E. Koike, H. Takano, R. Yanagisawa, T. Ichinose, and T. Yoshikawa, "Effects of diesel exhaust particles on antigen-presenting cells and antigen-specific Th immunity in mice," *Experimental Biology and Medicine*, vol. 234, no. 2, pp. 200–209, 2009.
- [16] J. Cyrys, M. Stölzel, J. Heinrich et al., "Elemental composition and sources of fine and ultrafine ambient particles in Erfurt, Germany," *Science of the Total Environment*, vol. 305, no. 1–3, pp. 143–156, 2003.
- [17] K. L. Timonen, G. Hoek, J. Heinrich et al., "Daily variation in fine and ultrafine particulate air pollution and urinary concentrations of lung Clara cell protein CC16," *Occupational and Environmental Medicine*, vol. 61, no. 11, pp. 908–914, 2004.
- [18] Y. Zhu, W. C. Hinds, S. Kim, and C. Sioutas, "Concentration and size distribution of ultrafine particles near a major highway," *Journal of the Air and Waste Management Association*, vol. 52, no. 9, pp. 1032–1042, 2002.
- [19] M. J. Utell and M. W. Frampton, "Acute health effects of ambient air pollution: the ultrafine particle hypothesis," *Journal of Aerosol Medicine*, vol. 13, no. 4, pp. 355–359, 2000.
- [20] G. Oberdörster, "Pulmonary effects of inhaled ultrafine particles," *International Archives of Occupational and Environmental Health*, vol. 74, no. 1, pp. 1–8, 2001.
- [21] A. Seaton, W. MacNee, K. Donaldson, and D. Godden, "Particulate air pollution and acute health effects," *Lancet*, vol. 345, no. 8943, pp. 176–178, 1995.
- [22] D. M. Brown, M. R. Wilson, W. MacNee, V. Stone, and K. Donaldson, "Size-dependent proinflammatory effects of ultrafine polystyrene particles: a role for surface area and oxidative stress in the enhanced activity of ultrafines," *Toxicology and Applied Pharmacology*, vol. 175, no. 3, pp. 191–199, 2001.
- [23] C. A. J. Dick, D. M. Brown, K. Donaldson, and V. Stone, "The role of free radicals in the toxic and inflammatory effects of four different ultrafine particle types," *Inhalation Toxicology*, vol. 15, no. 1, pp. 39–52, 2003.
- [24] N. Li, C. Sioutas, A. Cho et al., "Ultrafine particulate pollutants induce oxidative stress and mitochondrial damage," *Environmental Health Perspectives*, vol. 111, no. 4, pp. 455–460, 2003.
- [25] R. F. Service, "Nanotechnology grows up," *Science*, vol. 304, no. 5678, pp. 1732–1734, 2004.
- [26] H. Gong Jr., W. S. Linn, K. W. Clark et al., "Exposures of healthy and asthmatic volunteers to concentrated ambient ultrafine particles in Los Angeles," *Inhalation Toxicology*, vol. 20, no. 6, pp. 533–545, 2008.
- [27] M. W. Frampton, J. C. Stewart, G. Oberdörster et al., "Inhalation of ultrafine particles alters blood leukocyte expression of adhesion molecules in humans," *Environmental Health Perspectives*, vol. 114, no. 1, pp. 51–58, 2006.
- [28] M. P. Vincenti, T. A. Burrell, and S. M. Taffet, "Regulation of NF- $\kappa$ B activity in murine macrophages: effect of bacterial lipopolysaccharide and phorbol ester," *Journal of Cellular Physiology*, vol. 150, no. 1, pp. 204–213, 1992.
- [29] T. R. Ulich, L. R. Watson, S. Yin et al., "The intratracheal administration of endotoxin and cytokines: I. Characterization of LPS-induced IL-1 and TNF mRNA expression and the LPS-, IL-1-, and TNF-induced inflammatory infiltrate," *American Journal of Pathology*, vol. 138, no. 6, pp. 1485–1496, 1991.
- [30] P. G. Flanagan, S. K. Jackson, and G. Findlay, "Diagnosis of gram negative, ventilator associated pneumonia by assaying endotoxin in bronchial lavage fluid," *Journal of Clinical Pathology*, vol. 54, no. 2, pp. 107–110, 2001.
- [31] T. R. Martin, G. D. Rubenfeld, J. T. Ruzinski et al., "Relationship between soluble CD14, lipopolysaccharide binding protein, and the alveolar inflammatory response in patients with acute respiratory distress syndrome," *American Journal of Respiratory and Critical Care Medicine*, vol. 155, no. 3, pp. 937–944, 1997.
- [32] S. Becker, M. J. Fenton, and J. M. Soukup, "Involvement of microbial components and toll-like receptors 2 and 4 in cytokine responses to air pollution particles," *American Journal of Respiratory Cell and Molecular Biology*, vol. 27, no. 5, pp. 611–618, 2002.
- [33] R. Yanagisawa, H. Takano, K. Inoue et al., "Enhancement of acute lung injury related to bacterial endotoxin by components of diesel exhaust particles," *Thorax*, vol. 58, no. 7, pp. 605–612, 2003.
- [34] K.-I. Inoue, H. Takano, R. Yanagisawa et al., "Effects of airway exposure to nanoparticles on lung inflammation induced by bacterial endotoxin in mice," *Environmental Health Perspectives*, vol. 114, no. 9, pp. 1325–1330, 2006.
- [35] K.-I. Inoue, H. Takano, M. Ohnuki et al., "Size effects of nanomaterials on lung inflammation and coagulatory disturbance," *International Journal of Immunopathology and Pharmacology*, vol. 21, no. 1, pp. 197–206, 2008.
- [36] K.-I. Inoue, H. Takano, R. Yanagisawa, E. Koike, and A. Shimada, "Size effects of latex nanomaterials on lung inflammation in mice," *Toxicology and Applied Pharmacology*, vol. 234, no. 1, pp. 68–76, 2009.
- [37] K.-I. Inoue, H. Takano, E. Koike et al., "Effects of pulmonary exposure to carbon nanotubes on lung and systemic inflammation with coagulatory disturbance induced by lipopolysaccharide in mice," *Experimental Biology and Medicine*, vol. 233, no. 12, pp. 1583–1590, 2008.
- [38] K.-I. Inoue, H. Takano, R. Yanagisawa et al., "Effects of inhaled nanoparticles on acute lung injury induced by lipopolysaccharide in mice," *Toxicology*, vol. 238, no. 2–3, pp. 99–110, 2007.
- [39] D. K. Agrawal and Z. Shao, "Pathogenesis of allergic airway inflammation," *Current Allergy and Asthma Reports*, vol. 10, no. 1, pp. 39–48, 2010.

- [40] K. Maejima, K. Tamura, Y. Taniguchi, S. Nagase, and H. Tanaka, "Comparison of the effects of various fine particles on IgE antibody production in mice inhaling Japanese cedar pollen allergens," *Journal of Toxicology and Environmental Health, Part A*, vol. 52, no. 3, pp. 231–248, 1997.
- [41] A. L. Lambert, W. Dong, D. W. Winsett, M. K. Selgrade, and M. I. Gilmour, "Residual oil fly ash exposure enhances allergic sensitization to house dust mite," *Toxicology and Applied Pharmacology*, vol. 158, no. 3, pp. 269–277, 1999.
- [42] A. L. Lambert, W. Dong, M. K. Selgrade, and M. I. Gilmour, "Enhanced allergic sensitization by residual oil fly ash particles is mediated by soluble metal constituents," *Toxicology and Applied Pharmacology*, vol. 165, no. 1, pp. 84–93, 2000.
- [43] M. Løvik, A.-K. Høgseth, P. I. Gaarder, R. Hagemann, and I. Eide, "Diesel exhaust particles and carbon black have adjuvant activity on the local lymph node response and systemic IgE production to ovalbumin," *Toxicology*, vol. 121, no. 2, pp. 165–178, 1997.
- [44] M. Van Zijverden, A. Van der Pijl, M. Bol et al., "Diesel exhaust, carbon black, and silica particles display distinct Th1/Th2 modulating activity," *Toxicology and Applied Pharmacology*, vol. 168, no. 2, pp. 131–139, 2000.
- [45] J. A. Last, R. Ward, L. Temple, K. E. Pinkerton, and N. J. Kenyon, "Ovalbumin-induced airway inflammation and fibrosis in mice also exposed to ultrafine particles," *Inhalation Toxicology*, vol. 16, no. 2, pp. 93–102, 2004.
- [46] N. H. Al-Humadi, P. D. Siegel, D. M. Lewis et al., "The effect of diesel exhaust particles (DEP) and carbon black (CB) on thiol changes in pulmonary ovalbumin allergic sensitized brown norway rats," *Experimental Lung Research*, vol. 28, no. 5, pp. 333–349, 2002.
- [47] K.-I. Inoue, H. Takano, R. Yanagisawa et al., "Effects of nanoparticles on antigen-related airway inflammation in mice," *Respiratory Research*, vol. 6, article 106, 2005.
- [48] C. De Haar, I. Hassing, M. Bol, R. Bleumink, and R. Pieters, "Ultrafine but not fine particulate matter causes airway inflammation and allergic airway sensitization to co-administered antigen in mice," *Clinical and Experimental Allergy*, vol. 36, no. 11, pp. 1469–1479, 2006.
- [49] K. Inoue, H. Takano, R. Yanagisawa et al., "Effects of nanoparticles on lung physiology in the presence or absence of antigen," *International Journal of Immunopathology and Pharmacology*, vol. 20, no. 4, pp. 737–744, 2007.
- [50] K.-I. Inoue, E. Koike, R. Yanagisawa, S. Hirano, M. Nishikawa, and H. Takano, "Effects of multi-walled carbon nanotubes on a murine allergic airway inflammation model," *Toxicology and Applied Pharmacology*, vol. 237, no. 3, pp. 306–316, 2009.
- [51] K. Inoue, R. Yanagisawa, E. Koike, M. Nishikawa, and H. Takano, "Repeated pulmonary exposure to single-walled carbon nanotubes exacerbates allergic inflammation of the airway: possible role of oxidative stress," *Free Radical Biology and Medicine*, vol. 48, no. 7, pp. 924–934, 2010.
- [52] U. C. Nygaard, J. S. Hansen, M. Samuelsen, T. Alberg, C. D. Marioara, and M. Løvik, "Single-walled and multi-walled carbon nanotubes promote allergic immune responses in mice," *Toxicological Sciences*, vol. 109, no. 1, pp. 113–123, 2009.
- [53] J. P. Ryman-Rasmussen, E. W. Tewksbury, O. R. Moss, M. F. Cesta, B. A. Wong, and J. C. Bonner, "Inhaled multiwalled carbon nanotubes potentiate airway fibrosis in murine allergic asthma," *American Journal of Respiratory Cell and Molecular Biology*, vol. 40, no. 3, pp. 349–358, 2009.
- [54] S. Hussain, J. A. Vanoirbeek, K. Luyts et al., "Lung exposure to nanoparticles modulates an asthmatic response in a mouse model of asthma," *European Respiratory Journal*. In press.
- [55] E. Koike, H. Takano, K.-I. Inoue, R. Yanagisawa, and T. Kobayashi, "Carbon black nanoparticles promote the maturation and function of mouse bone marrow-derived dendritic cells," *Chemosphere*, vol. 73, no. 3, pp. 371–376, 2008.
- [56] E. Koike, H. Takano, K.-I. Inoue et al., "Pulmonary exposure to carbon black nanoparticles increases the number of antigen-presenting cells in murine lung," *International Journal of Immunopathology and Pharmacology*, vol. 21, no. 1, pp. 35–42, 2008.
- [57] C. de Haar, M. Kool, I. Hassing, M. Bol, B. N. Lambrecht, and R. Pieters, "Lung dendritic cells are stimulated by ultrafine particles and play a key role in particle adjuvant activity," *Journal of Allergy and Clinical Immunology*, vol. 121, no. 5, pp. 1246–1254, 2008.
- [58] W. MacNee and K. Donaldson, "How can ultrafine particles be responsible for increased mortality?" *Monaldi Archives for Chest Disease*, vol. 55, no. 2, pp. 135–139, 2000.
- [59] A. Nemmar, H. Vanilloen, M. F. Hoylaerts, P. H. M. Hoet, A. Verbruggen, and B. Nemery, "Passage of intratracheally instilled ultrafine particles from the lung into the systemic circulation in hamster," *American Journal of Respiratory and Critical Care Medicine*, vol. 164, no. 9, pp. 1665–1668, 2001.

## Review Article

# Evaluating the Controlled Release Properties of Inhaled Nanoparticles Using Isolated, Perfused, and Ventilated Lung Models

**Moritz Beck-Broichsitter, Thomas Schmehl, Werner Seeger, and Tobias Gessler**

*Medical Clinic II, Department of Internal Medicine, Justus-Liebig-Universität Giessen, Klinikstraße 36, 35392 Giessen, Germany*

Correspondence should be addressed to Tobias Gessler, tobias.gessler@innere.med.uni-giessen.de

Received 31 August 2010; Accepted 22 November 2010

Academic Editor: Hugh D. Smyth

Copyright © 2011 Moritz Beck-Broichsitter et al. This is an open access article distributed under the Creative Commons Attribution License, which permits unrestricted use, distribution, and reproduction in any medium, provided the original work is properly cited.

Polymeric nanoparticles meet the increasing interest for inhalation therapy and hold great promise to improve controlled drug delivery to the lung. The synthesis of tailored polymeric materials and the improvement of nanoparticle preparation techniques facilitate new perspectives for the treatment of severe pulmonary diseases. The physicochemical properties of such drug delivery systems can be investigated using conventional analytical procedures. However, the assessment of the controlled drug release properties of polymeric nanoparticles in the lung remains a considerable challenge. In this context, the isolated lung technique is a promising tool to evaluate the drug release characteristics of nanoparticles intended for pulmonary application. It allows measurements of lung-specific effects on the drug-release properties of pulmonary delivery systems. *Ex vivo* models are thought to overcome the common obstacles of *in vitro* tests and offer more reliable drug release and distribution data that are closer to the *in vivo* situation.

## 1. Introduction

Pulmonary drug delivery has become a well-established approach in the treatment of respiratory diseases and offers several advantages over other routes of administration. Inhalation therapy enables the direct application of a drug to the respiratory tract. The “local” or “regional” deposition of the administered drug facilitates a targeted treatment of respiratory diseases avoiding high-dose exposures to the systemic circulation. With the direct delivery of therapeutic agents to the desired site of action, rapid onset of drug action, lower systemic exposure, and consequently, reduced side effects can be achieved. Site-specific or targeted delivery, therefore, would also enable a reduction in the necessary dose to be administered [1–4]. A significant disadvantage of inhalation therapy is the relatively short duration of drug action demanding multiple daily inhalation maneuvers, ranging up to 9 times a day [5]. Moreover, “conventional” inhalation therapy does not permit targeted cell-specific drug delivery or modified biological distribution of drugs, both at

the organ and cellular level, and drug deposition in different lung areas is only poorly controllable [6–8].

Strategies for further advancements of inhalation therapy include the development of aerosolizable controlled release formulations with the aim to improve the drug effect, as well as the patient’s convenience and compliance. A large number of carrier systems have been conceived and investigated as potential controlled drug delivery formulations to the lung [9–11]. In the recent years, nanomedicine has become an attractive concept for the controlled and targeted delivery of therapeutic and diagnostic compounds to the desired site of action. Nanotechnology opens new perspectives in the design of novel drug delivery vehicles that not only facilitate targeting of an organ, tissues, cells, or subcellular compartments, but also affect the duration and the intensity of the pharmacological effect [12–16]. In particular, nanoparticulate drug delivery systems enable the controlled delivery of the pharmacological agent to its site of action at a therapeutically optimal rate and dose regimen [17–19]. Among the various drug delivery systems considered for pulmonary application,

Polymeric nanoparticles demonstrate several advantages for the treatment of respiratory diseases, for example prolonged drug release and cell-specific targeted drug delivery [20–24].

Numerous manufacturing techniques are known for the production of drug-loaded polymeric nanoparticles. The choice of the nanoparticle preparation technique essentially depends on the physicochemical properties of the polymeric nanoparticle matrix material intended to be used and on the active compound to be encapsulated in the nanoparticles [25, 26]. Regarding the polymeric nanoparticle matrix material, criteria such as biocompatibility and degradability determine its selection [27–29]. Moreover, for an effective nanoparticulate drug delivery system, sufficient drug loading and controlled drug release over a predetermined period of time must be ensured. The characteristics of drug release, that is, release mechanism and release rate, from drug-delivery systems vary according to the type of employed encapsulation technique and the physicochemical properties (interaction) of drug and polymer. The release from polymeric nanoparticles *in vitro* is normally fast (several minutes to hours) due to the short distance drugs have to cover to diffuse out of the particles. The release rate of drugs from nanoparticles is also strongly influenced by the biological environment. Nanoparticles may interact with biological components like proteins and cells that alter the release rate of drugs from nanoparticles. As a consequence, the *in vitro* drug release characteristics may not predict the release situation *in vivo*. Moreover, a precise assessment of the *in vitro* drug release from nanoparticles is technically difficult to achieve, which is mainly attributed to the inability of rapid separation of the nanoparticles from the dissolved or released drug in the surrounding medium [17, 30, 31].

Different methods have been used to characterize the behavior of pulmonary administered drug-loaded carriers in biological systems. These range from *in vitro* cell culture methods to *in vivo* pharmacokinetic analysis. *Ex vivo* isolated, perfused, and ventilated lung models have been utilized in numerous pharmacological and toxicological studies to elucidate the fate of inhaled drugs or toxic substances. In *ex vivo* lung models, lung-specific pharmacokinetic effects, like drug absorption and distribution profiles, can be investigated without the contribution of systemic absorption, distribution, and elimination of the drug. Moreover, it is possible to elucidate the effect of the interaction of nanoparticles with the natural pulmonary environment on the release of encapsulated drugs. Accordingly, more reliable drug release and distribution data are obtained that are closer to the *in vivo* situation [6, 32–34].

It is interesting to note that the first investigations regarding the use of polymeric nanoparticles as drug carriers for the controlled and targeted delivery of drugs to the desired site of action have been reported in the mid 1970's [35]. It was shown that the "natural" drug distribution after systemic application was altered by the encapsulation of drug into polymeric nanoparticles. Since then, great efforts have been made in this field, and several treatment modalities for cancer on the basis of polymeric nanostructured drug delivery vehicles have been developed and made clinically available, for example, Abraxane, Transdrug, and Genexol-

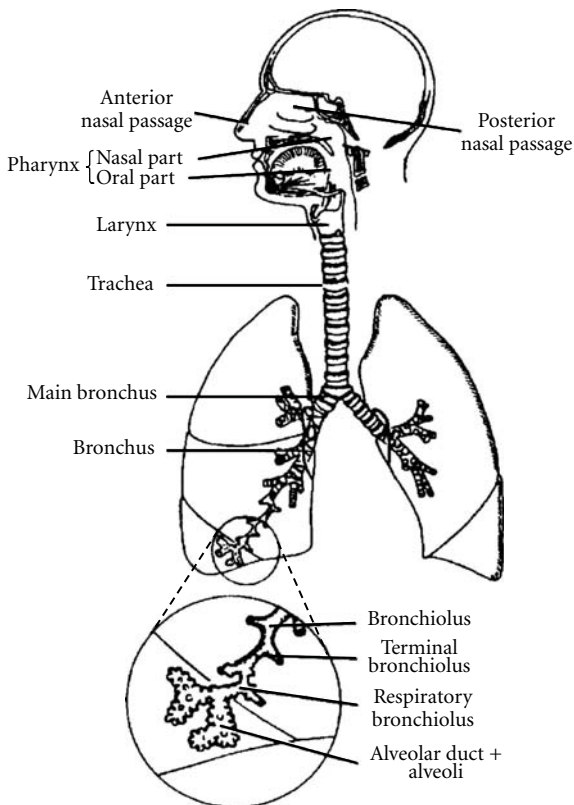


FIGURE 1: Schematic of the human respiratory system (Adapted from [43]).

PM [25, 36, 37]. In contrast to systemic administration, the regional application of drug-loaded nanoparticles to the respiratory tract has been so far incompletely investigated. This is attributed on one hand to the limited efficiency of conventional devices to generate nanoparticle-containing aerosols and on the other hand to the lack of methods to assess the drug release form and the distribution behavior of pulmonary administered nanoparticulate drug-delivery systems [38, 39]. Meanwhile, technological advances have led to improved designs for aerosol-generation devices that solve the main drawbacks, and the key attributes associated with successful nanoparticle aerosolization have been identified [40–42]. However, the prediction of drug release and distribution from pulmonary administered nanoparticulate-delivery systems remains a major challenge.

## 2. Structure and Function of the Lung

The development of drug delivery systems for pulmonary application requires a detailed knowledge of the lung in its healthy, as well as various diseased states. The lung is composed of more than 40 different cell types, of which approximately one-third are epithelial cells [44, 45]. The conducting zone includes the nasal cavity, pharynx, larynx, trachea, bronchi, and bronchioles, while the respiratory zone, where the gas exchange takes place, includes respiratory bronchioles and alveoli (Figure 1). The conducting airways

exhibit 16 bifurcations, comprising the trachea, the bronchi, and the bronchioles. The terminal bronchioles represent the passage to the respiratory region, which exhibits another 6 bifurcations. The respiratory region includes the respiratory bronchioles, from which the alveolar ducts with alveolar sacs branch off [46]. The airways also fulfill some other essential functions, such as warming, humidifying, and cleaning of the inhaled air. Warming and humidifying of the inspired air predominantly take place in the nasal cavity and the pharynx. In the deeper airways this process continues, so that the air finally reaching the alveoli has body heat and is completely saturated with water. Also the cleaning of the inspired air partly takes place in the nose; dust, bacteria, and particles are caught by impaction. Further inhaled substances deposit on the mucus layer which coats the walls of the conducting airways. The mucus is secreted by goblet and submucosal gland cells and forms a gel like layer consisting of mucin as the major component [47]. Ciliated cells are another important type of cells which predominate in the bronchial epithelia of the conducting region. Their major function is the propulsion of mucus upwards and out of the lung (bronchotracheal escalator), thus the lung will be cleared of foreign substances [48, 49]. Beneath, in the respiratory bronchioles the epithelium consists of ciliated cells and Clara cells.

In the alveolar space there is no mucus layer, but a complex surfactant lining that covers the alveolar epithelium and reduces the surface tension to prevent collapse of the alveoli during breathing [50]. It contains approximately 90% lipids and 10% proteins [51]. The lipids in the surface lining material consist mainly of phospholipids (~80–90%) and a minor portion of neutral lipids (~10–20%). Among the phospholipids, phosphatidylcholines (~70–80%) and phosphatidylglycerols (~10%) represent the predominant classes, with minor amounts of phosphatidylinositols, phosphatidylserines, and phosphatidylethanolamines [52]. About half of the protein mass of the alveolar lining layer is composed of the surfactant-associated proteins SP-A and SP-D, which are high molecular weight hydrophilic proteins, and SP-B and SP-C, which are low molecular weight hydrophobic proteins [53]. The surfactant proteins SP-A and SP-D have been identified as playing a fundamental role in innate immunity. A complex interaction between phospholipids and SP-B and SP-C enables the decrease of surface tension in the alveolar region to values of ~0 mN/m during compression/expansion cycles [54, 55]. Pulmonary surfactant is secreted by type II pneumocytes, which cover only 5% of the total alveolar surface. Beside the production of pulmonary surfactant, alveolar type II cells play a role in alveolar fluid balance, coagulation and fibrinolysis, host defense and proliferation, and differentiation into type I cells [56]. Type I pneumocytes are very thin ( $\leq 200\text{ nm}$ ) with a large extension (~200  $\mu\text{m}$ ), covering over ~95% of the alveolar epithelial surface [57]. They form the primary diffusion barrier between air and blood which is highly permeable for water, gases, and hydrophobic molecules, while it is poorly permeable for large hydrophilic substances (peptides and proteins) or ionic species. Macromolecules pass this barrier by active transport mechanisms [7, 58, 59]. In addition to epithelial cells, the alveoli contain

macrophages that engulf particles, potentially digest them, and slowly migrate with their payload out of the respiratory tract, either following along the mucociliary escalator or (to a lesser degree) the lymphatic system. Thus, the pulmonary endocytosis by macrophages represents the main mechanism of removing solid particles in the alveolar region [60, 61].

Nanoparticles have been praised for their advantageous drug delivery properties to the lung, such as avoidance of mucociliary and macrophage clearance and long residence times until degradation or translocation by epithelial cells takes place [6, 62–70].

### 3. Pulmonary Drug Delivery

*3.1. The Lung as a Route of Application for Systemic and Local Therapy.* Although the lung represents effective barrier systems and clearance mechanisms much attention has been raised in the last decades to this organ for drug delivery applications. One reason is its large absorption area. The lung build up a total surface of  $\sim 100\text{ m}^2$  that is enveloped by an equally large capillary network, from which many agents can be readily absorbed to the bloodstream avoiding a first-pass-effect of the liver. Another reason is the known instability and low permeability of proteins and peptides when these biopharmaceuticals are administered through the widely preferred oral route. Consequently, most proteins and peptides on the market are administered intravenously. But the parenteral route of application does generally not meet with patients' convenience and compliance, in particular because the indication for the use of these agents is usually treatment of a chronic disease requiring frequent injections. Thus, the pulmonary route of application offers a noninvasive alternative for systemic therapy [71–77]. However, systemic macromolecule delivery via the lung has suffered setbacks as for example demonstrated for pulmonary administered insulin (Exubera) that was withdrawn from the market in 2008 for commercial and health-risk reasons [78, 79].

A large number of small molecular weight drugs are employed for the targeted treatment of respiratory diseases following inhalation. This basic concept of targeted drug therapy has been followed for a long time in the treatment of airway diseases. In particular, the application of  $\beta_2$ -agonists and corticosteroids by means of inhalation has improved the therapy of bronchial asthma and chronic obstructive pulmonary disease targeting the smooth musculature of the bronchi and immunologically competent intrapulmonary cells [80, 81]. In addition, the endothelial cells or the smooth muscle cells surrounding the pulmonary vessels present a target of inhalative drug therapy. As an example, prostaglandin derivatives have been recently introduced for aerosol therapy of pulmonary arterial hypertension [82, 83].

*3.2. Devices for Aerosol Generation.* Over the past decades several devices have been conceived and developed for the administration of drugs to the respiratory tract, namely pressurized metered dose inhalers (pMDIs), dry powder inhalers (DPIs), and nebulizers [84–87]. pMDIs are hand-held devices that use pressurized propellants to atomize

the drug solution, suspension, or emulsion. These devices generally require a coordinative inhalation by the patient [88]. DPIs do not only differ in the principle of aerosol particle generation and delivery, but also with regard to design differences such as discrete or reservoir drug containment and the number of doses [89]. While the drugs are released from pMDI by the utilization of propellants, DPIs operate by using the inspiratory flow of the patient for disintegration of the powder and dose entrainment. Thus, reproducibility of the inhaled dose from these devices is extremely dependant on the patient [90]. Several types of nebulizers are available for aerosol generation for pulmonary drug delivery, namely jet nebulizers, ultrasonic nebulizers, and nebulizers that use a vibrating-mesh technology for aerosol generation [91]. Jet nebulizers are driven by compressed air. The liquid is dispersed into small droplets ( $<5\text{-}6\,\mu\text{m}$ ) by passing through a narrow nozzle orifice and multiple impactions on a baffle structure. In general, the droplet size distribution of a nebulizer and the output rate are also influenced by the physical properties of the drug solution and the air flow rate from the compressor [92]. Ultrasonic nebulizers use a piezoelectric transducer in order to create droplets from an open liquid reservoir. As the energy is transferred through the liquid container it becomes evident that the properties of the drug formulation have strong effects on the aerosol particle size and the output rate [93]. Vibrating-mesh nebulizers use perforated membranes actuated by an annular piezoelement to vibrate in resonant bending mode. The holes in the membrane have a large cross-section size on the liquid supply side and a narrow cross-section size on the side from where the droplets emerge. Depending on the therapeutic application, the hole sizes (2  $\mu\text{m}$  and upwards) can be adjusted, as well as the number of holes [40, 41, 94].

**3.3. Polymeric Nanoparticles as Inhalative Drug-Delivery Vehicles.** Nanomaterials exploit novel physical, chemical, and biological properties [14–16]. The general aim of controlled release formulations is the modification of pharmacokinetics and thus, improved pharmacodynamic characteristics at the target site. A successful drug delivery system needs to demonstrate optimal drug loading and release properties, and low toxicity [17, 20, 23, 24, 95–98]. Nanoparticle formulations for this purpose with a mean size between 50 and 300 nm normally consist of polymeric materials. Polymers with particular physical or chemical characteristics, such as biocompatibility, degradability, or responsiveness to environmental changes have been predominantly used [99]. In addition to biocompatibility and degradability of the applied polymer, sufficient association of the therapeutic agent with the carrier particles and controlled and targeted drug release properties, nanoparticles need to meet further standards, such as protection of the drug against degradation, ability to be transferred into an aerosol, and stability against forces generated during aerosolization. Nanoparticles composed of biodegradable polymers fulfill the stringent requirements placed on these delivery systems [22–24].

Due to their well-established biocompatibility and biodegradability, aliphatic polyesters like polylactide (PLA)

and poly(lactide-co-glycolide) (PLGA) are the most extensively used materials for biomedical applications [27]. However, linear polyesters have many limitations as nanoparticle matrix materials. Firstly, PLGA nanoparticles degrade over a period of weeks to months, but typically deliver drugs for a much shorter period of time. Slow or nondegrading polymers may lead to an unwanted accumulation in the lung when repeated administrations are needed, and may cause inflammatory processes [20, 95]. One way to overcome this problem is to synthesize polymers with faster degradation rates. Fast-degrading polymers are obtained by grafting of short PLGA chains onto polyvinyl alcohol backbones [100, 101]. The adjustable properties of these branched polyesters make them highly suitable for pulmonary formulations, especially with regard to biodegradation rates and *in vitro* cytotoxicity [102, 103]. Moreover, these types of biodegradable polyester revealed no signs of inflammatory response *in vivo* [104]. Their amphiphilic properties allows the generation of nanoparticles without the use of additional surfactant stabilizers [105, 106]. Another type of biodegradable polymer suitable for pulmonary application is based on ether-anhydride terpolymers consisting of poly(ethylene glycol), sebacic acid, and 1,3-bis(carboxyphenoxy)propane. These polymers are known to form aerosolizable particles and to exhibit fast degradation rates (half-life <12 h) [107–109].

Secondly, for an effective nanoparticulate-delivery system, sufficient drug-loading and tailored release properties must be ensured. Nanoparticles prepared from hydrophobic polymers, like PLGA, often incur the drawback of poor incorporation of low molecular weight hydrophilic drugs due to the low affinity of the drug compounds to the polymers [110, 111]. The introduction of charged functional groups within the polymer structure, like for example described by Wittmar et al. and Wang et al., promotes electrostatic interactions with oppositely charged drugs, thereby improving the design of nanoparticulate carriers [112, 113].

The release rate and release mechanism from drug-delivery systems vary according to the carrier vehicle, as well as to the properties of the employed drug and polymer combination. The *in vitro* release pattern from polymeric nanoparticles used in the field of medicine and pharmacy is of importance for characterization purposes and for quality control reasons. The release of drug compounds from nanoparticulate drug delivery systems is a result of the direct interaction of nanoparticles with their environment and is thought to be dependent upon desorption of the surface-bound, adsorbed drug, diffusion through the nanoparticle matrix, and rate of polymer degradation. Thus, diffusion and biodegradation govern the process of drug release from polymeric nanoparticles [17, 30, 31].

Several manufacturing techniques are known for the production of drug-loaded polymeric nanoparticles, allowing extensive modulation of their characteristics and control of their behavior at the target site. Conventionally, two groups of preparation methods can be distinguished. The first involves polymerization of monomers whereas the second is based on precipitation of preformed, well-defined natural or synthetic polymers, as for example used in salting out,

emulsion evaporation, emulsification diffusion, and solvent displacement. The choice of the nanoparticle preparation technique essentially depends on the physicochemical properties of the polymeric nanoparticle matrix material intended to be used and on the active compound to be encapsulated in the nanoparticles. One way to encapsulate the drug into the nanoparticles is accomplished by the preparation of nanoparticles in the presence of the therapeutic agent, what leads to a “homogeneous” distribution of drug within the polymer matrix. Another way to associate drug and polymer is achieved by subsequent sorption of the drug to unloaded nanoparticles either to the surface or the bulk of nanoparticles. The type of binding may also result in different release mechanisms and release rates [16, 17, 25, 26, 28, 29, 31].

Overall, the final choice of the appropriate polymer, manufacturing technique, and nanoparticle characteristics will primarily depend on the biocompatibility and degradability of the polymer, secondarily on the physicochemical characteristics of the drug, and thirdly on the therapeutic goal to be reached [31].

Owing to the advantageous drug delivery properties of polymeric nanoparticles, researchers were encouraged to find suitable application forms for pulmonary delivery. Their small size limits pulmonary deposition as nanoparticles alone are expected to be exhaled after inhalation [114]. In general, aerosol particle size is characterized by the mass median aerodynamic diameter (MMAD). The MMAD is used to describe the particle size distribution of any aerosol statistically based on the weight and size of the particles. Thus, a group of very dense particles will exhibit a larger MMAD than that of a group of less dense particles, despite an identical geometric size. It is well understood that pulmonary deposition is achieved by three principal mechanisms: inertial impaction, sedimentation, and diffusion. Impaction predominates during the passage through the oropharynx and large conducting airways if the particles possess a MMAD of  $>5\text{ }\mu\text{m}$ , or have a high velocity. Gravitational force leads to sedimentation of smaller particles (MMAD of  $<3\text{ }\mu\text{m}$ ) in the smaller airways. Additionally, sedimentation increases by breath holding. In the range below a MMAD of  $1\text{ }\mu\text{m}$ , particles are deposited by diffusion, which is based on Brownian motion. Thus, extent and efficiency of drug deposition is influenced by particle-specific and physiological factors, such as particle size and geometry, lung morphology, and breathing pattern [43, 115]. Common methods to deposit drug-loaded nanoparticles in the deeper lung are the nebulization of nanosuspensions and the aerosolization of nanoparticle-containing microparticles (composite microparticles) [21, 64, 66].

A number of nanoparticle formulations were found to be accessible for nebulization with common nebulizers [42, 105, 106, 116, 117]. One major advantage of this method is that regardless of the aerodynamic properties of the nanoparticles themselves, alveolar deposition can be easily achieved by generating adequate droplet sizes. Over the past decades, the generation of therapeutic aerosols has primarily been reserved to pneumatic- and ultrasound-driven nebulizers. Recent technological advances have led to improved

nebulizer designs employing vibrating-mesh technology for aerosol generation [40, 41]. Vibrating mesh nebulizers have been shown to overcome the main drawbacks of pneumatic- and ultrasound-driven nebulizers, that is, concentration of medicaments, temperature changes, and high residual volumes inside the nebulizer reservoir. The aggregation of nanoparticles during aerosolization is dependent on both the nanoparticle surface characteristics and the technique for aerosol generation. The aggregation tendency was reduced for nanoparticles exhibiting a more hydrophilic surface [42]. Coating of nanoparticle surfaces with hydrophilic polymers was also shown to improve the nebulization stability of biodegradable nanoparticles [105, 106]. Furthermore, the use of vibrating mesh nebulizers is suitable for the delivery of “delicate” structures, like biodegradable nanoparticles due to avoidance of high shear stress during aerosolization [118].

As an alternative to nebulization of a nanosuspension, polymeric nanoparticles can be delivered to the lung by means of dry powder aerosolization. For this reason, nanoparticles need to be encapsulated into composite microparticles using standard techniques like spray drying or agglomeration [119, 120]. The composite microparticles must display defined aerodynamic properties (MMAD) to obtain peripheral lung deposition of inhaled particles [114]. The delivery of nanoparticles as part of microparticles has been intensively investigated for several reasons. A common obstacle that limits the use of biodegradable polymeric nanoparticles is their chemical and physical instability in aqueous suspension [121, 122]. Nanoparticles tend to aggregate when stored over an extended period of time. Furthermore, hydrolytic degradation of the polymeric nanoparticle matrix material and drug leakage from nanoparticles into the aqueous medium take place. Thus, for stabilization of biodegradable polymeric nanoparticles a subsequent drying step needs to be carried out to remove water from these systems. The most commonly used methods to convert a colloidal suspension into solid powders of sufficient stability are freeze- and spray drying [123, 124]. Spray drying offers the advantage over freeze-drying that nanoparticles are transformed to respirable microparticle-containing powders in a one-step process. Freeze-drying would cause additional disintegration to form microparticles suitable for pulmonary application. The addition of stabilizers like sugars or polymers has shown to prevent unwanted nanoparticle aggregation during drying and storage [125]. Spontaneous redispersion of nanoparticles is a key desideratum in the development of successful composite drug delivery systems to the lung. Composite microparticles should release their therapeutic payload (drug-loaded nanoparticles) when they get into contact with aqueous media, and the unaffected nanoparticles can carry out their therapeutic benefit at the target site. Typical examples for preparation of composite microparticles by spray drying can be found in the literature. Drug-loaded PLGA nanoparticles and trehalose as microparticle matrix material were used to prepare composite microparticles suitable for inhalation [126]. The use of “porous nanoparticle-aggregate particles” (PNAPs) as dry powder delivery vehicles to the lung was investigated by Sung et al.. Drug-loaded PLGA nanoparticles were prepared using

a solvent evaporation method and subsequently converted to PNAPs using a spray drying technique [127]. Effervescent powder formulations containing nanoparticles were recently introduced for pulmonary drug delivery. These formulations were composed of poly(butyl cyanoacrylate) nanoparticles and as effervescent components sodium carbonate and citric acid stabilized with ammonia were employed. The active release mechanism (effervescent reaction) of the composite microparticles was observed when the carrier particles were exposed to humidity and unaffected nanoparticles were released [128].

Another interesting method to obtain nanoparticle containing microparticles is enabled by controlled agglomeration of oppositely charged nanoparticle populations. Positively- and negatively charged biodegradable nanoparticles are brought into contact under vigorous stirring, and spontaneous composite microparticle formation takes place. Nanoparticle aggregation is driven by electrostatic attraction/forces in this case [129, 130].

#### **4. Methods to Evaluate the Controlled Release Properties of Inhaled Nanoparticles**

A basic concern in the field of nanomedicine is the development of successful nanoparticulate controlled release formulations with the aim to improve the characteristics of the therapeutic agent at the target site. Biological environments are known to strongly influence the release properties of nano-sized drug delivery vehicles. An insistent problem in the development of nanoparticulate drug delivery systems is the lack of systems to follow the drug release after contact with an external medium. As a consequence, conventional *in vitro* drug release studies may have very little in common with the delivery and release situation *in vivo* and the development of more sophisticated controlled drug release carriers to the lung is precluded [31].

Different preclinical models are used to account for the drug release mechanisms, as well as the rate and extent of drug absorption after pulmonary administration [6, 32, 34]. The complexity of the employed models increases from *in vitro* cell culture methods and *in silico* models, which are primarily used as screening tools, to *in vivo* pharmacokinetic analysis that provide fundamental information about the fate of the released drug by monitoring drug levels in plasma, lung fluid, and tissue. Several cell culture models of the respiratory tract are described using both continuous and primary cells to explore drug transport mechanisms under precise experimental conditions [45, 57, 131–133]. Continuous cell cultures using alveolar or bronchial epithelial cells like A549 and Calu-3 are often employed as simple *in vitro* models for pulmonary drug delivery studies. In contrast to continuous cell cultures primary cultures consisting of alveolar epithelial cells present cell morphologies and biochemical characteristics closer to the *in vivo* situation. However, time-consuming isolation and cultivating, as well as limited cell lifetimes are the main drawbacks of primary cell culture models. The estimation of drug absorption from the respiratory tract based on physicochemical properties and permeability of drugs using

computational and experimental models led to the extension of the biopharmaceutical classification system (BCS) [134]. The pulmonary BCS (pBCS) takes into consideration the specific biology of the respiratory tract, particle deposition, and the subsequent process of drug absorption and depicts an alternative to the currently and widely used studies in animals. Drug structure-permeability relationships may contribute to reliable prediction of pulmonary pharmacokinetics used for the development of novel inhalable drugs [135]. *Ex vivo* isolated, perfused, and ventilated lung models allow the investigation of lung-specific pharmacokinetic effects on the fate of inhaled therapeutics [32–34]. These preparations maintain structural integrity of the lung tissue and allow careful control of the experimental regimen of the isolated lung. Drugs can be administered directly to the respiratory tract in a quantitative and reproducible manner, and simple sampling and analysis of perfusate provide the absorptive profile. The fundamental information about the fate of the inhaled therapeutics gained from *in vivo* pharmacokinetic analysis are accompanied by reduced screening capacity, increased expense, ethical considerations, and the potential for nonlinear dose-response relationships between the *in vitro* and *in vivo* situation as described for inhaled toxic substances [136, 137]. Overall, the application and comparison of different models to elucidate the drug behavior at the target site is needed to establish reliable *in vitro-in vivo* correlations [32, 34].

**4.1. Basic Techniques of Isolated, Perfused, and Ventilated Lung Preparations.** Isolated, perfused and ventilated lung (IPL) preparations have long been used by investigators interested in the respiratory, as well as nonrespiratory functions of this complex organ [138–141]. Recently, this technique has also been adopted to assess pulmonary pharmacokinetics of inhaled therapeutics [6, 32–34]. Areas in which IPL models have not been extensively used include the evaluation of controlled release properties of pulmonary drug delivery formulations like polymeric nanoparticles. With suitable modifications, application of IPL preparations for these investigations has become technically feasible. A schematic of an IPL using a rabbit lung is depicted in Figure 2. The basic techniques of IPL for pharmacokinetic measurements include the lung isolation, perfusion, and ventilation, the delivery of the formulation to the air-space by an appropriate method, and an adequate sample analytic. Differences between simple *in vitro* tests and intact lung models are to be expected on the basis of direct interaction of nanoparticles with their environment. Accordingly, more reliable drug release and distribution data are obtained that adequately reflect the dynamic effects occurring *in vivo* and thus enhance our knowledge on the fate of nanoparticulate drug delivery formulations at the target site [31].

The choice of an appropriate organ donor animal in IPL studies is influenced by several factors [139]. Size and airway geometry of the lung govern the selection of a particular species. Relevant anatomical and physiological characteristics, as well as respiratory parameters of appropriate organ donor animals for IPL preparations can be found in the literature [33, 34]. The most popular species

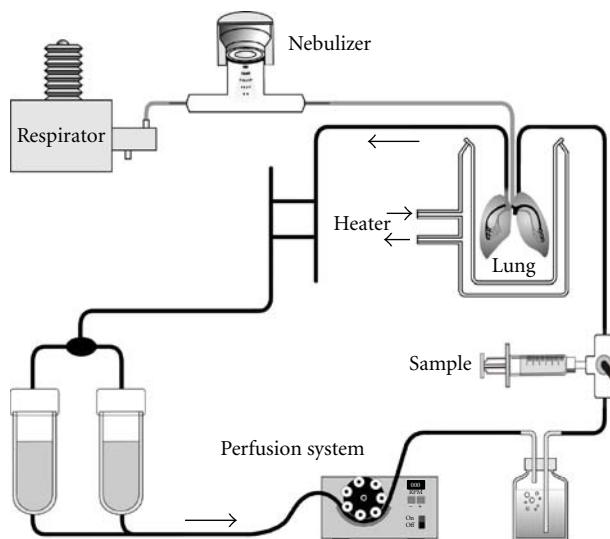


FIGURE 2: Schematic depiction of the basic arrangement of the isolated, perfused, and ventilated rabbit lung model useful for absorption and distribution studies of pulmonary-administered controlled release formulations (Modified from [106]).

have been the rat, the guinea pig, and the rabbit as donors for IPL experiments intended to assess the pulmonary pharmacokinetics of inhaled therapeutics (Table 1). Small animals have several disadvantages like tiny blood vessels that pose difficulties in surgical procedures and a lung geometry that impedes high lung deposition of therapeutic aerosols. An additional factor to be considered might be the volume and the number of perfusate samples needed for analytical tests during the course of the experiment. These difficulties are clearly overcome by using larger experimental animals having, however, the distinct disadvantage of increased animal and experimental costs.

The IPL approach has several advantages but also numerous limitations [33, 138–141]. IPL preparations offer several advantages to experimentation with animals. Perfusion experiments allow a definitive evaluation of lung-specific effects on the fate of inhaled drug substances. Experimental parameters remain controllable in IPL preparations, while in the intact animal these are likely to change with time especially in response to the administration of a drug formulation. The delivery methods for pulmonary drug administration to experimental animals are highly limited and often associated with low dosing efficiency (<10%) [164–167]. In contrast, the aerosol delivery to IPL models can be easily controlled by adjustment of the ventilation regimen [142, 165]. The release of drugs from its formulation can be monitored by sequential analysis of the (synthetic) perfusate medium. Unlike in the intact animal, it is possible to take frequent samples from the perfusate. This allows a complete qualitative and quantitative analysis of drug release from the test formulation. The determination of accurate and complete mass-balance of drugs is possible throughout the perfusion experiment.

Unlike *in vitro* cell culture, pharmacokinetic studies in *ex vivo* models display the advantage of structural and

functional integrity of the organ, for example, cell-to-cell contacts, native extracellular matrix, and pulmonary surfactant lining layer. Lung-specific factors that remain functional in perfusion studies govern drug absorption and distribution profiles and influence the final results in the intact perfused organ, and, therefore, enable a realistic extrapolation of the results to the *in vivo* situation [34].

The principal limitation imposed by IPL preparations is the comparatively short duration of study time. Long-term studies (>6 h) cannot be performed since physiological and biochemical integrity of the lung preparation deteriorates with time [139, 141, 168, 169]. Often, it is not possible to determine the effect of therapeutic agents on the lung tissue in such a short period of time. Furthermore, only *in vitro* cell culture allows detailed analysis of cellular transport processes [45, 57, 131–133].

Finally, a practical consideration is the level of expertise in all aspects of the surgical procedures, as well as in all other technical aspects required in setting up and conducting of successful perfusion experiments.

#### 4.2. Surgical Procedure for IPL Preparation: Isolation, Perfusion, and Ventilation.

The preparation of the IPL using a rabbit as organ donor animal is described briefly hereafter and interested readers are referred to excellent reviews on this topic [139–141]. In the following, the method of Seeger et al. is briefly described [141]. For lung isolation animals need to be deeply anesthetized and anticoagulated. Then a median incision is made to expose the trachea by blunt dissection, and a cannula is inserted into the trachea. Subsequently, the animals are ventilated with room air, using a respirator. After mid-sternal thoracotomy, the ribs are spread, the right ventricle is incised, and a fluid-filled perfusion catheter is immediately placed into the pulmonary artery. Immediately after insertion of the catheter, perfusion with cold buffer fluid is started, and the heart is then cut open at the apex. Next, the trachea, lungs, and heart are excised *en bloc* from the thoracic cage. A second perfusion catheter with a bent cannula is introduced via the left ventricle into the left atrium and is fixed in this position. After rinsing the lungs with buffer fluid for washout of blood, the perfusion circuit is closed for recirculation. Meanwhile, the flow is slowly increased, and left atrial pressure is set to 1.5 mmHg. In parallel with the onset of artificial perfusion, ventilation is changed (5% CO<sub>2</sub>, 16% O<sub>2</sub>, and 79% N<sub>2</sub>) to maintain the pH of the recirculating buffer at 7.4. Tidal volume is 10 ml/kg body weight with a frequency of 30 strokes/min. The IPL is placed in a temperature-equilibrated housing chamber (37°C), freely suspended from a force transducer for continuous monitoring of organ weight [170]. Pressures in the pulmonary artery, the left atrium, and the trachea are registered by means of small-diameter tubing threaded into the perfusion catheters and the trachea and connected to pressure transducers. Only lungs that have a homogeneous white appearance with no signs of hemostasis, edema, or atelectasis, a constant mean pulmonary artery and peak ventilation pressure in the normal range (4–10 and 5–8 mmHg, resp.), and are isogravimetric during an initial

TABLE 1: Typical examples of pulmonary drug delivery studies employing isolated, perfused, and ventilated lung models.

Organ donor animal	Perfusion system	Ventilation system	Drug/formulation	Formulation application	Analytics	References
Rat	Recirculating flow, 15 mL/min; Krebs-Ringer/Krebs-Henseleit buffer + 4% BSA	Alternating “negative” pressure; tidal volume: ~1 mL, ventilation frequency: 7–28 strokes/min	Fluorescent dyes, labeled dextrans, polypeptides (polyaspartamide, insulin); solution	“Forced solution instillation”	Fluorescence spectroscopy, ELISA	[142–152]
	Recirculating or single-pass flow, 7–11 mL/min; Krebs-Ringer buffer + 4.5% BSA	Alternating “negative” pressure; tidal volume: ~1 mL, ventilation frequency: 70 strokes/min	Budesonide; solution	Instillation	HPLC, liquid scintillation counting	[153]
	Recirculating flow, 5 mL/min; Krebs-Henseleit buffer + 3% BSA	“Positive” pressure inflation; tidal volume: 2, 4 mL, ventilation frequency: 60, 30 strokes/min	Levofloxacin; solution	Nebulization	HPLC	[154]
	Single-pass flow, ~17 mL/min; Krebs-Ringer buffer + 2% BSA	Alternating “negative” pressure; tidal volume: ~1 mL, ventilation frequency: 75 strokes/min	Budesonide, formoterol, terbutaline; powder	Powder aerosolization (DustGun® technology)	LC-MS/MS	[155]
	Recirculating flow, 10–12 mL/min; Krebs-Ringer buffer + 4.5% BSA	Alternating “negative” pressure; tidal volume: ~1 mL, ventilation frequency: 80 strokes/min	Diverse low molecular weight therapeutic agents, labelled dextrans, oligopeptides; solution	Nebulization, instillation (Aeroprobe® technology)	Fluorescence spectroscopy, LC-MS/MS	[156, 157]
Guinea pig	Single-pass flow, Guinea pig 10 mL/min; Krebs-Ringer buffer + 4.5% BSA	Alternating “negative” pressure; tidal volume: ~2 mL, ventilation frequency: 80 strokes/min	Xanthines; solution	Instillation	liquid scintillation counting	[158]
	Recirculating flow, 100 mL/min; Krebs-Henseleit buffer (+ 4% hydroxyethyl-amylopectine)	“Positive” pressure inflation; tidal volume: 30 mL, ventilation frequency: 30 strokes/min	Fluorescent dyes, salbutamol, iloprost; solution, nanosuspension	Nebulization, instillation	Fluorescence spectroscopy; HPLC; RIA	[106, 159–161]
	Recirculating flow; Krebs-Ringer buffer + 4.5% BSA	Alternating “negative” pressure	Isoproterenol, isoproterenol prodrugs; solution	Nebulization, instillation	HPLC	[162, 163]

BSA: bovine serum albumin; ELISA: enzyme-linked immunosorbent assay; HPLC: high-pressure liquid chromatography; LC-MS/MS: liquid chromatography-tandem mass spectrometry; RIA: radioimmunoassay.

steady state period of at least 30 min are considered for experiments.

A number of visual and physiological parameters can be determined to ascertain the viability of the IPL preparation [139, 171]. Under optimized preparation and perfusion conditions, greater than 85% of all excised lungs fulfill these criteria, and lungs may be perfused for ~6 h without changes in physiological aspects [141, 168, 169].

For analysis of pulmonary pharmacokinetics of inhaled therapeutics, such as pulmonary absorption and distribution characteristics, formulations need to be delivered to the IPL by the intratracheal route. Intratracheal delivery can be carried out by dry powder insufflation or inhalation or by means of fluid instillation or nebulization [32–34]. For nebulization purpose, a nebulizer unit is connected to the inspiratory tubing between the ventilator and the lung to pass the produced aerosol through by the inspiration gas [106, 159]. In order to determine the absorption of drug from the lung into the perfusate, samples are taken from the venous part of the system (Figure 2). Additionally, the analysis of the drug distribution characteristics to the different compartments of the lung is performed by lavage for the amount of drug remaining in the lung-lining fluid and by extraction or microscopic techniques for the amount of drug remaining in the lung tissue at the end of the experiment.

**4.3. Application of Drug Formulations to the IPL.** The choice of an appropriate IPL preparation set-up for the analysis of the fate of inhaled therapeutics at the target site is influenced by several factors. The particular problem determines the selection of experimental parameters like ventilation method, perfusion characteristic, and perfusate type [139, 140]. The ventilation of the IPL can be realized by two modes, namely, “positive” pressure and “negative” (subatmospheric) pressure ventilation. During “positive” pressure ventilation a connection of a respirator directly to the lung, which pushes bolus volumes of air into the lung, is required. Subatmospheric pressure ventilation is accomplished by using a reverse connected respirator to cycle subatmospheric pressures inside the chamber in which the lung is suspended. While “negative” pressure ventilation is generally preferred for drug absorption and distribution studies (Table 1), as it prevents water loss, tissue drying, and improves organ viability (i.e., reduced risk of architecture destruction by overinflation with subsequent edema formation and progressive atelectasis), “positive” pressure ventilation enables a highly efficient and homogeneous deposition of therapeutic aerosols to the isolated lung as described above [33, 106, 140, 159]. Beside the morphology of the respiratory tract, ventilation pattern is generally recognized to have a high impact for the successful aerosol delivery to isolated lungs. To avoid low dosing efficiency and nonreproducible aerosol deposition pattern in the lung, a synchronization of aerosol application and inspiration needs to be adjusted (tidal volume ↑, ventilation frequency ↓) [142, 165].

The applied perfusion technique is dependent on the experimental design [32, 33, 140]. The perfusion may be performed in a single-pass or recirculating manner. Single-

pass perfusion systems have the advantage of being less sophisticated; however, depending on the flow rate and the duration of the experiment, they come along with higher consumption of perfusate. Moreover, a sensitive sample analytics is required [155]. In pharmacokinetic experiments of inhaled therapeutics, the use of artificial perfusion medium, for example Krebs-Henseleit buffer fluid, with addition of hydroxyethylamylopectin or dextran as oncotic agent is only appropriate for hydrophilic drug substances. Hydrophobic drug analysis is relieved in the presence of albumin owing to binding of hydrophobic compounds. For example, Liu et al. investigated the effect of different perfusion buffers on the pharmacokinetics of several drugs with distinct physicochemical properties that were administered to the circulation of an isolated rat lung model [172]. The total recovery of the lipophilic drug propranolol was found to be significantly decreased when dextran was used as oncotic agent instead of albumin. Moreover, the measurement of pulmonary disposition of the potent glucocorticoid budesonide after administration to the air-space or the pulmonary circulation of the isolated rat lung was only feasible in the presence of 4.5% albumin in the perfusion medium [153]. These studies emphasize the use of albumin as oncotic agent in perfusion buffers when the pulmonary disposition of hydrophobic drugs is under investigation. In addition, depending on the experimental design, heparinized animal plasma may be added to the buffer fluid (10–15%). Use of heparinized animal blood as perfusion fluid most closely resembles the *in vivo* state. However, analysis of drugs and interpretation of results are rendered much more difficult by the presence of such a “complex” perfusion medium, thereby negating some of the advantages of the isolated lung technique [140, 141].

The use of IPL preparations to study the lung disposition of several inhaled therapeutics was pioneered by Byron et al. and Ryrfeldt et al. in the mid 1980’s (Table 1) [32, 33]. The pulmonary absorption and distribution of low molecular and high molecular weight drugs was addressed in several studies [143–152]. Ryrfeldt et al. investigated the pulmonary disposition of the glucocorticoid budesonide in an isolated rat lung after instillation [153]. The drug absorption from the air-space into the perfusate was characterized by two distinct phases: after a rapid initial absorption phase about half of the instilled dose was slowly transferred into the perfusate. This study points out the high lung affinity of budesonide, no biotransformation of this compound was found in the lung. The high affinity to the lung together with an absence of lung metabolism was shown to be an important factor to explain the clinical benefits seen with budesonide [80, 81]. Kröll et al. used the isolated guinea pig lung model for the measurement of the pulmonary fate of two antiasthmatic drugs (xanthines) [158]. After intratracheal instillation of theophylline, the peak concentration in the lung perfusate appeared within a short period of time, and after 10 and 60 minutes, ~68 and ~87% of the given dose had been absorbed, respectively. The rapid disappearance of locally administered theophylline may explain the lack of success of inhalation therapy with this therapeutic agent.

The pulmonary disposition of the antibiotic levofloxacin was evaluated after systemic application and inhalation in a model of the isolated rat lung. Different experimental conditions including higher or lower respiratory frequency with lower or higher tidal volume were tested. Comparison of systemic and pulmonary administration revealed statistically significant differences between partition coefficients showing much higher values for the latter route. Thus, inhalation compared to systemic administration improves levofloxacin access to the lung tissue [154].

Only limited information is available regarding the administration, deposition, and absorption of dry powder aerosols to IPL preparations. For this purpose, Ewing et al. and Byron et al. established an isolated rat lung model and reported the absorption profiles of a variety of test compounds [143, 155]. Using the recently developed DustGun aerosol technology, Ewing et al. exposed the IPL model to respirable dry powder aerosols of three drugs at high concentrations [155]. Other interesting techniques for reproducible aerosol application to IPL preparations include the miniaturized nebulization catheter (AeroProbe) and the “forced solution instillation” technique [142, 165].

Lahnstein et al. investigated the pulmonary absorption and distribution of fluorescent dyes in an isolated rabbit lung model [159]. Three structurally diverse probes were administered intrapulmonary by nebulization of dye solutions. The authors found that the absorption of the model compounds from the air-space into the perfusate was mainly affected by the physicochemical properties (octanol/water partition coefficient) of the employed dyes. While for the hydrophobic dye only a marginal appearance in the perfusate was observed due to accumulation in the lung tissue, a rapid increase in perfusate concentration (with stable plateau concentration) was obtained for both hydrophilic dyes.

Rapid absorption and capacity-limited metabolism of isoproterenol and prodrugs thereof were observed following intrabronchial and aerosol administration of drug to the isolated rabbit lung [162, 163].

The IPL preparation is a valuable model for the analysis of pharmacokinetic profiles of pulmonary administered drugs. Upgrading of the *ex vivo* models to pharmacodynamic investigations has recently become technically feasible. As an example, the pharmacokinetics and vasodilatory effect of nebulized iloprost were investigated in a model of experimental pulmonary hypertension employing the isolated rabbit lung [160]. The nebulization of different amounts of iloprost caused a dose-dependent pulmonary vasodilatation. In addition, a similar dose-dependent appearance of iloprost in the recirculating perfusate was noted.

The effect of polymeric nanoparticles on the microvascular permeability and translocation across the alveolar barrier was tested in isolated rabbit lungs after nanoparticle instillation [173, 174]. The increase in pulmonary microvascular permeability was related to the number of administered nanoparticles. Moreover, positively charged nanoparticles were more effective in the microvascular permeability response than negatively charged nanoparticles. The authors concluded that the surface properties and the total surface area need to be considered to interpret the changes of

the microvascular permeability upon nanoparticle challenge. The applied polymeric nanoparticles were mainly located in the alveolar space and in macrophages after instillation, and no translocation of nanoparticles from the alveoli into the perfusion medium was observed. However, the relevance of these findings for the *in vivo* translocation of inhaled ultrafine particles remains to be established, owing to the fact that polymeric nanoparticles are currently under investigation as potential drug delivery systems to the lung [95].

Beck-Broichsitter et al. compared the pulmonary disposition characteristics of the hydrophilic model drug 5(6)-carboxyfluorescein after aerosolization as solution or entrapped into polymeric nanoparticles in an isolated rabbit lung model [106]. Nanoparticles were of spherical shape with a mean particle size of ~200 nm. Nebulization of the nanosuspension using a vibrating mesh nebulizer led to negligible changes of nanoparticle properties. The drug release *in vitro* was fast. Nevertheless, after deposition of equal amounts of 5(6)-carboxyfluorescein in the isolated rabbit lung model, less 5(6)-carboxyfluorescein was detected in the perfusate for loaded nanoparticles (~10 ng/ml) when compared to 5(6)-carboxyfluorescein aerosolized from solution (~18 ng/ml).

Although IPL studies are conducted with an intact organ close to the physiological state, it is to a large extent unresolved if pharmacokinetic data obtained from IPL preparations are consistent with that measured *in vivo* [32, 33]. Recently, a linear relationship between the drug absorption kinetics of diverse low molecular weight drugs (<700 g/mol) in a vertically positioned IPL system and from the lung *in vivo* was demonstrated [156, 175]. Moreover, drugs for which air-to-perfusate absorption kinetics were evaluated *ex vivo* and *in vivo* were also tested in epithelial cell culture models (Caco-2 and 16HBE14o) regarding their transport characteristics. Permeability in intestinal and airway cell culture models were found to be in excellent agreement with the physicochemical properties of the investigated drugs, as well as the rate of absorption measured in the IPL [156, 157, 176]. The absence of a bronchial circulation in horizontally positioned IPL preparations and therefore a lack of tracheobronchial absorption pathways have been attributed as the likely cause of a substantial difference in the absorption kinetics of low molecular weight drugs between the IPL preparation and *in vivo*. The absorption of low molecular weight drugs *in vivo* takes place from alveolar, as well as tracheobronchial regions at effective and comparable rates. As a result, the IPL preparation underestimates the absorption of low molecular weight drugs compared to the *in vivo* situation. However, macromolecules show poor to insignificant absorption across the thicker tracheobronchial membranes and thus, the absorption profiles of macromolecules derived from IPL preparations have been reported as statistically indistinguishable from those obtained *in vivo* [32, 149]. Clearly, studies regarding the difference between the vertically and horizontally positioned IPL systems on drug absorption need to be carried out.

In recent studies, the development and performance of a novel nanoparticle-based formulation for pulmonary

delivery of salbutamol has been characterized systematically through all steps beginning from the particle preparation process, over the *in vitro* testing of drug release, drug transport in cell culture, pulmonary absorption, and distribution characteristics in an isolated rabbit lung model, to *in vivo* bronchoprotection studies in anaesthetized guinea pigs. Sustained salbutamol release from the drug-loaded nanoparticles was observed for 2.5 h *in vitro*. Drug transport experiments conducted with primary cultured human alveolar epithelial cells revealed a delayed transport of salbutamol across the cell monolayer for nanoparticle formulations. In parallel, a sustained salbutamol release profile was observed after aerosol delivery of nanoparticles to the IPL as reflected by a distinct absorption profile and lower salbutamol recovery in the perfusate (~40%) when compared to salbutamol solution (~63%). Moreover, a prolonged pharmacological effect was observed for 120 min *in vivo* when salbutamol-loaded nanoparticles were administered to guinea pigs [161, 177]. Overall, these results demonstrate good agreement between *in vitro*, *ex vivo*, and *in vivo* tests, serve as examples for the potential of the IPL to be used to predict drug absorption from the intact animal and, therefore, present a solid basis for future advancement in nanomedicine strategies for pulmonary drug delivery.

## 5. Conclusion and Perspective

Implementation of nanotechnology offers new concepts for development of optimized therapeutic and diagnostic tools in medicine. Biodegradable polymeric nanoparticles hold great promise to improve controlled and targeted drug delivery to the desired site of action. Various nanoparticle-containing formulations for drug delivery to the lung are currently under investigation. Existing analytical protocols allow the accurate analysis of the physicochemical properties of these drug delivery systems, but a lack of methods that elucidate the controlled release properties of polymeric nanoparticles constrict the development of improved drug-delivery vehicles. Isolated, perfused, and ventilated lung models are promising tools to evaluate the controlled release characteristics of nanoparticles intended for pulmonary application. *Ex vivo* models allow the determination of the fate of nanoparticulate drug delivery formulations at the target site. As a consequence, more reliable drug release and distribution data are obtained that adequately reflect the dynamic effects occurring *in vivo*. The first promising results that were made by the analysis of the release properties of drug-loaded polymeric nanoparticles by the *ex vivo* technique emphasize this strategy and will hopefully promote progress in nanomedicine.

## Acknowledgment

The authors want to express their sincere thanks to the German Research Foundation (DFG) for financial support.

## References

- [1] G. Taylor and I. Kellaway, "Pulmonary drug delivery," in *Drug Delivery and Targeting*, A. Hillery, A. W. Lloyd, and J. Swabrick, Eds., pp. 269–300, Routledge Chapman & Hall, London, UK, 2001.
- [2] H. Bisgaard, C. O'Callaghan, and G. C. Smaldone, Eds., *Drug Delivery to the Lung*, Informa Healthcare, New York, NY, USA, 2002.
- [3] H. M. Courrier, N. Butz, and TH. F. Vandamme, "Pulmonary drug delivery systems: recent developments and prospects," *Critical Reviews in Therapeutic Drug Carrier Systems*, vol. 19, no. 4-5, pp. 425–498, 2002.
- [4] D. A. Groneberg, C. Witt, U. Wagner, K. F. Chung, and A. Fischer, "Fundamentals of pulmonary drug delivery," *Respiratory Medicine*, vol. 97, no. 4, pp. 382–387, 2003.
- [5] T. Gessler, W. Seeger, and T. Schmehl, "Inhaled prostaglandins in the therapy of pulmonary hypertension," *Journal of Aerosol Medicine*, vol. 21, no. 1, pp. 1–12, 2008.
- [6] C. Mobley and G. Hochhaus, "Methods used to assess pulmonary deposition and absorption of drugs," *Drug Discovery Today*, vol. 6, no. 7, pp. 367–375, 2001.
- [7] N. R. Labiris and M. B. Dolovich, "Pulmonary drug delivery. Part I: physiological factors affecting therapeutic effectiveness of aerosolized medications," *British Journal of Clinical Pharmacology*, vol. 56, no. 6, pp. 588–599, 2003.
- [8] N. R. Labiris and M. B. Dolovich, "Pulmonary drug delivery. Part II: the role of inhalant delivery devices and drug formulations in therapeutic effectiveness of aerosolized medications," *British Journal of Clinical Pharmacology*, vol. 56, no. 6, pp. 600–612, 2003.
- [9] X. M. Zeng, G. P. Martin, and C. Marriott, "The controlled delivery of drugs to the lung," *International Journal of Pharmaceutics*, vol. 124, no. 2, pp. 149–164, 1995.
- [10] J. G. Hardy and T. S. Chadwick, "Sustained release drug delivery to the lungs. An option for the future," *Clinical Pharmacokinetics*, vol. 39, no. 1, pp. 1–4, 2000.
- [11] Y. Xie, P. Zeng, and T. S. Wiedmann, "Disease guided optimization of the respiratory delivery of microparticulate formulations," *Expert Opinion on Drug Delivery*, vol. 5, no. 3, pp. 269–289, 2008.
- [12] R. Langer, "New methods of drug delivery," *Science*, vol. 249, no. 4976, pp. 1527–1533, 1990.
- [13] R. Langer, "Drug delivery and targeting," *Nature*, vol. 392, no. 6679, supplement, pp. 5–10, 1998.
- [14] D. A. La Van, D. M. Lynn, and R. Langer, "Moving smaller in drug discovery and delivery," *Nature Reviews Drug Discovery*, vol. 1, no. 1, pp. 77–84, 2002.
- [15] O. C. Farokhzad and R. Langer, "Impact of nanotechnology on drug delivery," *ACS Nano*, vol. 3, no. 1, pp. 16–20, 2009.
- [16] B. Mishra, B. B. Patel, and S. Tiwari, "Colloidal nanocarriers: a review on formulation technology, types and applications toward targeted drug delivery," *Nanomedicine*, vol. 6, no. 1, pp. e9–e24, 2010.
- [17] K. S. Soppimath, T. M. Aminabhavi, A. R. Kulkarni, and W. E. Rudzinski, "Biodegradable polymeric nanoparticles as drug delivery devices," *Journal of Controlled Release*, vol. 70, no. 1–2, pp. 1–20, 2001.
- [18] J. Panyam and V. Labhasetwar, "Biodegradable nanoparticles for drug and gene delivery to cells and tissue," *Advanced Drug Delivery Reviews*, vol. 55, no. 3, pp. 329–347, 2003.
- [19] O. M. Koo, I. Rubinstein, and H. Onyuksel, "Role of nanotechnology in targeted drug delivery and imaging: a concise review," *Nanomedicine*, vol. 1, no. 3, pp. 193–212, 2005.
- [20] P. G. A. Rogueda and D. Traini, "The nanoscale in pulmonary delivery. Part 1: deposition, fate, toxicology and effects,"

- Expert Opinion on Drug Delivery*, vol. 4, no. 6, pp. 595–606, 2007.
- [21] P. G. A. Rogueda and D. Traini, “The nanoscale in pulmonary delivery. Part 2: formulation platforms,” *Expert Opinion on Drug Delivery*, vol. 4, no. 6, pp. 607–620, 2007.
- [22] S. Azarmi, W. H. Roa, and R. Löbenberg, “Targeted delivery of nanoparticles for the treatment of lung diseases,” *Advanced Drug Delivery Reviews*, vol. 60, no. 8, pp. 863–875, 2008.
- [23] E. Rytting, J. Nguyen, X. Wang, and T. Kissel, “Biodegradable polymeric nanocarriers for pulmonary drug delivery,” *Expert Opinion on Drug Delivery*, vol. 5, no. 6, pp. 629–639, 2008.
- [24] T. Lebhardt, S. Roesler, M. Beck-Broichsitter, and T. Kissel, “Polymeric nanocarriers for drug delivery to the lung,” *Journal of Drug Delivery Science and Technology*, vol. 20, no. 3, pp. 171–180, 2010.
- [25] C. Vauthier and K. Bouchemal, “Methods for the preparation and manufacture of polymeric nanoparticles,” *Pharmaceutical Research*, vol. 26, no. 5, pp. 1025–1058, 2009.
- [26] C. E. Mora-Huertas, H. Fessi, and A. Elaissari, “Polymer-based nanocapsules for drug delivery,” *International Journal of Pharmaceutics*, vol. 385, no. 1-2, pp. 113–142, 2010.
- [27] J. M. Anderson and M. S. Shive, “Biodegradation and biocompatibility of PLA and PLGA microspheres,” *Advanced Drug Delivery Reviews*, vol. 28, no. 1, pp. 5–24, 1997.
- [28] I. Bala, S. Hariharan, and M. N. V. R. Kumar, “PLGA nanoparticles in drug delivery: the state of the art,” *Critical Reviews in Therapeutic Drug Carrier Systems*, vol. 21, no. 5, pp. 387–422, 2004.
- [29] C. E. Astete and C. M. Sabliov, “Synthesis and characterization of PLGA nanoparticles,” *Journal of Biomaterials Science, Polymer Edition*, vol. 17, no. 3, pp. 247–289, 2006.
- [30] C. Washington, “Drug release from microdisperse systems: a critical review,” *International Journal of Pharmaceutics*, vol. 58, no. 1, pp. 1–12, 1990.
- [31] J. Kreuter, *Colloidal Drug Delivery Systems*, Marcel Dekker, New York, NY, USA, 1994.
- [32] M. Sakagami, “In vivo, in vitro and ex vivo models to assess pulmonary absorption and disposition of inhaled therapeutics for systemic delivery,” *Advanced Drug Delivery Reviews*, vol. 58, no. 9-10, pp. 1030–1060, 2006.
- [33] A. Tronde, C. Bosquillon, and B. Forbes, “The isolated perfused lung for drug absorption studies,” in *Biotechnology Pharmaceutical Aspects VII*, C. Erhardt and K. J. Kim, Eds., vol. 7 of *Drug Absorption Studies*, pp. 135–163, Springer, Berlin, Germany, 2008.
- [34] C. A. Fernandes and R. Vanbever, “Preclinical models for pulmonary drug delivery,” *Expert opinion on drug delivery*, vol. 6, no. 11, pp. 1231–1245, 2009.
- [35] J. Kreuter, “Nanoparticles-a historical perspective,” *International Journal of Pharmaceutics*, vol. 331, no. 1, pp. 1–10, 2007.
- [36] D. Peer, J. M. Karp, S. Hong, O. C. Farokhzad, R. Margalit, and R. Langer, “Nanocarriers as an emerging platform for cancer therapy,” *Nature Nanotechnology*, vol. 2, no. 12, pp. 751–760, 2007.
- [37] M. J. Hawkins, P. Soon-Shiong, and N. Desai, “Protein nanoparticles as drug carriers in clinical medicine,” *Advanced Drug Delivery Reviews*, vol. 60, no. 8, pp. 876–885, 2008.
- [38] M. Bur, A. Henning, S. Hein, M. Schneider, and C. M. Lehr, “Inhalative nanomedicine—opportunities and challenges,” *Inhalation Toxicology*, vol. 21, supplement 1, pp. 137–143, 2009.
- [39] I. Roy and N. Vij, “Nanodelivery in airway diseases: challenges and therapeutic applications,” *Nanomedicine*, vol. 6, no. 2, pp. 237–244, 2010.
- [40] R. Dhand, “Nebulizers that use a vibrating mesh or plate with multiple apertures to generate aerosol,” *Respiratory Care*, vol. 47, no. 12, pp. 1406–1416, 2002.
- [41] J. C. Waldrep and R. Dhand, “Advanced nebulizer designs employing vibrating mesh/aperture plate technologies for aerosol generation,” *Current Drug Delivery*, vol. 5, no. 2, pp. 114–119, 2008.
- [42] L. A. Dailey, T. Schmehl, T. Gessler et al., “Nebulization of biodegradable nanoparticles: impact of nebulizer technology and nanoparticle characteristics on aerosol features,” *Journal of Controlled Release*, vol. 86, no. 1, pp. 131–144, 2003.
- [43] W. C. Hinds, *Aerosol Technology: Properties, Behavior, and Measurements of Airborne Particles*, John Wiley & Sons, New York, NY, USA, 1999.
- [44] J. D. Crapo, B. E. Barry, P. Gehr, M. Bachofen, and E. R. Weibel, “Cell number and cell characteristics of the normal human lung,” *American Review of Respiratory Disease*, vol. 126, no. 2, pp. 332–337, 1982.
- [45] B. Forbes and C. Ehrhardt, “Human respiratory epithelial cell culture for drug delivery applications,” *European Journal of Pharmaceutics and Biopharmaceutics*, vol. 60, no. 2, pp. 193–205, 2005.
- [46] E. R. Weibel, Ed., *Morphometry of the Human Lung*, Springer, Berlin, Germany, 1963.
- [47] C. M. Evans and J. A. S. Koo, “Airway mucus: the good, the bad, the sticky,” *Pharmacology and Therapeutics*, vol. 121, no. 3, pp. 332–348, 2009.
- [48] C. Marriott, “Mucus and mucociliary clearance in the respiratory tract,” *Advanced Drug Delivery Reviews*, vol. 5, no. 1-2, pp. 19–35, 1990.
- [49] A. B. Lansley, “Mucociliary clearance and drug delivery via the respiratory tract,” *Advanced Drug Delivery Reviews*, vol. 11, no. 3, pp. 299–327, 1993.
- [50] L. A. J. M. Creuwels, L. M. G. Van Golde, and H. P. Haagsman, “The pulmonary surfactant system: biochemical and clinical aspects,” *Lung*, vol. 175, no. 1, pp. 1–39, 1997.
- [51] J. Goerke, “Pulmonary surfactant: functions and molecular composition,” *Biochimica et Biophysica Acta*, vol. 1408, no. 2-3, pp. 79–89, 1998.
- [52] R. Veldhuizen, K. Nag, S. Orgeig, and F. Possmayer, “The role of lipids in pulmonary surfactant,” *Biochimica et Biophysica Acta*, vol. 1408, no. 2-3, pp. 90–108, 1998.
- [53] J. Pérez-Gil and K. M. W. Keough, “Interfacial properties of surfactant proteins,” *Biochimica et Biophysica Acta*, vol. 1408, no. 2-3, pp. 203–217, 1998.
- [54] R. Wüstneck, J. Perez-Gil, N. Wüstneck, A. Cruz, V. B. Fainerman, and U. Pison, “Interfacial properties of pulmonary surfactant layers,” *Advances in Colloid and Interface Science*, vol. 117, no. 1-3, pp. 33–58, 2005.
- [55] J. Pérez-Gil, “Structure of pulmonary surfactant membranes and films: the role of proteins and lipid-protein interactions,” *Biochimica et Biophysica Acta*, vol. 1778, no. 7-8, pp. 1676–1695, 2008.
- [56] H. Fehrenbach, “Alveolar epithelial type II cell: defender of the alveolus revisited,” *Respiratory Research*, vol. 2, no. 1, pp. 33–46, 2001.
- [57] M. Ehrhardt, M. Laue, and K. J. Kim, “In vitro models of the alveolar epithelial barrier,” in *Biotechnology Pharmaceutical*

- Aspects VII*, C. Erhardt and K. J. Kim, Eds., Drug Absorption Studies, pp. 258–282, Springer, Berlin, Germany, 2008.
- [58] J. S. Patton, “Mechanisms of macromolecule absorption by the lungs,” *Advanced Drug Delivery Reviews*, vol. 19, no. 1, pp. 3–36, 1996.
- [59] M. Gumbleton, “Caveolae as potential macromolecule trafficking compartments within alveolar epithelium,” *Advanced Drug Delivery Reviews*, vol. 49, no. 3, pp. 281–300, 2001.
- [60] J. D. Brain, “Mechanisms, measurement, and significance of lung macrophage function,” *Environmental Health Perspectives*, vol. 97, pp. 5–10, 1992.
- [61] A. Palecanda and L. Kobzik, “Receptors for unopsonized particles: the role of alveolar macrophage scavenger receptors,” *Current Molecular Medicine*, vol. 1, no. 5, pp. 589–595, 2001.
- [62] J. Yu and Y. W. Chien, “Pulmonary drug delivery: physiologic and mechanistic aspects,” *Critical Reviews in Therapeutic Drug Carrier Systems*, vol. 14, no. 4, pp. 395–453, 1997.
- [63] U. Pison, T. Welte, M. Giersig, and D. A. Groneberg, “Nanomedicine for respiratory diseases,” *European Journal of Pharmacology*, vol. 533, no. 1–3, pp. 341–350, 2006.
- [64] J. C. Sung, B. L. Pulliam, and D. A. Edwards, “Nanoparticles for drug delivery to the lungs,” *Trends in Biotechnology*, vol. 25, no. 12, pp. 563–570, 2007.
- [65] M. Smola, T. Vandamme, and A. Sokolowski, “Nanocarriers as pulmonary drug delivery systems to treat and to diagnose respiratory and non respiratory diseases,” *International Journal of Nanomedicine*, vol. 3, no. 1, pp. 1–19, 2008.
- [66] W. Yang, J. I. Peters, and R. O. Williams, “Inhaled nanoparticles. A current review,” *International Journal of Pharmaceutics*, vol. 356, no. 1–2, pp. 239–247, 2008.
- [67] M. M. Bailey and C. J. Berkland, “Nanoparticle formulations in pulmonary drug delivery,” *Medicinal Research Reviews*, vol. 29, no. 1, pp. 196–212, 2009.
- [68] H. M. Mansour, Y. S. Rhee, and X. Wu, “Nanomedicine in pulmonary delivery,” *International journal of nanomedicine*, vol. 4, pp. 299–319, 2009.
- [69] G. Oberdörster, E. Oberdörster, and J. Oberdörster, “Nanotoxicology: an emerging discipline evolving from studies of ultrafine particles,” *Environmental Health Perspectives*, vol. 113, no. 7, pp. 823–839, 2005.
- [70] M. S. Cartiera, K. M. Johnson, V. Rajendran, M. J. Caplan, and W. M. Saltzman, “The uptake and intracellular fate of PLGA nanoparticles in epithelial cells,” *Biomaterials*, vol. 30, no. 14, pp. 2790–2798, 2009.
- [71] J. S. Patton and R. M. Platz, “Pulmonary delivery of peptides and proteins for systemic action,” *Advanced Drug Delivery Reviews*, vol. 8, no. 2–3, pp. 179–196, 1992.
- [72] P. R. Byron and J. S. Patton, “Drug delivery via the respiratory tract,” *Journal of Aerosol Medicine*, vol. 7, no. 1, pp. 49–75, 1994.
- [73] R. W. Niven, “Delivery of biotherapeutics by inhalation aerosol,” *Critical Reviews in Therapeutic Drug Carrier Systems*, vol. 12, no. 2–3, pp. 151–231, 1995.
- [74] R. U. Agu, M. I. Ugwoke, M. Armand, R. Kinget, and N. Verbeke, “The lung as a route for systemic delivery of therapeutic proteins and peptides,” *Respiratory Research*, vol. 2, no. 4, pp. 198–209, 2001.
- [75] G. Scheuch, M. J. Kohlhaeuf, P. Brand, and R. Siekmeier, “Clinical perspectives on pulmonary systemic and macromolecular delivery,” *Advanced Drug Delivery Reviews*, vol. 58, no. 9–10, pp. 996–1008, 2006.
- [76] J. S. Patton and P. R. Byron, “Inhaling medicines: delivering drugs to the body through the lungs,” *Nature Reviews Drug Discovery*, vol. 6, no. 1, pp. 67–74, 2007.
- [77] R. Siekmeier and G. Scheuch, “Systemic treatment by inhalation of macromolecules—principles, problems, and examples,” *Journal of Physiology and Pharmacology*, vol. 59, no. 6, pp. 53–79, 2008.
- [78] C. Bailey and A. Barnett, “Why is Exubera being withdrawn?” *British Medical Journal*, vol. 335, no. 7630, p. 1156, 2007.
- [79] J. Kling, “Inhaled insulin’s last gasp?” *Nature Biotechnology*, vol. 26, no. 5, pp. 479–480, 2008.
- [80] T. Volsko and M. D. Reed, “Drugs used in the treatment of asthma: a review of clinical pharmacology and aerosol drug delivery,” *Respiratory care clinics of North America*, vol. 6, no. 1, pp. 41–55, 2000.
- [81] D. D. Sin and S. F. Paul Man, “Inhaled corticosteroids in the long-term management of patients with chronic obstructive pulmonary disease,” *Drugs and Aging*, vol. 20, no. 12, pp. 867–880, 2003.
- [82] T. Gessler, T. Schmehl, H. Olschewski, F. Grimminger, and W. Seeger, “Aerosolized vasodilators in pulmonary hypertension,” *Journal of Aerosol Medicine*, vol. 15, no. 2, pp. 117–122, 2002.
- [83] H. Olschewski, G. Simonneau, N. Galie et al., “Inhaled iloprost for severe pulmonary hypertension,” *New England Journal of Medicine*, vol. 347, no. 5, pp. 322–329, 2002.
- [84] A. R. Clark, “Medical aerosol inhalers: past, present, and future,” *Aerosol Science and Technology*, vol. 22, no. 4, pp. 374–391, 1995.
- [85] I. Gonda, “The ascent of pulmonary drug delivery,” *Journal of Pharmaceutical Sciences*, vol. 89, no. 7, pp. 940–945, 2000.
- [86] P. J. Anderson, “History of aerosol therapy: liquid nebulization to MDIs to DPIs,” *Respiratory Care*, vol. 50, no. 9, pp. 1139–1150, 2005.
- [87] D. E. Geller, “Comparing clinical features of the nebulizer, metered-dose inhaler, and dry powder inhaler,” *Respiratory Care*, vol. 50, no. 10, pp. 1313–1321, 2005.
- [88] S. P. Newman, “Principles of metered-dose inhaler design,” *Respiratory Care*, vol. 50, no. 9, pp. 1177–1190, 2005.
- [89] P. J. Atkins, “Dry powder inhalers: an overview,” *Respiratory Care*, vol. 50, no. 10, pp. 1304–1312, 2005.
- [90] J. B. Fink, “Metered-dose inhalers, dry powder inhalers, and transitions,” *Respiratory Care*, vol. 45, no. 6, pp. 623–635, 2000.
- [91] P. P. H. Le Brun, A. H. De Boer, H. W. Frijlink, and H. G. M. Heijerman, “A review of the technical aspects of drug nebulization,” *Pharmacy World and Science*, vol. 22, no. 3, pp. 75–81, 2000.
- [92] O. N. M. McCallion, K. M. G. Taylor, P. A. Bridges, M. Thomas, and A. J. Taylor, “Jet nebulisers for pulmonary drug delivery,” *International Journal of Pharmaceutics*, vol. 130, no. 1, pp. 1–11, 1996.
- [93] K. M. G. Taylor and O. N. M. McCallion, “Ultrasonic nebulisers for pulmonary drug delivery,” *International Journal of Pharmaceutics*, vol. 153, no. 1, pp. 93–104, 1997.
- [94] M. Knoch and M. Keller, “The customised electronic nebuliser: a new category of liquid aerosol drug delivery systems,” *Expert Opinion on Drug Delivery*, vol. 2, no. 2, pp. 377–390, 2005.
- [95] S. Gill, R. Löbenberg, T. Ku, S. Azarmi, W. Roa, and E. J. Prenner, “Nanoparticles: characteristics, mechanisms of action, and toxicity in pulmonary drug delivery—a review,” *Journal of Biomedical Nanotechnology*, vol. 3, no. 2, pp. 107–119, 2007.

- [96] J. W. Card, D. C. Zeldin, J. C. Bonner, and E. R. Nestmann, "Pulmonary applications and toxicity of engineered nanoparticles," *American Journal of Physiology*, vol. 295, no. 3, pp. L400–L411, 2008.
- [97] W. H. De Jong and P. J. A. Borm, "Drug delivery and nanoparticles: applications and hazards," *International Journal of Nanomedicine*, vol. 3, no. 2, pp. 133–149, 2008.
- [98] K. R. Vega-Villa, J. K. Takemoto, J. A. Yáñez, C. M. Remsberg, M. L. Forrest, and N. M. Davies, "Clinical toxicities of nanocarrier systems," *Advanced Drug Delivery Reviews*, vol. 60, no. 8, pp. 929–938, 2008.
- [99] M. Caldorera-Moore and N. A. Peppas, "Micro- and nanotechnologies for intelligent and responsive biomaterial-based medical systems," *Advanced Drug Delivery Reviews*, vol. 61, no. 15, pp. 1391–1401, 2009.
- [100] L. A. Dailey and T. Kissel, "New poly(lactic-co-glycolic acid) derivatives: modular polymers with tailored properties," *Drug Discovery Today: Technologies*, vol. 2, no. 1, pp. 7–13, 2005.
- [101] L. A. Dailey, M. Wittmar, and T. Kissel, "The role of branched polyesters and their modifications in the development of modern drug delivery vehicles," *Journal of Controlled Release*, vol. 101, no. 1–3, pp. 137–149, 2005.
- [102] F. Unger, M. Wittmar, F. Morell, and T. Kissel, "Branched polyesters based on poly[vinyl-3-(dialkylamino)alkylcarbamate-co-vinyl acetate-co-vinyl alcohol]-graft-poly(d,l-lactide-co-glycolide): effects of polymer structure on in vitro degradation behaviour," *Biomaterials*, vol. 29, no. 13, pp. 2007–2014, 2008.
- [103] F. Unger, M. Wittmar, and T. Kissel, "Branched polyesters based on poly[vinyl-3-(dialkylamino)alkylcarbamate-co-vinyl acetate-co-vinyl alcohol]-graft-poly(d,l-lactide-co-glycolide): effects of polymer structure on cytotoxicity," *Biomaterials*, vol. 28, no. 9, pp. 1610–1619, 2007.
- [104] L. A. Dailey, N. Jekel, L. Fink et al., "Investigation of the proinflammatory potential of biodegradable nanoparticle drug delivery systems in the lung," *Toxicology and Applied Pharmacology*, vol. 215, no. 1, pp. 100–108, 2006.
- [105] L. A. Dailey, E. Kleemann, M. Wittmar et al., "Surfactant-free, biodegradable nanoparticles for aerosol therapy based on the branched polyesters, DEAPA-PVAL-g-PLGA," *Pharmaceutical Research*, vol. 20, no. 12, pp. 2011–2020, 2003.
- [106] M. Beck-Broichsitter, J. Gauss, C. B. Packhaeuser et al., "Pulmonary drug delivery with aerosolizable nanoparticles in an ex vivo lung model," *International Journal of Pharmaceutics*, vol. 367, no. 1–2, pp. 169–178, 2009.
- [107] J. Fu, J. Fiegel, E. Krauland, and J. Hanes, "New polymeric carriers for controlled drug delivery following inhalation or injection," *Biomaterials*, vol. 23, no. 22, pp. 4425–4433, 2002.
- [108] J. Fu, J. Fiegel, and J. Hanes, "Synthesis and characterization of PEG-based ether-anhydride terpolymers: novel polymers for controlled drug delivery," *Macromolecules*, vol. 37, no. 19, pp. 7174–7180, 2004.
- [109] J. Fiegel, J. Fu, and J. Hanes, "Poly(ether-anhydride) dry powder aerosols for sustained drug delivery in the lungs," *Journal of Controlled Release*, vol. 96, no. 3, pp. 411–423, 2004.
- [110] J. M. Barichello, M. Morishita, K. Takayama, and T. Nagai, "Encapsulation of hydrophilic and lipophilic drugs in PLGA nanoparticles by the nanoprecipitation method," *Drug Development and Industrial Pharmacy*, vol. 25, no. 4, pp. 471–476, 1999.
- [111] T. Govender, S. Stolnik, M. C. Garnett, L. Illum, and S. S. Davis, "PLGA nanoparticles prepared by nanoprecipitation: drug loading and release studies of a water soluble drug," *Journal of Controlled Release*, vol. 57, no. 2, pp. 171–185, 1999.
- [112] M. Wittmar, F. Unger, and T. Kissel, "Biodegradable brush-like branched polyesters containing a charge-modified poly(vinyl alcohol) backbone as a platform for drug delivery systems: synthesis and characterization," *Macromolecules*, vol. 39, no. 4, pp. 1417–1424, 2006.
- [113] X. Wang, X. Xie, C. Cai, E. Rytting, T. Steele, and T. Kissel, "Biodegradable branched polyesters poly(vinyl sulfonate-covinyl alcohol)-graft poly(D,L-lactic-coglycolic acid) as a negatively charged polyelectrolyte platform for drug delivery: synthesis and characterization," *Macromolecules*, vol. 41, no. 8, pp. 2791–2799, 2008.
- [114] J. Heyder, J. Gebhart, G. Rudolf, C. F. Schiller, and W. Stahlhofen, "Deposition of particles in the human respiratory tract in the size range 0.005–15 µm," *Journal of Aerosol Science*, vol. 17, no. 5, pp. 811–825, 1986.
- [115] C. Jaafar-Malej, V. Andrieu, A. Elaissari, and H. Fessi, "Assessment methods of inhaled aerosols: technical aspects and applications," *Expert Opinion on Drug Delivery*, vol. 6, no. 9, pp. 941–959, 2009.
- [116] J. Liu, T. Gong, H. Fu et al., "Solid lipid nanoparticles for pulmonary delivery of insulin," *International Journal of Pharmaceutics*, vol. 356, no. 1–2, pp. 333–344, 2008.
- [117] J. Hureaux, F. Lagarce, F. Gagnadoux et al., "Lipid nanocapsules: ready-to-use nanovectors for the aerosol delivery of paclitaxel," *European Journal of Pharmaceutics and Biopharmaceutics*, vol. 73, no. 2, pp. 239–246, 2009.
- [118] T. Ghazanfari, A. M. A. Elhissi, Z. Ding, and K. M. G. Taylor, "The influence of fluid physicochemical properties on vibrating-mesh nebulization," *International Journal of Pharmaceutics*, vol. 339, no. 1–2, pp. 103–111, 2007.
- [119] A. H. L. Chow, H. H. Y. Tong, P. Chattopadhyay, and B. Y. Shekunov, "Particle engineering for pulmonary drug delivery," *Pharmaceutical Research*, vol. 24, no. 3, pp. 411–437, 2007.
- [120] P. C. Seville, H. Y. Li, and T. P. Learoyd, "Spray-dried powders for pulmonary drug delivery," *Critical Reviews in Therapeutic Drug Carrier Systems*, vol. 24, no. 4, pp. 307–360, 2007.
- [121] D. Lemoine, C. Francois, F. Kedzierewicz, V. Preat, M. Hoffman, and P. Maincent, "Stability study of nanoparticles of poly( $\epsilon$ -caprolactone), poly(D,L-lactide) and poly(D,L-lactide-co-glycolide)," *Biomaterials*, vol. 17, no. 22, pp. 2191–2197, 1996.
- [122] M. S. Muthu and S. Feng, "Pharmaceutical stability aspects of nanomedicines," *Nanomedicine*, vol. 4, no. 8, pp. 857–860, 2009.
- [123] W. Abdelwahed, G. Degobert, S. Stainmesse, and H. Fessi, "Freeze-drying of nanoparticles: formulation, process and storage considerations," *Advanced Drug Delivery Reviews*, vol. 58, no. 15, pp. 1688–1713, 2006.
- [124] P. Tewa-Tagne, S. Briançon, and H. Fessi, "Preparation of redispersible dry nanocapsules by means of spray-drying: development and characterisation," *European Journal of Pharmaceutical Sciences*, vol. 30, no. 2, pp. 124–135, 2007.
- [125] G. Pilcer and K. Amighi, "Formulation strategy and use of excipients in pulmonary drug delivery," *International Journal of Pharmaceutics*, vol. 392, no. 1–2, pp. 1–19, 2010.
- [126] K. Tomoda, T. Ohkoshi, K. Hirota et al., "Preparation and properties of inhalable nanocomposite particles for treatment of lung cancer," *Colloids and Surfaces B*, vol. 71, no. 2, pp. 177–182, 2009.
- [127] J. C. Sung, D. J. Padilla, L. Garcia-Contreras et al., "Formulation and pharmacokinetics of self-assembled rifampicin

- nanoparticle systems for pulmonary delivery," *Pharmaceutical Research*, vol. 26, no. 8, pp. 1847–1855, 2009.
- [128] L. Ely, W. Roa, W. H. Finlay, and R. Löbenberg, "Effervescent dry powder for respiratory drug delivery," *European Journal of Pharmaceutics and Biopharmaceutics*, vol. 65, no. 3, pp. 346–353, 2007.
- [129] L. Shi, C. J. Plumley, and C. Berkland, "Biodegradable nanoparticle flocculates for dry powder aerosol formulation," *Langmuir*, vol. 23, no. 22, pp. 10897–10901, 2007.
- [130] L. J. Peek, L. Roberts, and C. Berkland, "Poly(D,L-lactide-co-glycolide) nanoparticle agglomerates as carriers in dry powder aerosol formulation of proteins," *Langmuir*, vol. 24, no. 17, pp. 9775–9783, 2008.
- [131] N. R. Mathias, F. Yamashita, and V. H. L. Lee, "Respiratory epithelial cell culture models for evaluation of ion and drug transport," *Advanced Drug Delivery Reviews*, vol. 22, no. 1-2, pp. 215–249, 1996.
- [132] A. Steimer, E. Haltner, and C. M. Lehr, "Cell culture models of the respiratory tract relevant to pulmonary drug delivery," *Journal of Aerosol Medicine*, vol. 18, no. 2, pp. 137–182, 2005.
- [133] J. L. Sporty, L. Horálková, and C. Ehrhardt, "In vitro cell culture models for the assessment of pulmonary drug disposition," *Expert Opinion on Drug Metabolism and Toxicology*, vol. 4, no. 4, pp. 333–345, 2008.
- [134] G. L. Amidon, H. Lennernas, V. P. Shah, and J. R. Crison, "A theoretical basis for a biopharmaceutic drug classification: the correlation of in vitro drug product dissolution and in vivo bioavailability," *Pharmaceutical Research*, vol. 12, no. 3, pp. 413–420, 1995.
- [135] H. Eixarch, E. Haltner-Ukomadu, C. Beisswenger, and U. Bock, "Drug delivery to the lung: permeability and physicochemical characteristics of drugs as the basis for a pulmonary biopharmaceutical classification system (pBCS)," *Journal of Epithelial Biology and Pharmacology*, vol. 3, pp. 1–14, 2010.
- [136] S. A. Cryan, N. Sivadas, and L. Garcia-Contreras, "In vivo animal models for drug delivery across the lung mucosal barrier," *Advanced Drug Delivery Reviews*, vol. 59, no. 11, pp. 1133–1151, 2007.
- [137] P. Gerde, "Animal models and their limitations: on the problem of high-to-low dose extrapolations following inhalation exposures," *Experimental and Toxicologic Pathology*, vol. 57, no. 1, supplement, pp. 143–146, 2005.
- [138] R. W. Niemeier, "Isolated perfused rabbit lung: a critical appraisal," *Environmental Health Perspectives*, vol. 16, pp. 67–71, 1976.
- [139] H. M. Mehendale, L. S. Angevine, and Y. Ohmiya, "The isolated perfused lung. A critical evaluation," *Toxicology*, vol. 21, no. 1, pp. 1–36, 1981.
- [140] R. W. Niemeier, "The isolated perfused lung," *Environmental Health Perspectives*, vol. 56, pp. 35–41, 1984.
- [141] W. Seeger, D. Walmarth, F. Grimminger et al., "Adult respiratory distress syndrome: model systems using isolated perfused rabbit lungs," *Methods in Enzymology*, vol. 233, pp. 549–584, 1994.
- [142] P. R. Byron and R. W. Niven, "A novel dosing method for drug administration to the airways of the isolated perfused rat lung," *Journal of Pharmaceutical Sciences*, vol. 77, no. 8, pp. 693–695, 1988.
- [143] P. R. Byron, N. S. R. Roberts, and A. R. Clark, "An isolated perfused rat lung preparation for the study of aerosolized drug deposition and absorption," *Journal of Pharmaceutical Sciences*, vol. 75, no. 2, pp. 168–171, 1986.
- [144] R. W. Niven and P. R. Byron, "Solute absorption from the airways of the isolated rat lung. I. The use of absorption data to quantify drug dissolution or release in the respiratory tract," *Pharmaceutical Research*, vol. 5, no. 9, pp. 574–579, 1988.
- [145] R. W. Niven and P. R. Byron, "Solute absorption from the airways of the isolated rat lung II. Effect of surfactants on absorption of fluorescein," *Pharmaceutical Research*, vol. 7, no. 1, pp. 8–13, 1990.
- [146] R. W. Niven, F. Rypacek, and P. R. Byron, "Solute absorption from the airways of the isolated rat lung. III. Absorption of several peptidase-resistant, synthetic polypeptides: poly-(2-hydroxyethyl)-aspartamides," *Pharmaceutical Research*, vol. 7, no. 10, pp. 990–994, 1990.
- [147] P. R. Byron, Z. Sun, H. Katayama, and F. Rypacek, "Solute absorption from the airways of the isolated rat lung. IV. mechanisms of absorption of fluorophore-labeled poly- $\alpha,\beta$ -[N(2-hydroxyethyl)-DL-aspartamide]," *Pharmaceutical Research*, vol. 11, no. 2, pp. 221–225, 1994.
- [148] J. Z. Sun, P. R. Byron, and F. Rypacek, "Solute absorption from the airways of the isolated rat lung. V. Charge effects on the absorption of copolymers of N(2-hydroxyethyl)-DL-aspartamide with DL-aspartic acid or dimethylaminopropyl-DL-aspartamide," *Pharmaceutical Research*, vol. 16, no. 7, pp. 1104–1108, 1999.
- [149] M. Sakagami, P. R. Byron, J. Venitz, and F. Rypacek, "Solute disposition in the rat lung in vivo and in vitro: determining regional absorption kinetics in the presence of mucociliary escalator," *Journal of Pharmaceutical Sciences*, vol. 91, no. 2, pp. 594–604, 2002.
- [150] M. Sakagami, P. R. Byron, and F. Rypacek, "Biochemical evidence for transcytotic absorption of polyspartamide from the rat lung: effects of temperature and metabolic inhibitors," *Journal of Pharmaceutical Sciences*, vol. 91, no. 9, pp. 1958–1968, 2002.
- [151] Y. Pang, M. Sakagami, and P. R. Byron, "The pharmacokinetics of pulmonary insulin in the in vitro isolated perfused rat lung: implications of metabolism and regional deposition," *European Journal of Pharmaceutical Sciences*, vol. 25, no. 4-5, pp. 369–378, 2005.
- [152] Y. Pang, M. Sakagami, and P. R. Byron, "Insulin self-association: effects on lung disposition kinetics in the airways of the isolated perfused rat lung (IPRL)," *Pharmaceutical Research*, vol. 24, no. 9, pp. 1636–1644, 2007.
- [153] A. Ryrfeldt, G. Persson, and E. Nilsson, "Pulmonary disposition of the potent glucocorticoid budesonide, evaluated in an isolated perfused rat lung model," *Biochemical Pharmacology*, vol. 38, no. 1, pp. 17–22, 1989.
- [154] M. J. Jesús Valle, F. González López, and A. Sánchez Navarro, "Pulmonary versus systemic delivery of levofloxacin. The isolated lung of the rat as experimental approach for assessing pulmonary inhalation," *Pulmonary Pharmacology and Therapeutics*, vol. 21, no. 2, pp. 298–303, 2008.
- [155] P. Ewing, S. J. Eirefelt, P. Andersson, A. Blomgren, A. Ryrfeldt, and P. Gerde, "Short inhalation exposures of the isolated and perfused rat lung to respirable dry particle aerosols; the detailed pharmacokinetics of budesonide, formoterol, and terbutaline," *Journal of Aerosol Medicine*, vol. 21, no. 2, pp. 169–180, 2008.
- [156] A. Tronde, BO. Nordén, A. B. Jeppsson et al., "Drug absorption from the isolated perfused rat lung—correlations with drug physicochemical properties and epithelial permeability," *Journal of Drug Targeting*, vol. 11, no. 1, pp. 61–74, 2003.
- [157] A. Tronde, E. Krondahl, H. Von Euler-Chelpin et al., "High airway-to-blood transport of an opioid tetrapeptide in the

- isolated rat lung after aerosol delivery," *Peptides*, vol. 23, no. 3, pp. 469–478, 2002.
- [158] F. Kroll, J. A. Karlsson, E. Nilsson, A. Ryrfeldt, and C. G. A. Persson, "Rapid clearance of xanthines from airway and pulmonary tissues," *American Review of Respiratory Disease*, vol. 141, no. 5, pp. 1167–1171, 1990.
- [159] K. Lahnstein, T. Schmehl, U. Rüscher, M. Rieger, W. Seeger, and T. Gessler, "Pulmonary absorption of aerosolized fluorescent markers in the isolated rabbit lung," *International Journal of Pharmaceutics*, vol. 351, no. 1-2, pp. 158–164, 2008.
- [160] R. T. Schermuly, A. Schulz, H. A. Ghofrani et al., "Comparison of pharmacokinetics and vasodilatory effect of nebulized and infused iloprost in experimental pulmonary hypertension: rapid tolerance development," *Journal of Aerosol Medicine*, vol. 19, no. 3, pp. 353–363, 2006.
- [161] M. Beck-Broichsitter, J. Gauss, T. Gessler, W. Seeger, T. Kissel, and T. Schmehl, "Pulmonary targeting with biodegradable salbutamol-loaded nanoparticles," *Journal of Aerosol Medicine*, vol. 23, no. 1, pp. 47–57, 2010.
- [162] R. K. Brazzell, R. B. Smith, and H. B. Kostenbader, "Isolated perfused rabbit lung as a model for intravascular and intrabronchial administration of bronchodilator drugs I: isoproterenol," *Journal of Pharmaceutical Sciences*, vol. 71, no. 11, pp. 1268–1274, 1982.
- [163] R. K. Brazzell and H. B. Kostenbader, "Isolated perfused rabbit lung as a model for intravascular and intrabronchial administration of bronchodilator drugs II: isoproterenol prodrugs," *Journal of Pharmaceutical Sciences*, vol. 71, no. 11, pp. 1274–1281, 1982.
- [164] O. G. Raabe, H. S. Yeh, G. J. Newton, R. F. Phalen, and D. J. Velasquez, "Deposition of inhaled monodispers aerosols in small rodents," in *Inhaled Particles IV*, W. H. Walton, Ed., pp. 3–21, Pergamon Press, Oxford, UK, 1977.
- [165] A. Tronde, G. Baran, S. Eirefelt, H. Lennernäs, and U. H. Bengtsson, "Miniaturized nebulization catheters: a new approach for delivery of defined aerosol doses to the rat lung," *Journal of Aerosol Medicine*, vol. 15, no. 3, pp. 283–296, 2002.
- [166] C. Hofstetter, M. Flonder, E. Thein et al., "Aerosol delivery during mechanical ventilation to the rat," *Experimental Lung Research*, vol. 30, no. 7, pp. 635–651, 2004.
- [167] R. J. MacLoughlin, B. D. Higgins, J. G. Laffey, and T. O'Brien, "Optimized aerosol delivery to a mechanically ventilated rodent," *Journal of Aerosol Medicine*, vol. 22, no. 4, pp. 323–332, 2009.
- [168] R. W. Niemeier and E. Bingham, "An isolated perfused lung preparation for metabolic studies," *Life Sciences*, vol. 11, no. 16, pp. 807–820, 1972.
- [169] F. Kroll, J.-A. Karlsson, and E. Nilsson, "Lung mechanics of the guinea-pig isolated perfused lung," *Acta Physiologica Scandinavica*, vol. 128, no. 1, pp. 1–8, 1986.
- [170] S. Uhlig and O. Heiny, "Measuring the weight of the isolated perfused rat lung during negative pressure ventilation," *Journal of Pharmacological and Toxicological Methods*, vol. 33, no. 3, pp. 147–152, 1995.
- [171] S. Uhlig and L. Wollin, "An improved setup for the isolated perfused rat lung," *Journal of Pharmacological and Toxicological Methods*, vol. 31, no. 2, pp. 85–94, 1994.
- [172] X. Liu, J. Y. Wang, A. M. Khlebtzos et al., "Influence of perfusate composition on drug disposition in the in-situ perfused rat lung," *International Journal of Pharmaceutics*, vol. 382, no. 1-2, pp. 192–197, 2009.
- [173] J. Hamoir, A. Nemmar, D. Halloy et al., "Effect of polystyrene particles on lung microvascular permeability in isolated perfused rabbit lungs: role of size and surface properties," *Toxicology and Applied Pharmacology*, vol. 190, no. 3, pp. 278–285, 2003.
- [174] A. Nemmar, J. Hamoir, B. Nemery, and P. Gustin, "Evaluation of particle translocation across the alveolo-capillary barrier in isolated perfused rabbit lung model," *Toxicology*, vol. 208, no. 1, pp. 105–113, 2005.
- [175] A. Tronde, B. O. Nordén, H. Marchner, A. K. Wendel, H. Lennernäs, and U. H. Bengtsson, "Pulmonary absorption rate and bioavailability of drugs in vivo in rats: structure-absorption relationships and physicochemical profiling of inhaled drugs," *Journal of Pharmaceutical Sciences*, vol. 92, no. 6, pp. 1216–1233, 2003.
- [176] F. Manford, A. Tronde, A. B. Jeppsson, N. Patel, F. Johansson, and B. Forbes, "Drug permeability in 16HBE14o- airway cell layers correlates with absorption from the isolated perfused rat lung," *European Journal of Pharmaceutical Sciences*, vol. 26, no. 5, pp. 414–420, 2005.
- [177] E. Ryting, M. Bur, R. Cartier et al., "In vitro and in vivo performance of biocompatible negatively-charged salbutamol-loaded nanoparticles," *Journal of Controlled Release*, vol. 141, no. 1, pp. 101–107, 2010.